2-8-2011

Structural and Magnetic Phase Transitions in Manganese Arsenide Thin-Films Grown by Molecular Beam Epitaxy

Felix T. Jaeckel

Follow this and additional works at: https://digitalrepository.unm.edu/phyc_etds

Recommended Citation
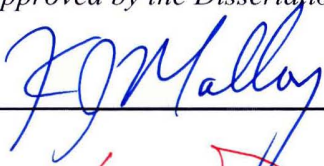
Felix Till Jaeckel

Candidate

Physics and Astronomy

Department

This dissertation is approved, and it is acceptable in quality
and form for publication:
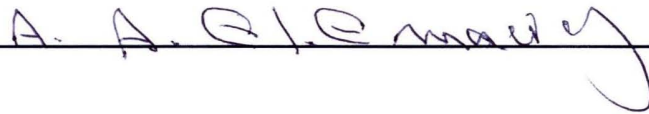
Approved by the Dissertation Committee:

_____ , Chairperson

_____

_____

_____

_____

_____

_____

Structural and Magnetic Phase Transitions in Manganese Arsenide Thin-Films Grown by Molecular Beam Epitaxy

by

Felix Till Jaeckel

Vordiplom, Julius-Maximilians-Universität Würzburg, 2000

M.S., Physics, University of New Mexico, 2002

DISSERTATION

Submitted in Partial Fulfillment of the

Requirements for the Degree of

Doctor of Philosophy

Physics

The University of New Mexico

Albuquerque, New Mexico

December, 2010

Dedication

To my wife and children, for their love, patience, and support.

"Every calculation based on experience elsewhere
fails in New Mexico."

Lew Wallace (1827-1905), Governor of Territorial New Mexico, 1878-1881,

Author of Ben Hur.

Acknowledgments

The following people deserve thanks:

- Prof. Kevin Malloy, my advisor, for his continued support, guidance, and encouragement. And for giving me the opportunity to pursue my varied interests.

- Prof. Steve Boyd as a committee member for critical reading of the manuscript and many fruitful discussions.

- Prof. Rob Duncan for serving on my committee and hosting me at Caltech to use the SQUID susceptometer.

- Prof. Abdel-Rahman El-Emawy, for setting up the MBE machine and exploring the growth of both GaMnAs and MnAs.

- Dr. Andreas Stintz, for teaching me a lot about MBE growth and for many illuminating discussions over the years.

- Prof. Tom Sigmon for initiating the spintronics project at CHTM.

- Dr. Alexander Albrecht, for sharing his expertise, especially regarding mechanical apparatus and photography, and for machining sample holders and other parts. His great diligence in proofreading this dissertation is also highly appreciated.

- Dr. Chi Yang, for allowing me to (ab-)use his temperature-controlled laser testing stage for X-ray diffraction experiments.

- Ron Kay, for his help with many custom electronics projects and supplying humor.

- Mike Lebiednik, for installing the magnet reversal system and spending some time hanging from the ceiling.

Structural and Magnetic Phase Transitions in Manganese Arsenide Thin-Films Grown by Molecular Beam Epitaxy

by

Felix Till Jaeckel

ABSTRACT OF DISSERTATION

Submitted in Partial Fulfillment of the
Requirements for the Degree of

Doctor of Philosophy
Physics

The University of New Mexico

Albuquerque, New Mexico

December, 2010

Structural and Magnetic Phase Transitions in Manganese Arsenide Thin-Films Grown by Molecular Beam Epitaxy

by

Felix Till Jaeckel

Vordiplom, Julius-Maximilians-Universität Würzburg, 2000

M.S., Physics, University of New Mexico, 2002

PhD., Physics, University of New Mexico, 2010

Abstract

Phase transitions play an important role in many fields of physics and engineering, and their study in bulk materials has a long tradition. Many of the experimental techniques involve measurements of thermodynamically extensive parameters. With the increasing technological importance of thin-film technology there is a pressing need to find new ways to study phase transitions at smaller length-scales, where the traditional methods are insufficient.

In this regard, the phase transitions observed in thin-films of MnAs present interesting challenges. As a ferromagnetic material that can be grown epitaxially on a

variety of technologically important substrates, MnAs is an interesting material for spintronics applications. In the bulk, the first order transition from the low temperature ferromagnetic α-phase to the β-phase occurs at 313 K. The magnetic state of the β-phase has remained controversial. A second order transition to the paramagnetic γ-phase takes place at 398 K. In thin-films, the anisotropic strain imposed by the substrate leads to the interesting phenomenon of coexistence of α- and β-phases in a regular array of stripes over an extended temperature range.

In this dissertation these phase transitions are studied in films grown by molecular beam epitaxy on GaAs (001). The films are confirmed to be of high structural quality and almost purely in the A_0 orientation.

A diverse set of experimental techniques, germane to thin-film technology, is used to probe the properties of the film: Temperature-dependent X-ray diffraction and atomic-force microscopy (AFM), as well as magnetotransport give insights into the structural properties, while the anomalous Hall effect is used as a probe of magnetization during the phase transition. In addition, reflectance difference spectroscopy (RDS) is used as a sensitive probe of electronic structure.

Inductively coupled plasma etching with BCl_3 is demonstrated to be effective for patterning MnAs. We show that the evolution of electrical resistivity in the coexistence regime of α- and β-phase can be understood in terms of a simple model. These measurements allow accurate extraction of the order-parameter "phase fraction" and thus permit us to study the hysteresis of the phase transition in detail. Major features in the hysteresis can be correlated to the ordering observed in the array of α- and β-stripes.

As the continuous ferromagnetic film breaks up into isolated stripes of α-phase, a hysteresis in the out-of-plane magnetization is detected from measurements of the anomalous Hall effect. The appearance of out-of-plane domains can be understood

from simple shape-anisotropy arguments. Remarkably, an anomaly of the Hall effect at low fields persists far into the β-phase.

Signatures of the more elusive β- to γ-transition are found in the temperature-dependence of resistivity, the out-of-plane lattice constant, and reflectance difference spectra. The transition temperature is significantly lowered compared to the bulk, consistent with the strained state of the material. The negative temperature coefficient of resistivity, as well as its anisotropic changes, lend support to the idea of an antiferromagnetic order within the β-phase.

Contents

Contents

Contents

Contents

List of Figures

List of Tables

List of Tables

Glossary

Abbreviations

AF   Antiferromagnetic

AFM   Atomic Force Microscopy

AHE   Anomalous Hall Effect

BEP   Beam-Equivalent Pressure

cps   Counts Per Second

CMCE   Colossal Magnetocaloric Effect

CMRR   Common-Mode Rejection Ratio

DFT   Density Functional Theory

DI   Deionized (water)

DOS   Density of States

EHL   Envelope Hysteresis Loop

F   Ferromagnetic

Glossary

FET	Field Effect Transistor
FWHM	Full-Width at Half-Maximum
GMCE	Giant Magnetocaloric Effect
GNU	GNU's Not Unix!
HOPG	Highly Oriented Pyrolytic Graphite
HT	High Temperature (growth)
ICP	Inductively Coupled Plasma (etcher)
LT	Low Temperature (growth)
MBE	Molecular Beam Epitaxy
MCE	Magnetocaloric Effect
MHL	Minor Hysteresis Loop
MFM	Magnetic Force Microscopy
MR	Magnetoresistance
PEM	Photoelastic Modulator
PI	Proportional/Integral (controller)
PM	Paramagnetic
PMMA	Poly(Methyl Methacrylate)
PVC	Polyvinyl Chloride
RAS	Reflectance Anisotropy Spectroscopy

Roman Symbols

Glossary

A_0, A_1, B_0, B_1	Epitaxial orientations of MnAs (see Fig. 2.5)
b	Sample height misalignment
B	Bulk modulus (Chapter 2)
$\vec{B}$	Magnetic induction in Tesla
B_{ex}	Exchange field
$B_J(x)$	Brillouin function
c_{ij}	Stiffness tensor
C	Curie constant
$d_{(hkjl)}$	Lattice plane spacing of lattice plane $(hkjl)$
E	Energy
$\vec{E}$	Electric field
$f_{[hkl]}$	Lattice mismatch along crystallographic direction $[hkl]$
f_α, f_β	α- and β-phase fractions
$f_i^\uparrow$, $f_i^\downarrow$	Phase fraction of phase i for heating, cooling
$\overline{f_i}$	Average phase fraction
Δf_i	Hysteresis in phase fraction
f_0	Atomic scattering factor.
F_{hkl}	X-ray structure factor.
g	Landé-factor

Glossary

$G(\omega)$	Gaussian function
h	Height
(hkl)	Miller indices of crystallographic plane
$(hkjl)$	Miller-Bravais indices for hexagonal lattice $(h + k + j = 0)$
H_c	Critical field
H_c	Saturation field
$\vec{H}$	Magnetic field in A/m
I	Current
$\vec{I}$	Magnetic polarization in Tesla
$I(\omega)$	Arbitrary X-ray line profile
$\vec{j}$	Current density
J	Total angular momentum quantum number
$J_1(x),\ J_2(x)$	Bessel function of the first kind, first and second order
$\vec{k}$	Wave-vector
$K_1,\ K_2,\ K_3$	Constants of magnetocrystalline anisotropy
l	Length
L	Orbital angular momentum quantum number
$L(\omega)$	Lorentzian function
m_S	Spin quantum number

Glossary

M^s	Saturation magnetization
M_s	Spontaneous magnetization
$\vec{M}$	Magnetization in A/m
n	Carrier density
N_i	Demagnetizing factor
p	Aspect ration h/w
q	Charge
q_x, q_y	Spatial frequency coordinates
Q_x, Q_z	In-plane and out-of-plane components of X-ray scattering vector
r	(Reflectivity) Coefficient of reflection, defined as the ratio between reflected and incident field amplitude
R	(Reflectance) Coefficient of reflection, defined as the ratio between reflected and incident intensities
R	Diffractometer radius
R_0	Ordinary Hall constant
R_S	Spontaneous Hall constant
S	Spin angular momentum quantum number
$\vec{S}$	X-ray scattering vector
s_{ij}	Compliance tensor
t	Thickness (of epilayer)

Glossary

T	Temperature
T_C	Curie temperature
T_N	Néel temperature
$\vec{v}$	Velocity
V	Volume (of the unit cell)
V_{xx}	Longitudinal voltage on Hall-bar
V_{xy}	Hall voltage
$V(\omega)$	Voigt function
w	Width
x	Atomic composition, as in $Ga_{(1-x)}Mn_xAs$
x, y, z	Cartesian coordinates

Greek Symbols

α_V	Volumetric thermal expansion coefficient
γ	Exponent in anomalous Hall effect
γ_L, γ_G	FWHM of Lorentzian/Gaussian
ε_{ij}	Strain tensor
ϵ_{ij}	Dielectric tensor
$\Theta, 2\Theta$	Bragg angle and scattering angle
κ	Compressibility

Glossary

λ	Wavelength of light or X-rays
Λ	Periodicity of stripes
$\vec{\mu}$	Magnetic moment
μ	Center position of peak
μ_0	Vacuum permittivity
μ_{eff}	Effective magnetic moment
μ_B	Bohr magneton
ν	Poisson ratio
ρ	Density
ρ_{xx}^{sheet}	Sheet resistivity
ρ_{ij}	Resistivity tensor
ρ_{xy}^{s}	Saturation Hall resistance
σ_{ij}	Stress tensor (Chapters 2 and 5); Conductivity tensor (Chapter 4)
Φ	Angle of rotation around surface normal
χ	Magnetic susceptibility
χ_{hf}	High-field susceptibility
Ψ	Angle between surface normal and X-ray scattering plane
ω	Angle of first goniometer axis
$\delta\omega$	Difference in X-ray peak positions

Chapter 1

Introduction

Due to their ubiquity in nature, the study of phase transitions is of great practical importance and has a long tradition in physics. From a theoretical basis, phase transitions are described in terms of the free energy. Therefore, from an experimental viewpoint, the study of phase transitions involves measurements of thermodynamically "extensive" quantities, such as enthalpy, volume, and magnetization. These measurements are routinely performed on bulk samples with great sensitivity, thanks to the availability of modern instrumentation such as calorimeters and SQUID magnetometers.

With the growing importance of thin-films and nanomaterials in the last decade, the study of their phase transitions has also gained popularity. For example, phase change materials play important roles as recording media. Magnetic phase transitions of thin-films are at the heart of the emergent field of spintronics.

An interesting material in this regard is MnAs, which can be grown epitaxially on a variety of substrates and exhibits two phase transitions. The transition from the ferromagnetic α- to β-MnAs (above 313 K in the bulk), is a first order coupled magneto-structural transition. A second transition from the β- to the paramagnetic

γ-phase occurs at 398 K. The magnetic state of the β-phase remains controversial to this day. In research publications spanning six decades, β-MnAs has been variously characterized as "antiferromagnetic", "paramagnetic", or exhibiting some other, unspecified "residual magnetic order".

The strain due to the thermal expansion mismatch and the first order phase transition has a profound influence on the α- to β-transition itself. In contrast to the abrupt transition observed in the bulk, the two phases actually coexist over an extended temperature interval in thin-films.

In the last few years, this material system has been studied intensively. Substantial insight into the coupling of magnetic and structural phase transition has thus been gained.

Unfortunately, in thin-films, the presence of the substrate often dominates the measurement of extensive quantities and can thus severely hamper the applicability of bulk techniques to determine extensive thermodynamic quantities. If one wants to measure the heat capacity for a nanomaterial, one may have to remove most of the substrate to obtain a "microcalorimeter". Similarly, in studying the susceptibility of a paramagnetic thin-film, one may need to either remove the substrate or numerically correct for its diamagnetic contribution. In the case of MnAs, the removal of the substrate is not an option, since one desires to investigate precisely the influence of the substrate on the phase transition of the thin-film.

In this dissertation we seek to extend some of the classical thin-film ("local") techniques to the study of phase transitions in thin-films.

- X-ray diffraction

  The lattice parameters of thin-films are thermodynamically intensive quantities. Strictly speaking, however, X-ray diffraction is an "extensive" measurement, as the scattering amplitude depends on the number of scatterers. Be-

cause of its relatively short absorption length, it can nonetheless be regarded as a "local" — and thus non-extensive — probe in certain circumstances.

- Magnetotransport and anomalous Hall effect
  Conductivity and resistivity in and of itself are intensive quantities. Again, since any practical measurement involves a volume integral over current density, the measurement itself has to be considered "global". Luckily, in many cases the substrate is insulating enough that the measurement effectively becomes "local". The anomalous Hall effect, in particular, offers a sensitive probe of magnetization, that is unaffected by the diamagnetic contribution from the GaAs substrate.

- Reflectance difference spectroscopy
  The optical penetration depth scales with the wavelength of light. For metals, penetration depths are on the order of 10s of nanometers in the visible optical regime. Furthermore, light can be focused to a spot size on the order of the wavelength. Therefore, optical techniques are an important "local" characterization tool, with a firmly established place in thin-film characterization. Reflectance difference spectroscopy can resolve very small anisotropies in the dielectric constants, which can be useful for anisotropic materials such as MnAs.

- Atomic force microscopy
  By its nature, scanning probe microscopies are "local" techniques, that allow insights into a variety of variables. In particular, atomic force microscopy can sense the local displacement of ensembles of atoms on an otherwise flat surface.

We will find that the combination of these "local" techniques allows us to gain considerably more insight into the phase transitions than each technique would by itself. In this way we can obtain further insights into the following issues:

- What causes the hysteresis in the α-/β-phase-coexistence?

- What is the influence of strain on the β- to γ-transition?

- What is the magnetic state of the β-phase?

1.1 MnAs as a Spintronics Material

Many of today's data storage technologies are based on thin-films of magnetic materials. With the technological challenges posed by the approaching breakdown of Moore's law, alternative approaches to computing are sought. One such new paradigm is the idea of quantum computing, where information is not just encoded in a binary state. While there are many interesting approaches to the physical implementation of quantum computing, one possible approach for *solid-state* quantum computation may lie in a field that has been termed "spintronics". As in classical electronics, the carrier of information is the electron, but in addition to its charge property, information can also be encoded in its spin. This immediately raises the question by what means one can generate, manipulate, and read-out the spin-state and interface it to the macroscopic world. The coupling of circularly polarized light to the electron spin offers a route to control and read-out electron spin in a solid. To realize this approach, it is desirable to use a material with demonstrated photonic capabilities as the host material, such as GaAs or InP.

1.1.1 Spin Injection

If one wants to control the spin by electric means, a polarized "spin-current" can be injected into a semiconductor from a ferromagnetic material. An electric current can be used to generate a magnetic field to control the magnetization of the magnetic

material. However, the transport of spins across the interface between the magnetic material and the semiconductor is complex. In general, one has to rely on tunnel injection of carriers to bypass the "conductivity-mismatch problem" [1, 2] encountered in diffusive transport. For this purpose, it is important that interfaces of excellent quality can be achieved.

A widely studied candidate for spin-injection is the dilute ferromagnetic alloy $Ga_{1-x}Mn_xAs$, which can be epitaxially grown directly onto GaAs with excellent interface quality [3]. Unfortunately, complex materials issues limit its Curie temperature to about 173 K [4], even after more than a decade of improvement. Epitaxy of conventional magnetic materials like iron, cobalt, or nickel on semiconductors is difficult because of the difference in lattice constants and/or crystal structure. In addition, formation of non-magnetic alloys at the interface can impede efficient tunnel injection. Nonetheless, for carefully selected growth conditions [5] successful tunnel injection using iron on GaAs has been demonstrated, albeit with fairly low injection efficiencies (2% for Fe/GaAs(001) [6] and 13% for Fe/AlGaAs(001) [7]). Despite its dissimilar crystal structure, MnAs can be epitaxially grown on a variety of semiconductor substrates. This, and its sufficiently high Curie temperature, make it an interesting option for further studies of spin injection [8]. It has also been proposed that a zincblende modification of MnAs might be half-metallic [9, 10], i.e. 100% spin polarized at the Fermi level. If such a material could be successfully grown, spin injection efficiencies might be greatly enhanced.

1.1.2 MnAs Clusters in GaMnAs

In $Ga_{1-x}Mn_xAs$, the "workhorse" of the spintronics world, it was found that the formation of interstitial Mn (Mn_I) greatly reduces the Curie temperature T_C of the as-grown material. Low temperature (250°C) post-growth annealing is effective in

the removal of these interstitials and can raise T_C from typically below 80 K to around 170 K [4]. If the material is grown or annealed at higher temperatures, phase segregation occurs and clusters of MnAs form within the matrix. The clusters lead to interesting properties, among them strong magneto-optic effects [11] that may be exploited for devices integrated on GaAs substrates [12], as well as a very large magnetoresistance effect [13].

1.2   MnAs as a Magnetocaloric Refrigerant

A second potential application area for MnAs is magnetic refrigeration [14]. Of the many compounds under investigation, MnAs shows the highest magnetocaloric entropy change of about 30 J kg^{-1}K^{-1} [15] for a field change of 5 T near room temperature. The discovery of an increasing magnetocaloric effect (MCE) with pressure (up to 267 J kg^{-1}K^{-1}) [16] has generated significant attention. This "colossal" magnetocaloric effect (CMCE) is far beyond what has been achieved by other materials exhibiting only a "giant" magnetocaloric effect (GMCE), such as $Gd_5Si_2Ge_2$. A CMCE was claimed for $Mn_{1-x}Fe_xAs$ by de Campos et al. [17], but was disputed by Balli et al. [18], who pointed out the improper application of Maxwell relations to determine the entropy change. Nevertheless, the tunability of ordering temperature and hysteresis through substitutions of Fe [17], Cr [19], Co [20], and Sb [15, 21] may enable the construction of multi-stage magnetic refrigerators. While the high toxicity of the arsenic contained in MnAs may be a show-stopper for some applications, it is certainly not a problem for the cooling of semiconductor-devices based on GaAs.

1.3 Overview

The rest of the dissertation is organized as follows: In Chapter 2, we review the properties of bulk MnAs and discuss in detail the effect of substrate strain on the phase coexistence in thin-films of MnAs. A brief overview of magnetism and anomalous Hall effect concludes the chapter. Chapter 3 details the experimental procedure for the growth of MnAs thin-films on GaAs by molecular beam epitaxy and the structural characterization of the samples. In Chapter 4, we discuss magnetotransport with an emphasis on the correlation with the structural and magnetic α- to β-phase transition. Finally, in Chapter 5 the influence of strain on the β- to γ-transition is investigated by electrical, optical, and structural methods. A summary of the important results is given in Chapter 6.

Chapter 2

Background

In this chapter, we present some background information on the phase transitions and magnetic orderings of bulk MnAs. Then, we turn our attention to thin-films of MnAs, for which the epitaxial constraints considerably alter the α- to β-transition. Finally, some background material on magnetism and the anomalous Hall effect is provided to aid in the understanding of later chapters.

2.1   Bulk MnAs

The phase transitions in bulk MnAs have been the subject of a considerable number of studies since the late 1940s, when Serres [22] discovered the anomalous behavior of susceptibility in the β-phase, and Guillaud [23] identified the phase transition around 313 K as a ferromagnetic to antiferromagnetic transition. One model for this type of transition (F-AF) was developed by Kittel [24], on the premise that the exchange coupling between two magnetic sublattices would vary as a function of one crystallographic parameter and change sign at the transition temperature. On the other hand, Bean and Rodbell [25] concluded that evidence for an antiferromagnetic

ordering in the β-phase was insufficient and attempted to explain the first order nature of the ferromagnetic-paramagnetic (F-PM) transition on the basis of a volume dependent exchange interaction. The debate on the magnetic state of β-MnAs has not been settled to this date.

In the following, we review some of the experimental evidence for the different phases. An overview of the physical properties of the three phases of MnAs is given in Table 2.1. Figure 2.1 shows the phase diagram of the As-Mn system. Besides MnAs, various other phases have been identified. Among these, Mn_2As is antiferromagnetic ($T_N =$573 K [26, 27]). The magnetic state of Mn_3As (space group 63, Cmcm, $a = 3.788$Å, $b = 16.29$Å, $c = 3.788$Å [28]) is unknown. Mn_3As_2 is ferromagnetic with a Curie temperature of about 273 K [29].
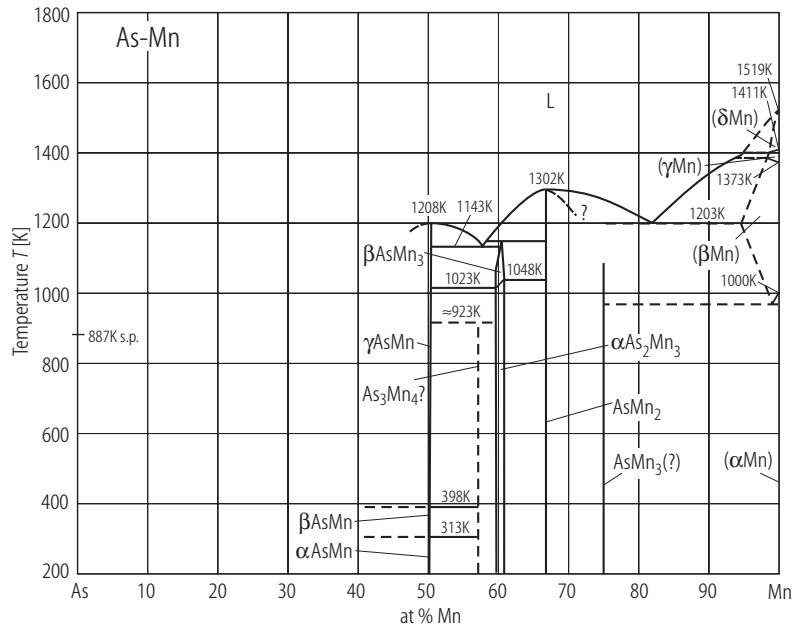
Figure 2.1: Binary phase diagram of the As-Mn system, taken from Landolt-Börnstein [30]. Reprinted with kind permission of Springer Science and Business Media.

		α-phase	β-phase	γ-phase		
Space group		P6$_3$/mmc	Pnma	P6$_3$/mmc		
Lattice constants	a_h	3.717	3.673	3.70	Å	
	b_{oh}	a_h	3.684	a_h	Å	
	c_h	5.722	5.722	5.77	Å	[31]
Density	ρ	6.30	6.43	6.30	g/cm^3	
Volumetric thermal expansion	α_V		$18 \cdot 10^{-5}$	$6.9 \cdot 10^{-5}$	K^{-1}	[32]
Compressibility	κ		$4.5 \cdot 10^{-2}$	$1.7 \cdot 10^{-2}$	GPa^{-1}	[32]
Poisson ratio	ν		0.27	0.40		[32]

Table 2.1: Properties of bulk MnAs in the different phases.

2.1.1 α- to β-Transition

The magneto-structural transition from the α- to the β-phase has been studied extensively. The transition is of first order, accompanied by a latent heat of 7.49 J/g [25], and a discontinuous change in lattice parameters with a thermal hysteresis of about 10 K. The change in volume at the transition is about 2.1%. In 1964, Wilson discovered that the crystal structure changes from hexagonal space group P6$_3$/mmc ("NiAs type") to the orthorhombic space group Pnma [33] ("MnP type").

The nomenclature of the crystallographic setting used throughout this dissertation is illustrated in Fig. 2.2.

For the two crystallographic systems, the following relations hold:

$$a_o = a_h = b_h \tag{2.1}$$

$$b_o \approx \sqrt{3}b_h \tag{2.2}$$

$$c_o = c_h, \tag{2.3}$$

where subscript o denotes the orthorhombic, and h denotes the hexagonal sys-
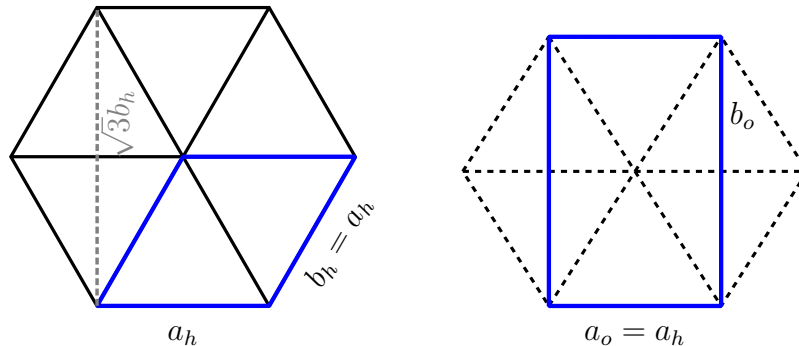
Figure 2.2: Crystallographic setting of MnAs in hexagonal space group P6$_3$/mmc (left) and orthorhombic space group Pnma (right), along with the hexagonal lattice constants (a_h, b_h, c_h), as well as the orthorhombic lattice constants (a_o, b_o, c_o).

tem. Since the orthorhombic distortion from the hexagonal symmetry is small, we introduce a "orthohexagonal" lattice constant b_{oh}, defined as:

$$b_{oh} \equiv \frac{b_o}{\sqrt{3}}. \tag{2.4}$$

With this definition, for vanishing orthorhombic distortion $b_{oh} \to a_o$.

The bulk lattice constants of MnAs have been measured by Willis and Rooksby in 1954 [34], and more recently by Suzuki and Ido in 1982 [31]. A comparison of the two datasets is shown in Fig. 2.3. In the literature, there seems to be no consensus on which dataset is authoritative. The earlier data are reproduced for example in the recent review by Däweritz [35], while the later dataset has been used for density-functional theory (DFT) calculations [36]. While there is good overall agreement of the two datasets, significant discrepancies exist especially in the temperature range of the β-phase. This is likely caused by the incorrect assumption of hexagonal symmetry in the data analysis of the earlier measurement. For that reason, and assuming improved experimental procedure, we will use the Suzuki and Ido dataset.

The lattice constant changes abruptly by about 1% in the temperature range from 305 to 318 K, with a thermal hysteresis of about 10 K.
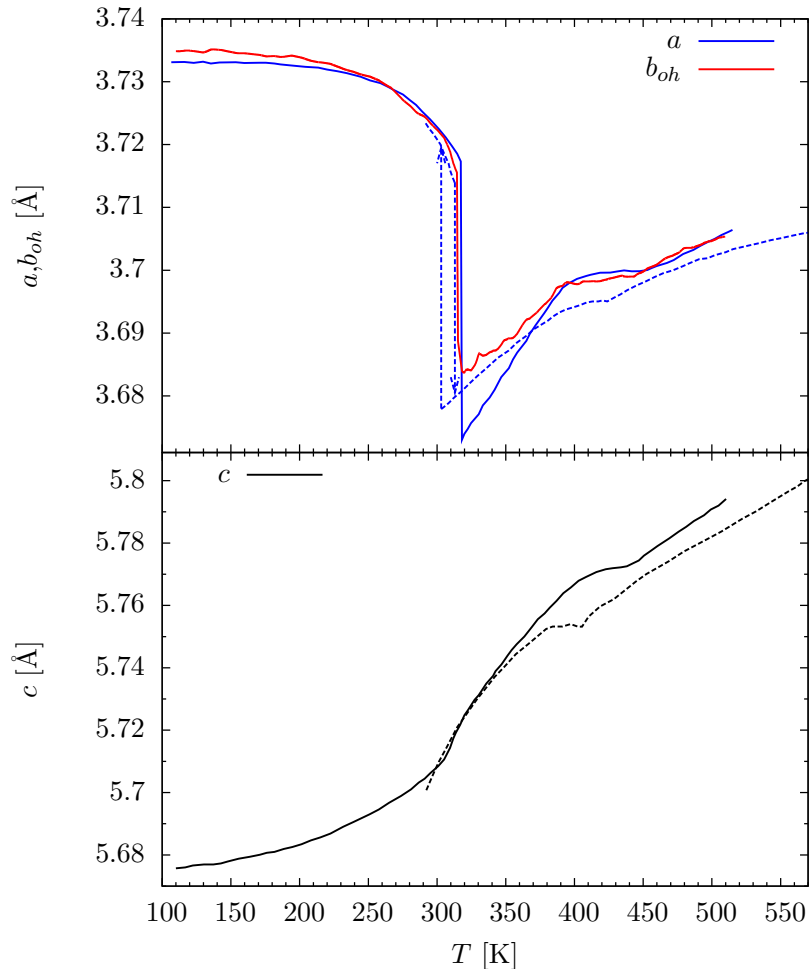
Figure 2.3: Bulk lattice constants of MnAs, as measured by Willis and Rooksby in 1954 [34] (dashed lines) and by Suzuki and Ido in 1982 [31] (solid lines). The Suzuki paper gives only the lattice parameters a, c, as well as the cell volume V, therefore b_{oh} is computed as $\frac{V}{a \cdot c \cdot \sqrt{3}}$.

Concomitantly, the crystal symmetry changes from hexagonal for the α- to orthorhombic for the β-phase, where the b_{oh} lattice constant differs slightly from the a lattice constant.

The α- to β-transition is a coupled "magneto-structural" phase transition, as demonstrated by the shift of the transition to higher temperatures under applied

magnetic fields with a slope of about 3.5 K/T [37] to 4 K/T [38].

The loss of magnetization is discontinuous, as shown in Fig. 2.4. If one extrapolates the spontaneous magnetization to higher temperature, one finds a "true" Curie temperature for α-MnAs of about 400 K [39].
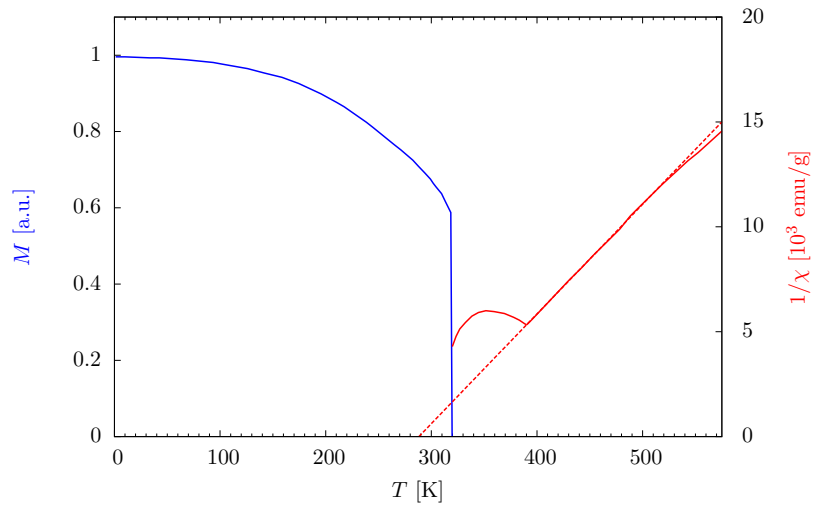
Figure 2.4: Bulk magnetization (blue) and inverse susceptibility (red) of MnAs, after Ido [40]. The dashed red line is a Curie fit to the γ-phase susceptibility, resulting in an extrapolated $T_c = 288$ K.

Remarkably, the susceptibility in the β-phase does not follow the typical Curie-Weiss behavior [22, 23].

The γ-phase, on the other hand, shows a paramagnetic susceptibility with an effective moment μ_{eff} of 4.45 μ_B and an extrapolated Curie temperature of 285 K [22].

2.1.2 β- to γ-Transition

With increasing temperature, the orthorhombic distortion of the β-phase decreases. At about 398 K, hexagonal symmetry ($b_{oh} = a$) is restored, marking the phase transition from the β- to the γ-phase. The γ-phase is is undoubtedly paramagnetic,

as its susceptibility follows the Curie-Weiss law.

2.1.3 Magnetic State of the β-Phase

After magnetic measurements by Serres and Guillaud showed that susceptibility in the β-phase did not follow the Curie-Weiss behavior observed for the paramagnetic γ-phase, the β-phase was believed to be antiferromagnetic [23]. However, no evidence for antiferromagnetic order could be found in neutron diffraction experiments [33, 41]. Thereafter, Bean and Rodbell [25], as well as Goodenough and Kafalas [39], and others [38, 42, 43, 44] treated the first order phase transition as a ferromagnetic to paramagnetic transition.

More recently, density functional calculations have hinted at the possibility of antiferromagnetic ordering [36, 45, 46].

2.1.4 Elastic Constants

For a crystal of hexagonal symmetry, Hooke's law can be written in Voigt notation as [47]

$$
\begin{bmatrix} \sigma_{xx} \\ \sigma_{yy} \\ \sigma_{zz} \\ \sigma_{yz} \\ \sigma_{zx} \\ \sigma_{xy} \end{bmatrix} = \begin{bmatrix} c_{11} & c_{12} & c_{13} & 0 & 0 & 0 \\ c_{12} & c_{11} & c_{13} & 0 & 0 & 0 \\ c_{13} & c_{13} & c_{33} & 0 & 0 & 0 \\ 0 & 0 & 0 & c_{44} & 0 & 0 \\ 0 & 0 & 0 & 0 & c_{44} & 0 \\ 0 & 0 & 0 & 0 & 0 & c_{66} \end{bmatrix} \begin{bmatrix} \varepsilon_{xx} \\ \varepsilon_{yy} \\ \varepsilon_{zz} \\ \varepsilon_{yz} \\ \varepsilon_{zx} \\ \varepsilon_{xy} \end{bmatrix}, \tag{2.5}
$$

with the elastic stiffness tensor c_{ij}, strain ε and stress σ. Here, $c_{66} = \frac{c_{11}-c_{12}}{2}$. The compliance tensor $s_{ij} = c_{ij}^{-1}$ leads to the inverse relationship

$$\varepsilon = s\sigma. \tag{2.6}$$

The bulk modulus is given by

$$B = \frac{(c_{11} + c_{12})c_{33} - 2c_{13}^2}{c_{11} + c_{12} + 2c_{33} - 4c_{13}}. \tag{2.7}$$

The elastic compliance constants for α- and β-MnAs were determined by Dörfler on single crystalline whiskers [48] and are listed in Table 2.2. The slight orthorhombic distortion of the β-phase was ignored.

Stiffness [GPa]	c_{11}	c_{33}	c_{44}	c_{66}	c_{12}	c_{13}	B
α-MnAs	49.8	119	37.0	18.6	12.7	14.0	28.8
β-MnAs	41.0	112	34.5	16.1	8.7	10.7	23.1
Compliance [MPa^{-1}]	s_{11}	s_{33}	s_{44}	s_{66}	s_{12}	s_{13}	
α-MnAs	21.9	8.9	27	53.8	-5	-2	
β-MnAs	26.0	9.3	29	62.0	-5	-2	

Table 2.2: Elastic stiffness (c_{ij}) and compliance (s_{ij}) tensor elements and bulk modulus for bulk MnAs. The compliance values were taken from Dörfler and Bärner [48].

2.1.5 Related Materials

Besides MnAs, a number of other manganese pnictides have been studied for their magnetic properties.

	MnAs	MnP	MnSb	MnBi
	$P6_3/mmc$	Pnma	$P6_3/mmc$	$P6_3/mmc$
a [Å]	3.722		4.122	4.287 [49]
c [Å]	5.702		5.755	6.126
T_c [K]		292 [50]	588 [51]	633 [52]
$\mu_{eff}(T = 0K)$ [μ_B]	3.31 [53]		3.5 [54]	3.95 [52]

Table 2.3: Properties of magnetic manganese pnictides. The lattice parameters for the orthorhombic MnP are $a = 5.268$Å, $b = 3.173$Å, and $c = 5.918$Å.

MnN, MnP, MnSb, and MnBi

Like MnAs, the manganese pnictides MnN, MnP, MnSb and MnBi are also ferromagnetic (see Table 2.3). MnSb and MnBi posses the same hexagonal crystal structure (space group $P6_3$/mmc) as the α- and γ-phases of MnAs. MnP on the other hand possesses the slightly distorted orthorhombic "MnP" structure, i.e. the same structure as β-MnAs.

Mn-Ga Intermetallics

As the MnAs layers are grown on a GaAs substrate, in principle the formation of Mn-Ga intermetallics cannot be ruled out. A large number of stable intermetallic phases are known [30], several of which exhibit magnetic ordering [55, 56]. For the so-called δ-phase Mn_xGa_{1-x} ($x = 0.55 - 0.60$), Curie temperatures up to 658 K (depending on stoichiometry) have been reported [57]. This phase has indeed been grown epitaxially on GaAs [58, 59]. As we will see in Section 3.3.1, no evidence for crystalline MnGa was found in X-ray diffraction experiments.

2.2   Thin-Films

The growth of MnAs by molecular beam epitaxy (MBE) was first demonstrated by Tanaka in 1994 [60, 61]. In conventional heteroepitaxy of III-V semiconductors all materials have the same zincblende crystal structure, but differ in their lattice constant. In this respect, MnAs epitaxy is extraordinary, as it possesses hexagonal crystal structure, but can still be grown with good quality on a variety of substrates with cubic symmetry. To this date, growth on various orientations of GaAs, Si (001) [62], InP (001) [63, 64], and even highly oriented pyrolytic graphite (HOPG) [65] have been demonstrated.

In this dissertation, the focus will be on the most widely studied system: MnAs on GaAs (001). For a recent review of MnAs on GaAs with different substrate orientations, see the excellent paper by Däweritz [35].

Similar to GaMnAs, the growth of crystalline MnAs on GaAs is only possible at low enough substrate temperatures. For temperatures below 250°C, surface diffusivity for the adatoms becomes too low and results in amorphous material. As already noted by Tanaka, the orientation of the MnAs cell with respect to GaAs depends on the exact growth conditions during nucleation of the film, in particular on the arsenic coverage. An overview of the various epitaxial relationships obtained is shown in Figure 2.5.

In the following, we will focus on the most widely studied system: MnAs ($1\bar{1}00$) grown on GaAs (001) in the A_0 orientation, Figure 2.6, with [0001] parallel to GaAs [$1\bar{1}0$] and [$11\bar{2}0$] parallel to GaAs [110].

For this epitaxial relation, the following natural lattice mismatch can be derived:

$$f_{[110]} = \frac{d_{GaAs(220)} - d_{MnAs(11\bar{2}0)}}{d_{GaAs(220)}} = 6.9\% \tag{2.8}$$
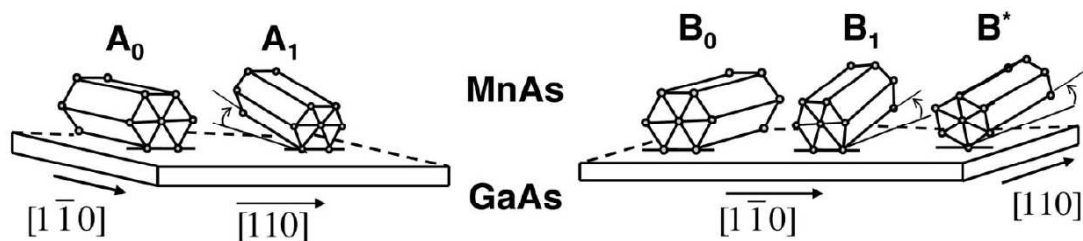
Figure 2.5: Epitaxial relationships observed for hexagonal MnAs grown on GaAs (001), taken from Iikawa et al. [66]. Reprinted with kind permission of the American Institute of Physics.
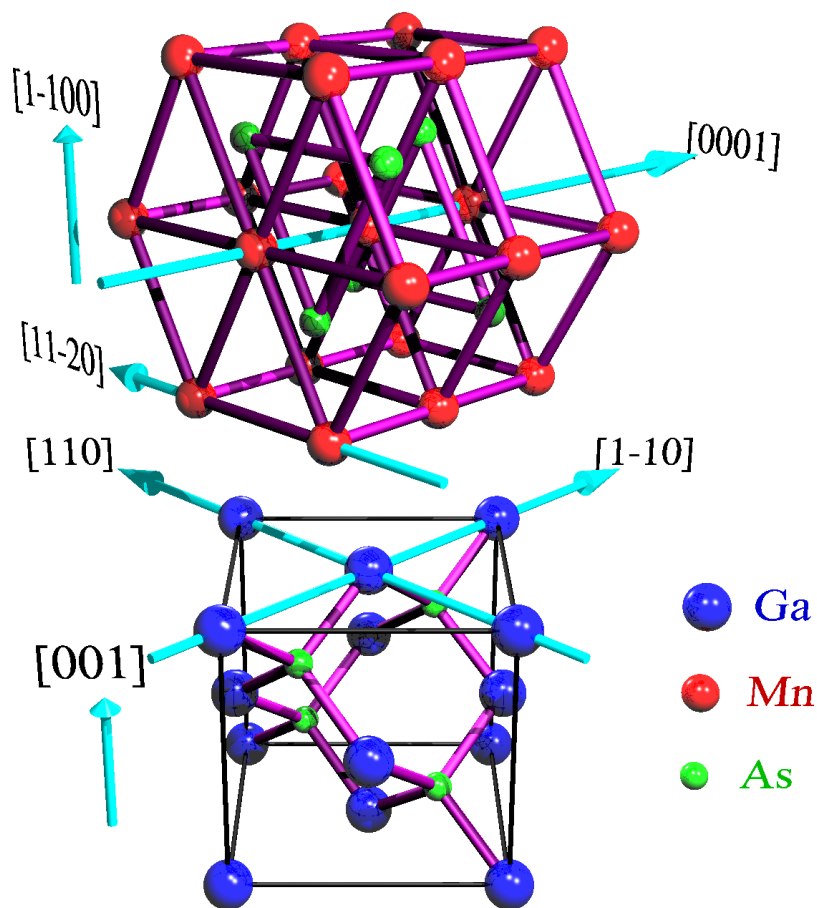
Figure 2.6: MnAs (A_0 orientation) on GaAs (001).

$$f_{[1\bar{1}0]} = \frac{d_{GaAs(1\bar{1}0)} - d_{MnAs(0002)}}{d_{GaAs(1\bar{1}0)}} = 29\% \tag{2.9}$$

These large mismatches lead to very small critical thickness, and therefore, relaxation occurs after only a few monolayers. It was shown by Satapathy [67] that the mismatch in the c-direction is reduced through a regular array of misfit dislocations, where every fourth MnAs (002) lattice plane coincides with every sixth GaAs (220) plane, thus reducing the strain to

$$f_{[1\bar{1}0]} = \frac{6d_{GaAs(1\bar{1}0)} - 4d_{MnAs(0002)}}{6d_{GaAs(1\bar{1}0)}} = 4.8\% \tag{2.10}$$

A secondary set of misfit dislocations with a 6 to 8 ratio reduces this misfit further, so that the strain at the growth temperature is near zero.

2.2.1 In-Plane Strain

Upon cooling, the epitaxial relationship between the MnAs film and the underlying substrates is thought to become fixed at critical temperature of about $T_0 = 150°C$ [68].

Then, assuming the thermal expansion of the MnAs film follows the thermal expansion of the GaAs substrate, the thin-film lattice constants are given by

$$a_{film}^{MnAs}(T) = \frac{a^{MnAs}(T_0)}{a^{GaAs}(T_0)} a^{GaAs}(T) \tag{2.11}$$

$$c_{film}^{MnAs}(T) = \frac{c^{MnAs}(T_0)}{a^{GaAs}(T_0)} a^{GaAs}(T). \tag{2.12}$$

From this, we find the in-plane strain versus temperature as

$$\varepsilon_a(T) \equiv \frac{a_{film}^{MnAs}(T) - a^{MnAs}(T)}{a^{MnAs}(T)} = \frac{a^{GaAs}(T)}{a^{GaAs}(T_0)} \frac{a^{MnAs}(T_0)}{a^{MnAs}(T)} - 1 \qquad (2.13)$$

$$\varepsilon_c(T) \equiv \frac{c_{film}^{MnAs}(T) - c^{MnAs}(T)}{c^{MnAs}(T)} = \frac{a^{GaAs}(T)}{a^{GaAs}(T_0)} \frac{c^{MnAs}(T_0)}{c^{MnAs}(T)} - 1. \qquad (2.14)$$

The resulting tensile strain is shown in Fig. 2.7.
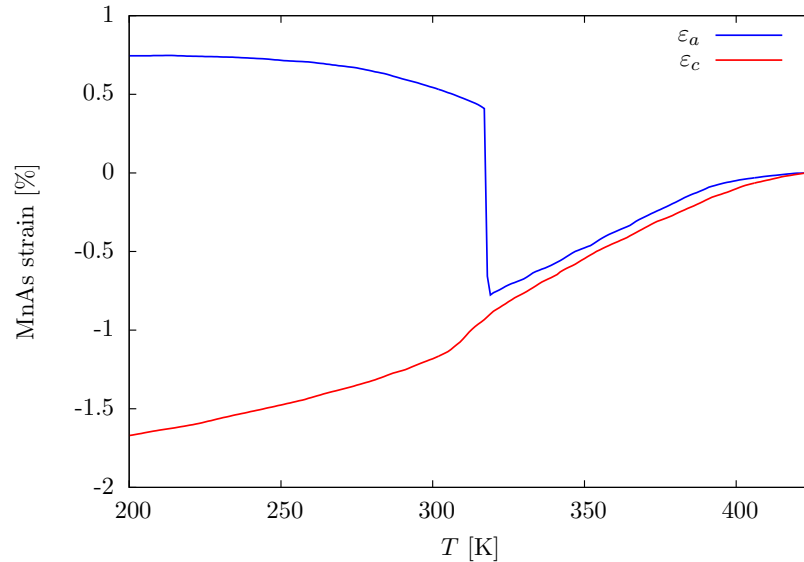
Figure 2.7: Strain versus temperature for the in-plane directions a and c of MnAs. The epitaxial relationship was assumed to be fixed and fully relaxed at 423 K (150°C). The GaAs lattice constant was taken from Ayers [47], MnAs lattice constants from Suzuki and Ido [31].

2.2.2   Phase Coexistence

Owing to the large difference in thermal expansion coefficients for MnAs and GaAs, tensile strain will build up in the MnAs layer upon cooling from the growth temperature. The β-phase with its larger lattice constant offers a way to lower the total

strain along the $[11\bar{2}0]$ direction. This leads to the phase coexistence regime, where α- and β-phase of MnAs form a regular array of stripes. A model for this phase coexistence has been developed by Kaganer et al. [69, 70]. The basic assumption is that the in-plane mean total strains $\bar{\varepsilon}_{xx}$ and $\bar{\varepsilon}_{yy}$ are zero due to lateral constraints of the substrate. With the relative phase fractions f_α and f_β these conditions can be written as:

$$\bar{\varepsilon}_{xx} = f_\alpha \varepsilon_{\alpha,xx} + f_\beta \varepsilon_{\beta,xx} = 0 \tag{2.15}$$

$$\bar{\varepsilon}_{yy} = f_\alpha \varepsilon_{\alpha,yy} + f_\beta \varepsilon_{\beta,yy} = 0 \tag{2.16}$$

The surface of the film, however, is unconstrained and hence the stress σ_{zz} normal to the film is zero.

The free energy of the film is given as

$$F = f_\alpha (F_\alpha + E_\alpha^{el}) + f_\beta (F_\beta + E_\beta^{el}), \tag{2.17}$$

with the free energies of the phases $F^{\alpha,\beta}$ and elastic strain energy

$$E_a^{el} = Y \left(e_{a,xx}^2 + 2\nu e_{a,xx} e_{a,yy} + e_{a,yy}^2 \right). \tag{2.18}$$

Minimization of the free energy with respect to f_α leads to the equilibrium phase fraction

$$f_\alpha = -\frac{\Delta F}{2Y\eta^2}. \tag{2.19}$$

If the detailed structure of the film is assumed to be periodic, a Fourier expansion can be used to calculate the normal displacements within the domains [70, 71, 72]. The result of such a calculation, shown in Fig. 2.8, illustrates the surface modulation encountered in the phase-coexistence regime of MnAs. The stripe periodicity Λ is known to be proportional to the film thickness t, with $\Lambda \approx 4.8 \cdot t$ [35]. This scaling
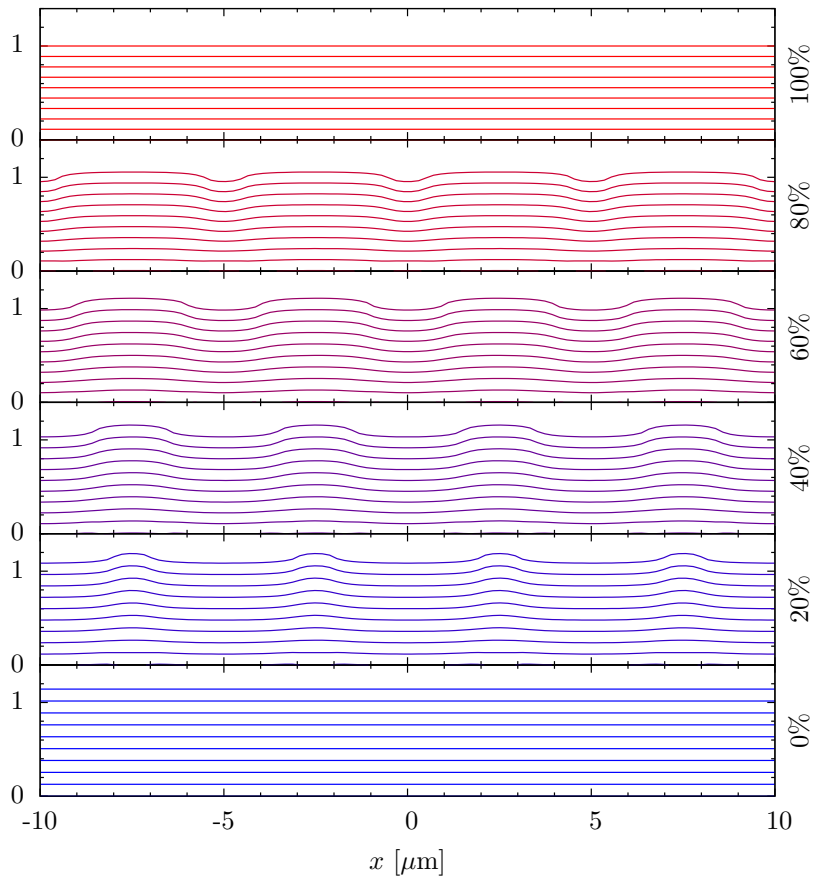
Figure 2.8: Calculated vertical displacements of a 1 μm thick film with 5 μm periodicity for different phase fractions. The assumed misfit of 1% is applicable for the MnAs α- to β-transition. For clarity, the displacement is scaled by a factor of 10.

is the result of the competing elastic energies along the GaAs/MnAs interface and α- and β-domain interfaces [70].

The phase-coexistence can also be observed for other epitaxial orientations. For MnAs(0001)/GaAs(111)B the transition is found to proceed over a temperature range from about 313 to 323 K [73]. As a consequence of the isotropic strain conditions (the hexagonal plane lies in the growth plane), periodic striped structures are not observed.

2.3 Magnetism

In the following, we give a quick review of some of the important concepts in magnetism which will be relevant in the following chapters. A more detailed discussion can be found in most textbooks on magnetism, see for example [74, 75].

In general, the magnetic induction $\vec{B}$ is related to magnetic field $\vec{H}$ and magnetization $\vec{M}$ by

$$\vec{B} = \mu_0(\vec{H} + \vec{M}). \tag{2.20}$$

Due to the difference in units in the SI-system between B (Tesla) on the one hand, and H and M (in A/m) on the other hand, in practice one often uses

$$\vec{B} = \vec{B_{ext}} + \vec{I}, \tag{2.21}$$

with the definitions $\vec{B_{ext}} \equiv \mu_0\vec{H}$ for the external (applied) field and the magnetic polarization $\vec{I} \equiv \mu_0\vec{M}$, see for example [76, 77].

The magnetic susceptibility tensor χ of a non-ferromagnetic medium is formally defined by

$$\vec{M} = \chi\vec{H}. \tag{2.22}$$

2.3.1 Paramagnetism

Isolated, localized spins in an external magnetic field experience the Zeeman splitting of their energy levels

$$E_m = -\vec{\mu} \cdot \vec{B}, \tag{2.23}$$

where the moment is given by

$$\mu = g\mu_B m_S, \tag{2.24}$$

with Bohr magneton μ_B and Landé-factor $g = 1 + \frac{J(J+1)+S(S+1)-L(L+1)}{2J(J+1)}$.

From thermodynamics, one can derive from this the magnetization of an ideal paramagnet as

$$M = Ng\mu_B J B_J(x), \tag{2.25}$$

with the dimensionless parameter $x = g\mu_B J \frac{H}{k_B T}$, and the Brillouin function

$$B_J(x) = \frac{2J+1}{2J} \coth\left(\frac{2J+1}{2J}x\right) - \frac{1}{2J}\coth\left(\frac{1}{2J}x\right). \tag{2.26}$$

A plot of Eqn. 2.26 for different values of J is shown in Fig. 2.9. The saturation behavior observed for $x \geq 1$ is usually only encountered for very low temperatures or very strong fields. For $x \ll 1$, one may approximate the zero-field susceptibility as

$$\chi = \frac{C}{T}, \tag{2.27}$$

where C is the Curie constant.
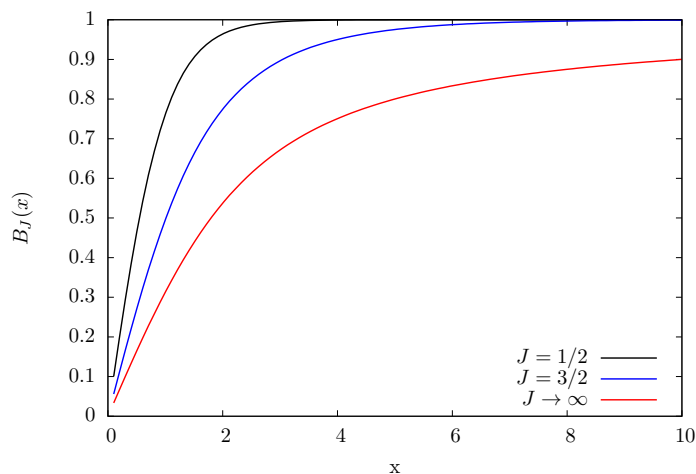
Figure 2.9: Plot of the Brillouin function $B_J(x)$ for $J = 1/2$, $J = 3/2$, and $J \to \infty$.

The assumption of completely non-interacting spins is valid only in dilute spin-systems. For practical paramagnets, one instead finds the Curie-Weiss law

$$\chi = \frac{C}{T - T_c},\tag{2.28}$$

where T_c describes the magnetic ordering temperature of the system.

In a real solid, in particular a metal, the electrons are not fully localized and thus one has to consider band-effects. As a consequence, relation 2.24 does not hold anymore and one introduces an effective moment μ_{eff} instead. For MnAs in particular, the following parameters have been reported: $J = 3/2$, $g = 2.27$, and $\mu_{eff} = 3.4\mu_B$ [78].

2.3.2   Ferromagnetism

In a solid, magnetic moments are coupled to each other through quantum-mechanical exchange interactions. While direct (dipole-dipole) interactions couple neighboring spins, indirect exchange mechanisms such as the Rudermann-Kittel-Kasuya-Yosida (RKKY) interaction can mediate coupling between more remote moments. In effect, if the coupling is of the right sign and sufficiently strong, magnetic moments will order below some Curie temperature to yield a spontaneous magnetization M_s. In describing this ordering, one commonly resorts to effective-field theories, where the role of the exchange interactions is lumped together into an exchange-field B_{ex}. This treatment also leads directly to the Curie-Weiss law (Eq. 2.28), which then gives the susceptibility of the material above its Curie temperature.

2.3.3   Antiferromagnetism

If the sign of the exchange coupling favors antiparallel alignment, it is possible for the moments to form an ordered antiferromagnetic state with neighboring moments

in antiparallel alignment. Commonly employed models typically consider a set of two (or more) sublattices with ferromagnetic order within each sublattice, but the total magnetization canceling because of the antiparallel alignment of the sublattices. The net magnetization of such a system is linear in the applied field as in a paramagnet, and unlike in ferromagnetism, there is no net magnetization at zero field. Therefore, from magnetization and susceptibility measurements it is very hard to find conclusive evidence of antiferromagnetism, and the only reliable way to directly detect the antiferromagnetic order is through neutron scattering.

2.3.4   Magnetic Anisotropy

Magnetic materials, in particular ferro- and antiferromagnets, are generally not isotropic.

Shape Anisotropy and Demagnetization

The magnetostatic energy is given by the volume integral

$$E = -\frac{1}{2} \int \vec{M}(\vec{r}) \cdot \vec{H}(\vec{r}) d\vec{r}. \tag{2.29}$$

For a *uniformly* magnetized material, the internal field may be written as

$$\vec{H}_{internal} = -N \cdot \vec{M}, \tag{2.30}$$

with the demagnetizing tensor (or factor) N. Demagnetization factors in textbooks are usually only given for simple geometric shapes like spheres and ellipsoids. For an infinitely thin film, the perpendicular demagnetization factor N_z is 1, while the in-plane demagnetization factors $N_x = N_y = 0$. General analytical expressions for rectangular prisms have been derived only recently [79]. For an infinitely long prism

of height h and width w and aspect ratio $p = \frac{h}{w}$, these simplify to

$$N_z = \frac{1}{\pi} \left(\frac{1 - p^2}{2p} \ln(1 + p^2) + p \ln p + 2 \arctan \frac{1}{p} \right) \tag{2.31}$$

A plot of the demagnetization factor N_z versus h/w is shown in Fig. 2.10.
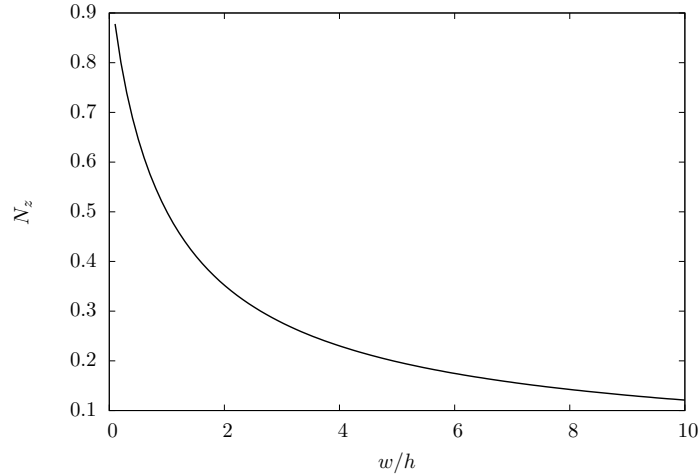
Figure 2.10: Plot of the demagnetization factor N_z for infinitely long stripes of width w and height h.

Magnetocrystalline Anisotropy

The spin-orbit interaction is a major factor in the magnetic anisotropy. For a hexagonal crystal, the anisotropy energy is usually approximated as [74]

$$E = \int K_1 \sin^2 \Theta(\vec{r}) + K_2 \sin^4 \Theta(\vec{r}) + K_3 \sin^6 \Theta(\vec{r}) d\vec{r}, \tag{2.32}$$

where $\Theta(\vec{r})$ is the angle between the magnetization $\vec{M}(\vec{r})$ and the hexagonal c-axis. For MnAs, De Blois and Rodbell found $K_1 = -5.75 \cdot 10^5$ J/m^3, $K_2 = 1.5 \cdot 10^5$ J/m^3, and $K_3 = -1.15 \cdot 10^5$ J/m^3 at 35°C [38, 42].

A plot of the anisotropy energy density is shown in Fig. 2.11. The minimum in energy is for $\Theta = 90°$, i.e. the magnetically easy direction is in the hexagonal plane, while the c-axis ($\Theta = 0°$) of MnAs is magnetically hard.
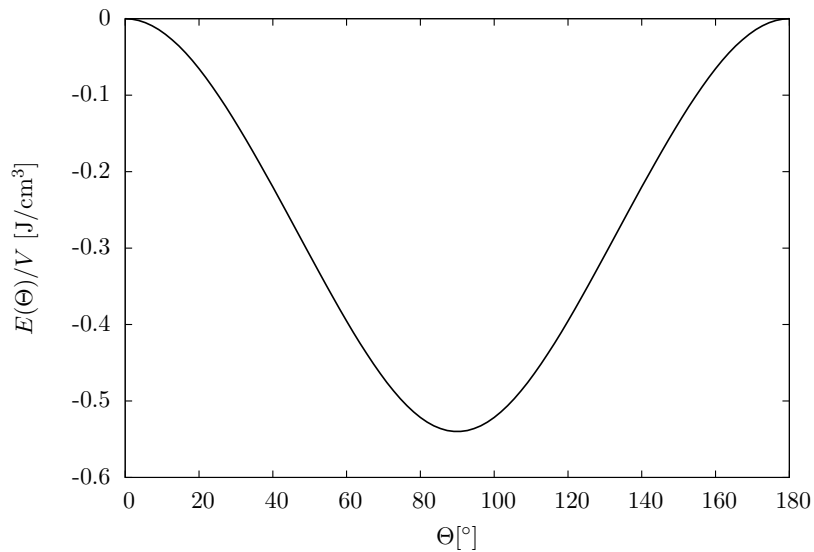
Figure 2.11: Magnetocrystalline anisotropy energy density for MnAs.

Additional contributions to the anisotropy may arise from surfaces, because the otherwise perfect translational periodicity of the crystal is broken.

2.4 Hall Effect and Anomalous Hall Effect

The ordinary Hall effect is a result of the Lorentz-force of an applied magnetic field $\vec{H}$ acting on moving charge carriers (electrons or holes) in a solid. The deflection of carriers leads to a charge imbalance, and thus to an electric field $\vec{E}$ that — under steady state conditions — balances the magnetic force

$$q\vec{v} \times \vec{B} = q\vec{E}. \tag{2.33}$$

In a rectangular geometry with symmetric contacts illustrated in Fig. 2.12, one

can measure the Hall Voltage V_{xy} and derive the Hall resistance ρ_{xy}

$$\rho_{xy} = \frac{V_{xy}}{I} t \tag{2.34}$$

if transport is assumed to be homogeneous over a known film-thickness t.
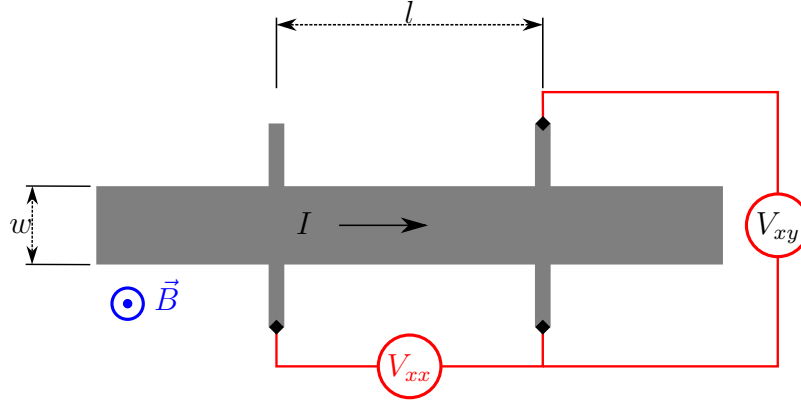
Figure 2.12: Classical Hall-bar geometry.

In the same geometry, the sheet resistance is given as

$$\rho_{xx}^{sheet} = \frac{V_{xx}}{I} \frac{w}{l}, \tag{2.35}$$

where the bulk value can again be determined by $\rho_{xx} = t \cdot \rho_{xx}^{sheet}$.

In a simple, single band picture, the Hall resistivity is connected to the density n of carriers with charge q through the Hall constant:

$$R_H \equiv \frac{\rho_{xy}}{B} = \frac{1}{n \cdot q}. \tag{2.36}$$

From these two measurements, the carrier mobility μ is then found as

$$\mu = \frac{V_{xy}}{V_{xx}} \frac{l}{w} \frac{1}{B}. \tag{2.37}$$

Soon after the discovery of the Hall effect, it became clear that for a magnetic material there is an additional "anomalous" contribution to the Hall effect [80]:

$$\rho_{xy} = R_0 B_z + R_S \mu_0 M_z, \tag{2.38}$$

where $R_0 = \frac{1}{n \cdot q}$ is the normal Hall constant, R_S is the spontaneous Hall constant, M_z is the out-of-plane component of magnetization.

It has to be pointed out here, that this additional contribution exists even in paramagnetic substances. Indeed, for a material with a small ordinary Hall coefficient (high doping), high resistivity (low mobility), and a significant concentration of paramagnetic ions, the anomalous contribution may be dominant. A prime example is the dilute magnetic semiconductor $Ga_{1-x}Mn_xAs$.

While for *non-magnetic* materials the linear relation $B_z = \mu_0 H_z^{ext.}$ holds, for a *magnetic* material the internal magnetic field contains a contribution from the magnetization:

$$B_z = \mu_0(H_z^{ext.} + (1 - N_z)M_z). \tag{2.39}$$

Here, the demagnetizing field (see Section 2.3.4) has to be taken into account. In the limiting case of a continuous thin-film one finds $N_z \approx 1$ and relationship 2.38 simplifies to

$$\rho_{xy} = R_0 \mu_0 H_z + R_S \mu_0 M_z. \tag{2.40}$$

2.4.1 Phenomenology

Phenomenologically, it has been known that the spontaneous Hall constant R_S is dependent on the sheet resistivity ρ_{xx} in the following form:

$$R_S = c \cdot \rho_{xx}^\gamma. \tag{2.41}$$

Here, in typical experiments the exponent γ is found to be either 1 or 2, depending on the system under consideration. The proportionality constant c is usually taken to be temperature independent. Considering the availability of theoretical models

for $\gamma = 1$ and $\gamma = 2$, the following form is also quite commonly encountered:

$$R_S = c_1 \cdot \rho_{xx} + c_2 \cdot \rho_{xx}^2. \tag{2.42}$$

For large ρ_{xx} the anomalous Hall effect is often the dominant contribution and one can neglect the ordinary Hall effect. Then, through eqn. 2.40, the anomalous Hall effect can be utilized as a sensitive magnetometer for the thin-film. In particular for low fields, the susceptibility of the sample can be approximated as

$$\chi_{zz} \equiv \frac{dM_z}{dH_z} \approx \frac{1}{R_S \mu_0} \frac{d\rho_{xy}}{dH_z} = \frac{1}{R_S} \frac{d\rho_{xy}}{dB_z^{ext.}}. \tag{2.43}$$

We will make use of this relation in Chapter 4 to deduce the susceptibility of the α-phase.

2.4.2 Theoretical

Despite its early discovery, a theoretical understanding of the anomalous Hall effect (AHE) had not been developed until the 1950s and has remained sketchy.

The empirical dependence of R_S on ρ (Eqn. 2.42) might lead one to assume that the AHE must be intimately connected to scattering. That this is not necessarily so can be seen by focusing instead on the Hall conductivity $\sigma_{xy} = \frac{\rho_{xy}}{\rho_{xx}^2 + \rho_{xy}^2} \approx \frac{\rho_{xy}}{\rho_{xx}^2}$. Assuming $R_S \sim \rho_{xx}^2$, we find that the anomalous Hall conductivity term $\sigma_{xy}^{AHE} = \frac{R_S}{\rho_{xx}^2} \mu_0 M_z$ does not have an explicit dependence on σ_{xx}, i.e. no dependence on a scattering time τ.

A first theory of the AHE was developed by Karplus and Luttinger [81], based on the spin-orbit interaction. Their theory predicted an anomalous velocity perpendicular to the applied electric field contribution to the Hall effect, with the associated ρ^2 dependence of the extraordinary Hall constant.

This "intrinsic" explanation of the AHE was rejected by Smit [82, 83], who, using a semiclassical approach, developed a theory based on impurity scattering due to the spin-orbit interaction. His theory contained contributions of both ρ^1 dependence, termed the "skew-scattering" mechanism, as well as the ρ^2 dependence. This second contribution, neglected by Smit, was later resurrected by Berger [84] as the "side-jump" mechanism and was considered the primary AHE mechanism for the next decades.

Only recently, the connection of Karplus and Luttinger's anomalous velocity to Berry's phase [85] arguments has been realized [86, 87, 88, 89, 90] and has been termed the "intrinsic" contribution.

In practice, it is of course not easily possible to distinguish between the intrinsic and the side-jump mechanism since both lead to a ρ^2 dependence. The general view is that skew scattering mechanism dominates for highly conductive ($\sigma > 10^6 (\Omega\text{cm})^{-1}$) ferromagnets, while for moderately conductive (10^4 - $10^6 (\Omega\text{cm})^{-1}$) materials the intrinsic and side-jump mechanisms give rise to a $R_S \sim \rho^2$ dependence. The conductivity of MnAs is about 2 to $5 \cdot 10^5 (\Omega\text{cm})^{-1}$, placing it within the ρ^2 regime.

An extensive review of recent theoretical and experimental work concerning the AHE is given in Nagaosa et al. [91].

2.4.3   Inhomogeneous Media

In an inhomogeneous medium, the Hall effect can be treated using effective media theory. Expressions for the effective conductivity tensor in a parallel slab geometry, appropriate in the phase-coexistence regime, are given in Section 4.3. For a similar derivation, see also Mityushov et al. [92].

With the increasing technological importance of the applications of multilayered

magnetic structures, studies of the AHE in these inhomogeneous systems have become an important subject.

Using Kubo theory, Zhang [93] investigated side-jump scattering in multilayer structures for three different geometries (current in plane, magnetic field perpendicular or in-plane, current perpendicular to plane) and found that the usual scaling relation 2.42 does not hold in the case of "extended scattering". In the "local limit" (i.e. mean free path length smaller than layer thickness), however, the scaling relations are expected to be valid.

Reported mean-free paths for holes in MnAs are between 18 and 225 nm at 0.3 K [94] and are certainly significantly smaller at room temperature. Therefore, within the phase-coexistence region, the local limit may be applicable and the scaling relation may hold.

Chapter 3

Growth of MnAs

3.1   Molecular Beam Epitaxy of MnAs

In conventional III-V heteroepitaxy all the constituent alloys (e.g. InAs, InSb, AlAs, GaAs, InP, GaSb) have the same crystal structure and differ only in their lattice constant. MnAs on GaAs, on the other hand, presents an extreme case of heteroepitaxy, the two have different crystal structures, namely hexagonal for MnAs and zincblende for GaAs. Nevertheless, it is possible to achieve epitaxial growth of MnAs on a variety of substrates under the right conditions. The growth of MnAs on GaAs (001) was pioneered by Tanaka in 1994 [60]. Since then, various groups have demonstrated growth on other substrates of cubic symmetry, namely Si (001) [62] and InP (001) [63], as well as on different GaAs substrate orientations: GaAs (110), GaAs (113A) [95], and GaAs (111)A&B [73, 96, 97].

3.1.1 Substrate Temperature

A big challenge in growing MnAs films is the low growth temperature required, typically about 250°C. Films grown at higher temperature usually turn out poly-crystalline, films grown at a lower temperature turn amorphous.

High quality growth of GaAs typically takes place at about 580 to 600°C and temperature calibration and monitoring in this regime is easily accomplished using infrared emission pyrometry. Temperature control at lower temperatures is more difficult for several reasons:

- Radiative heating of the substrate from the Knudsen sources becomes very significant.

- Infrared emission from the sources may give erroneous readings on the pyrom-eter [98].

- MnAs is metallic. Therefore, absorption of infrared radiation varies with film thickness.

- Thermal time constants are much longer than during high temperature growth.

In our MBE system, the substrate thermocouple was shorted out and could not be used for temperature control. As repairs were deemed too risky due to the uncertainty of component availability and past experience [1] had indicated poor control stability around 250°C, we decided to instead perform the temperature regulation manually, i.e. by setting a constant output power on the heater power supply.

Temperature calibration was established individually for each wafer by correlat-ing temperature readings from the pyrometer above 400°C with the applied heater

---

[1]Abdel-Rahman El-Emawy, personal communications.

power. Figure 3.1 shows the relationship between heater control voltage and pyrometer temperature reading for about 30 growth runs on substrates of different sizes. For the growth on $\frac{1}{4}$ x 2" semi-insulating (S.I.) wafers, significant differences were observed for the two different wafer holders ("LL1" and "LL2") employed for these growths. After repeated use of both holders, the difference became smaller. Holders with full 2-inch wafers, as well as n-doped substrates, behave completely differently and require separate calibrations.
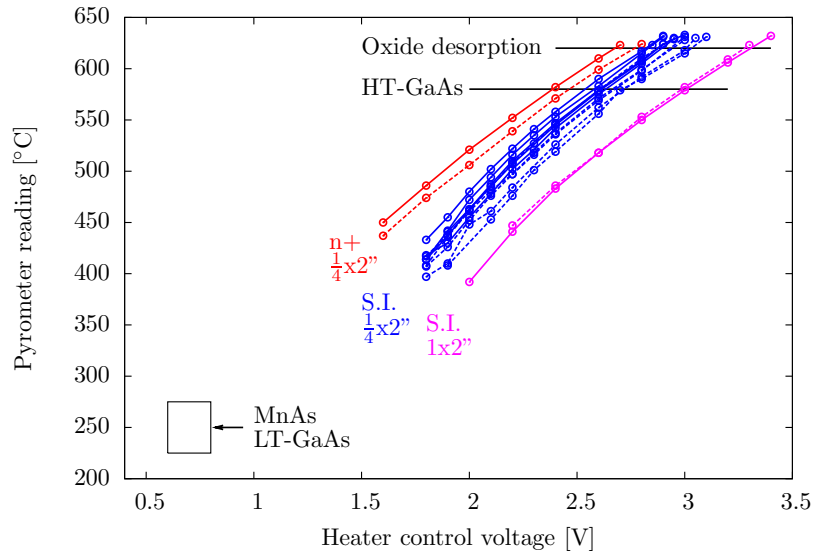
Figure 3.1: Heater control voltage versus pyrometer reading for a number of growth runs. Solid and dashed blue lines represent wafer holders "LL1" and "LL2". The temperatures for oxide desorption and high-temperature (HT) GaAs growth are also shown. The rectangle in the lower left represents the target temperature range for MnAs and low-temperature (LT) GaAs growth.

3.1.2 Basic Growth Procedure

Since the MBE system was not equipped with a preparation chamber, samples were transfered from the load-lock into the growth chamber the evening before growth. Outgassing was performed overnight at temperatures up to about 350°C with the

sample oriented away from the source flange. The next day, oxide desorption was performed at 630°C under an As_4 beam equivalent pressure (BEP) of $1.2 \cdot 10^{-5}$ mbar for about 10 minutes, before the substrate temperature was lowered to 580°C for the growth of high-temperature GaAs. At this point, the Ga shutter was opened to deposit a buffer layer of 300 nm GaAs at a growth rate of 1 μm/h. To reduce the chance of formation of GaMn intermetallics, the cell temperature of gallium was rapidly ramped down to the idle point once the growth of GaAs buffer layers had been completed. Then, the substrate temperature was lowered to about 250°C while keeping the As_4 shutter open and simultaneously ramping the As_4 cell temperature to the new setpoint required for nucleation of MnAs. After stabilization of the substrate temperature, the growth of MnAs was initiated by opening the Mn shutter. After completion of the growth, substrate temperature was slowly lowered to room temperature, with the arsenic shutter in the open position until the sample had cooled below ≈ 200°C.

3.2 Growth Optimization

Early growth attempts for MnAs, performed by Drs. Abdel-Rahman El-Emawy and Andreas Stintz, had already shown 2-dimensional growth, as evidenced by streaky reflection high energy electron diffraction (RHEED) patterns. However, investigation of the samples by AFM showed a large number of voids in these MnAs thin-films and the typical stripe pattern was not observed. Similar holes have also been reported in AFM scans of films that were annealed at ≈ 400°C [99, 100], possibly as a result of arsenic loss. Because the observed holes were very deep, and there was no indication of the growth temperature being chosen too high, it was suspected that the problem was caused either during nucleation of the films or during coalescence in the early stages of growth. To improve the quality of the films, several different

growth parameters and variations of growth procedure were explored.

3.2.1   Arsenic Overpressure

As has been noted in the literature, As_4 overpressure is a critical factor in the nucle-ation of MnAs on GaAs. We found that for successful nucleation an As_4 to Mn BEP ratio of about 400 was required. Lower overpressures yielded films with significant contents of MnAs in A_1 or B_1 orientation.

3.2.2   Growth Rate

Another significant factor for nucleation is the choice of growth rate. Typical reported growth rates are ≈ 10 nm/h [101], very low compared to the usual ≈ 1 μm/h in III-V growth. The low growth rate may also lead to increased incorporation of impurities.

We speculated, that after initial nucleation at a low growth rate, it might be possible to increase the growth rate and thus achieve better material quality for the remainder of the film. To test this, the normal growth procedure was modified in the following way: After 15 minutes of low growth rate MnAs growth, the cell temperatures of both As_4 and Mn were ramped up over a 15 minute interval to obtain a flux 2.5 times the low-growth rate flux. For comparison, samples were also grown with only the low growth rate and only the high growth rate.

3.2.3   Growth Interrupt and Buffer Layer

The cooldown from 580°C to 250°C in our reactor takes about 60 minutes. During this time, contamination of the growth surface from background is likely. As a possible strategy to reduce this effect we explored the insertion of an additional low

temperature grown GaAs layer to bury these impurities. Furthermore, since the temperatures of the Ga and Mn cells are comparable, the radiative heating from the Ga cell may help to stabilize the substrate temperature. This growth procedure is shown schematically in Fig. 3.2.
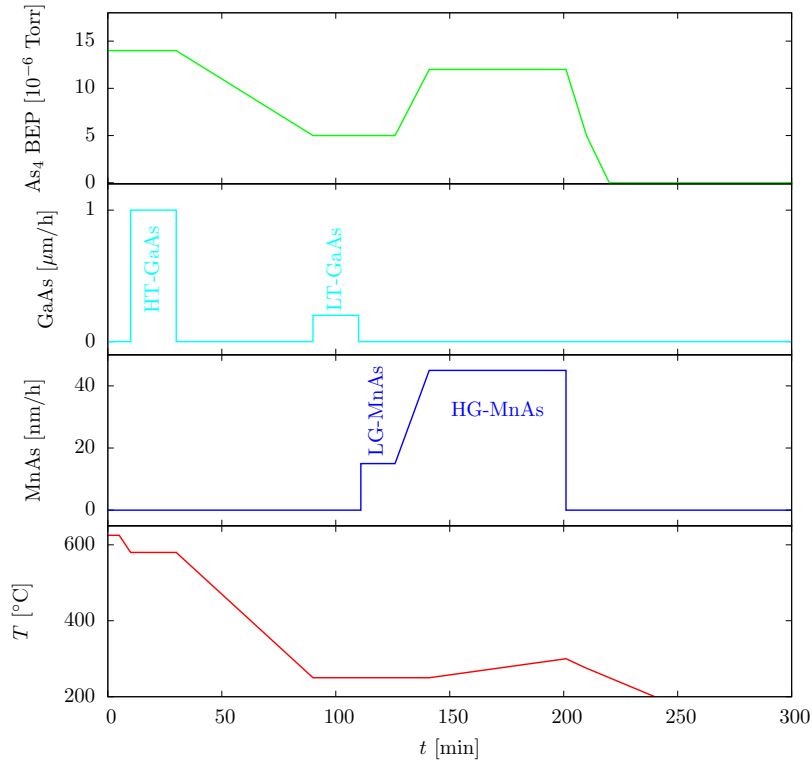
Figure 3.2: Schematic illustration of the growth procedure used for growing MnAs thin-films. "HT-GaAs" and "LT-GaAs" denote the high and low temperature GaAs buffers, while "LG-MnAs" and "HG-MnAs" refer to low and high growth rate MnAs respectively.

3.2.4 Growth Monitoring by RHEED

The entire growth process was monitored by RHEED and recorded for some samples using a commercial video camera. The typical d(4x4)-surface RHEED pattern of

GaAs disappeared after about 120 seconds of growth, and in good samples, faint streaks of the MnAs (1x2) reconstruction appeared after another 30 seconds. As growth proceeded the intensity of the streaks became more pronounced and persisted until the growth was terminated, indicating a 2-D growth mode. Typical RHEED patterns of GaAs and MnAs (A_0 oriented) recorded during growth are shown in Fig. 3.3.

3.3   Structural Characterization

To evaluate the quality of all samples, X-ray diffraction (XRD) and reflection (XRR), as well as atomic force microscopy (AFM) were employed. In the following, only a subset of data for a few representative samples will be shown.

3.3.1   X-Ray Diffraction

To assess the quality of the growth, extensive X-ray characterization was performed on each sample. Figure 3.4 shows typical high-resolution XRD scans obtained for two different samples.

Two separate peaks for the α-MnAs ($1\bar{1}00$) and β-MnAs (020) reflections are clearly resolved. For the sample that was annealed during growth (TE577), an extra reflection, corresponding to the tilted A_1 or B_1 orientations is found just to the right of the GaAs (002) peak. The structure factor for this reflection is substantially larger than the one of the ($1\bar{1}00$) reflection and thus even small amounts of out-of-plane orientation can be detected. Therefore, all samples were screened for this feature.

In Fig. 3.5 we show AFM scans obtained for these two samples. While the classic stripe pattern is observed for TE578, in sample TE577 grains of two orthogonal
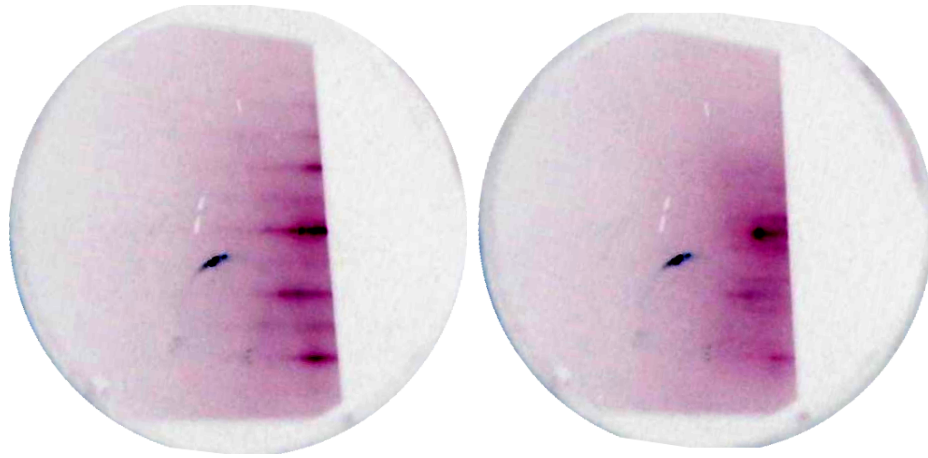
(a) HT-GaAs
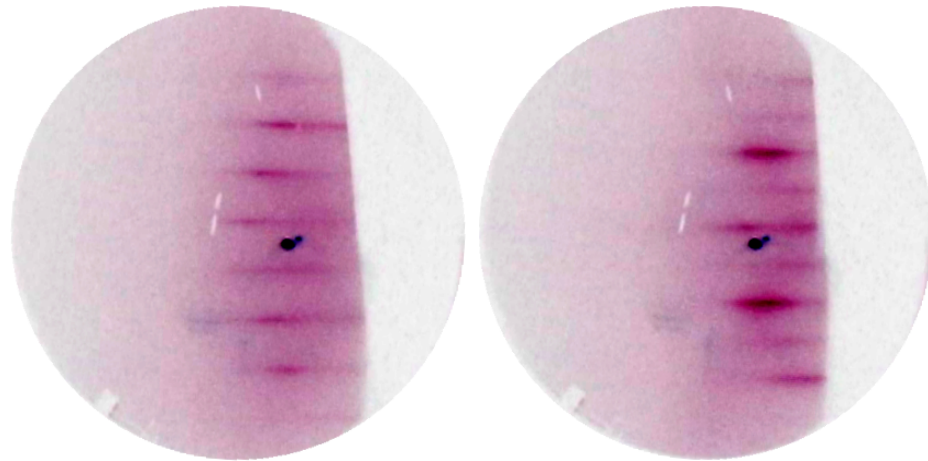
(b) MnAs

Figure 3.3: RHEED patterns of the GaAs (2x4) (a) and MnAs (1x2) (b) reconstructions, recorded using a camcorder during rotated growth. For clarity, the images have been inverted. The dark spot near the center is due to reflection of ambient light from the camera lens housing.

orientations are present, pointing at the presence of both A and B epitaxial orientations.

In Chapter 4, we will use the relative intensities of the MnAs reflection pair to determine the phase fraction across the α- to β-transition.
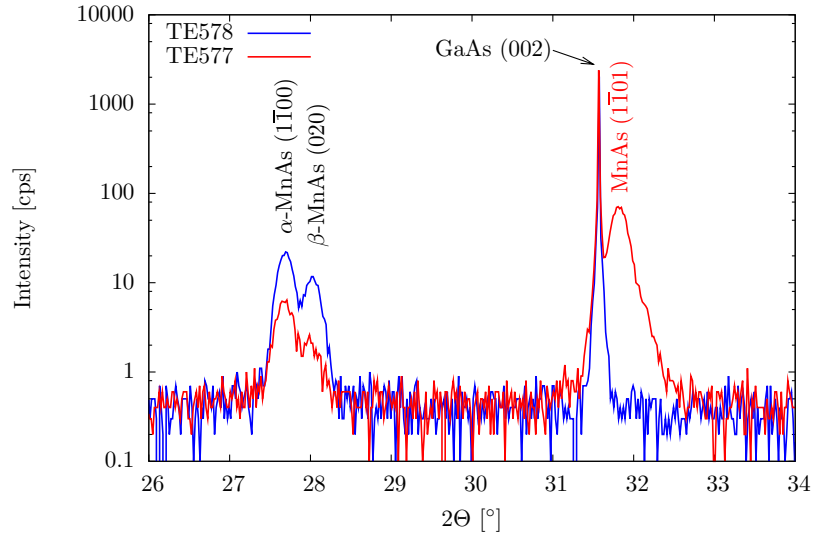
Figure 3.4: HR-XRD scans of samples TE577 and TE578.

(a) TE577   (b) TE578
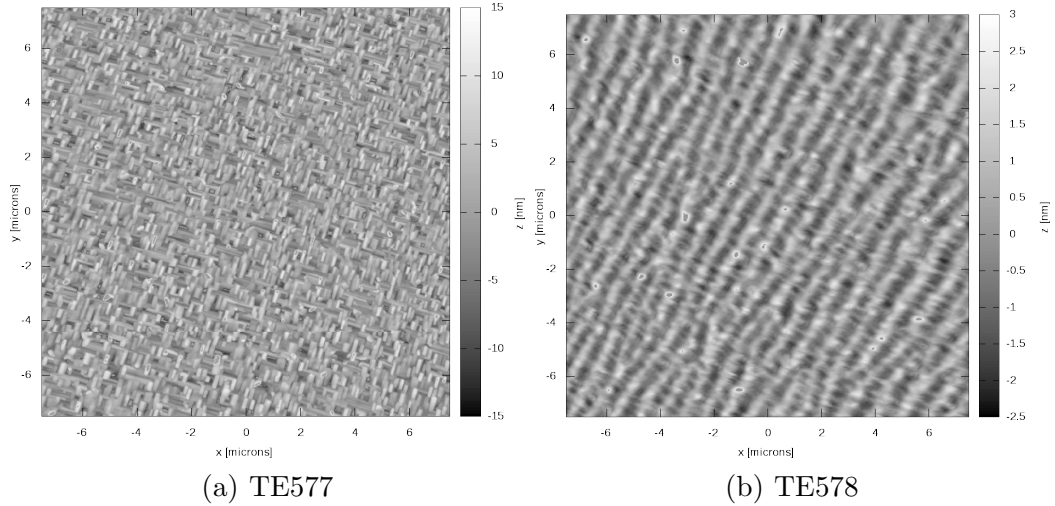
Figure 3.5: AFM scans of samples TE577 and TE578.

Phase Purity

While it is impossible to rule out the presence of unwanted other phases using XRD, we performed wide-range diffraction experiments to check for extra diffraction peaks. For improved sensitivity, a powder-diffractometer (described in more detail in Sec-

tion 4.2.1) with non-monochromatic beam and multi-pixel detector was used. In Fig. 3.6 we show one such scan, obtained on sample TE581.
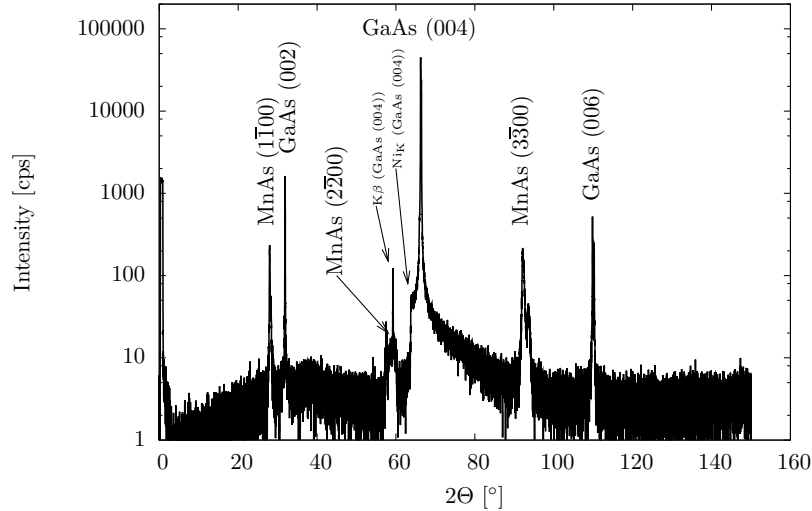
Figure 3.6: Large range diffraction scan of sample TE581, recorded using a powder-diffractometer.

Multiple diffraction orders of GaAs and MnAs reflections are clearly identifiable. The vertical 'jump' just to the left of the GaAs (004) reflection is due to sharp K-absorption edge of the nickel filter ($\lambda_{Ni} = 1.4886$ Å) used in this measurement. Due to the incomplete absorption of the Cu-K$_\beta$ radiation, a weaker ghost of the GaAs (004) peak is observed overlapping the MnAs ($2\bar{2}00$) reflection. Aside from these peaks, no further peaks of significant intensity are discernible.

Reciprocal Space Mapping

In Fig. 3.7 we show reciprocal space maps of the MnAs ($1\bar{1}00$)/(020) reflection pair at three temperatures over the phase-coexistence range for sample TE578. Reciprocal space maps for other samples are very similar. No significant difference in the FWHM is observed between the three temperatures.

(a) 276 K   (b) 305 K   (c) 330 K
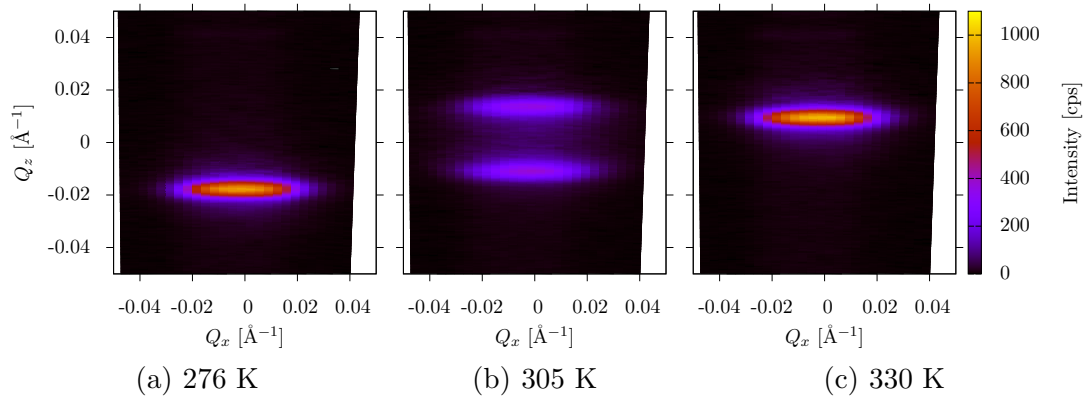
Figure 3.7: Reciprocal space maps of the MnAs ($1\bar{1}00$) and (020) reflections at 276 K (entirely α-phase), 305 K (roughly equal α- and β-phase), and 330 K (entirely β-phase).

Uniformity

For the experiments detailed in the following chapters, in many cases different pieces of the same wafer were used for the different characterization techniques. It is therefore important to gain a clear understanding of the uniformity (in terms of film thickness and growth temperature) of the material. Unfortunately, the weak structure factors of MnAs and long scan times required for XRR measurements make this impractical. Instead, we can use uniformity data obtained for a series of $Ga_{1-x}Mn_xAs$ films grown under similar conditions. The lattice constant of $Ga_{1-x}Mn_xAs$ depends not only on the Mn concentration, but also on the densities of defects such as As antisites (As_{Ga}) and interstitial Mn (Mn_I) [102, 103]. Nonetheless, the approximate composition can still be determined from a measurement of the lattice constant, assuming the validity of Vegard's law

$$a = x \cdot a_{MnAs} + (1 - x) \cdot a_{GaAs}, \tag{3.1}$$

with the lattice constants $a_{GaAs} = 5.6553$ Å and $a_{MnAs} = 5.90$ Å [104] for a hypothetical zincblende MnAs.
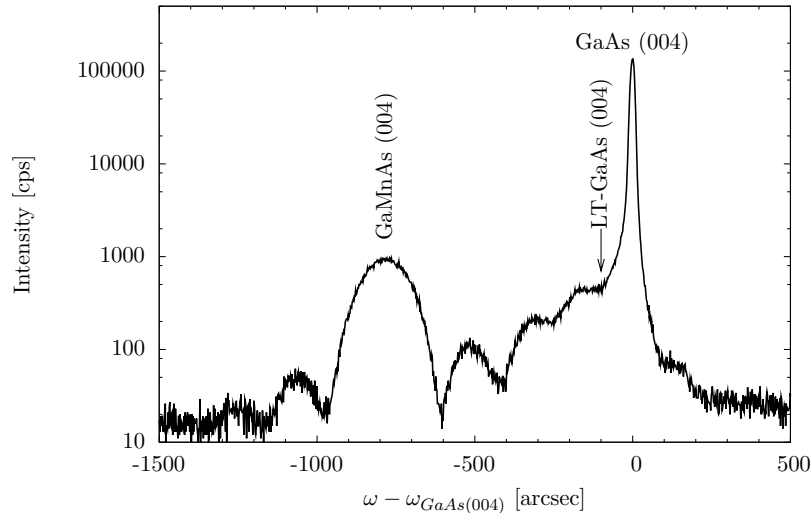
Figure 3.8: HR-XRD scan of a GaMnAs (TE546) film on GaAs.

A series of five full 2-inch wafers were grown with nominally identical film thickness (100 nm), but varying Ga and Mn fluxes to obtain a wide range of compositions. The wafers were then mounted in a high-resolution X-ray diffractometer and ω-2Θ-scans were performed at regularly spaced intervals (4 mm) across the wafer. One such scan is shown in Fig. 3.8. Clearly resolved thickness fringes enable the accurate determination of film thickness, while the separation of GaAs and GaMnAs peaks can be used to infer the lattice constant. The scans were fit to a 2-layer model accounting for the LT-GaAs and the $Ga_{1-x}Mn_xAs$ layers with the commercial Bede RADS Mercury software.

Figure 3.9 shows the film thickness and composition obtained from these fits. The thickness, which is uniform to better than $\approx 5\%$, is dominated by the growth rate of GaAs. The apparent composition, on the other hand, depends on the relative growth rates of GaAs and MnAs, as well as defect density. In particular, the density of As_{Ga} is a function of As overpressure and growth temperature [105]. Within each sample, the composition uniformity is also better than $\approx 5\%$, leading to the conclusion that both Mn and As fluxes, as well as growth temperature show good uniformity over

(a) Thickness   (b) Composition
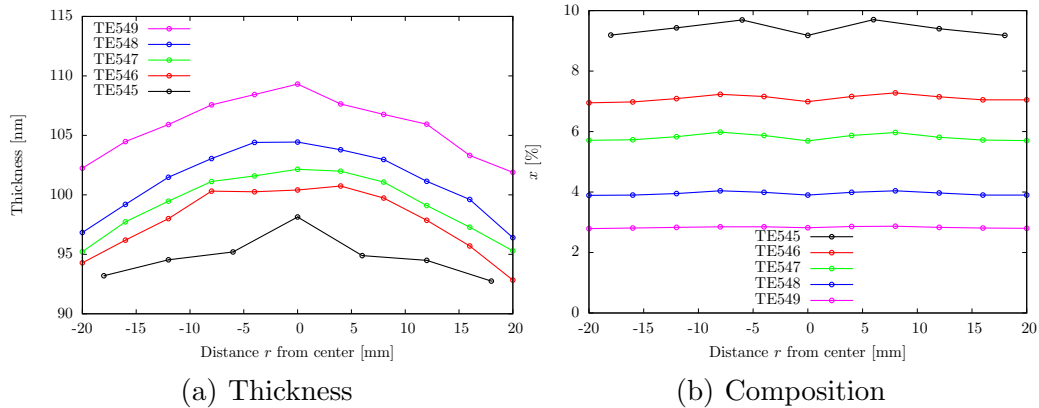
Figure 3.9: Thickness (a) and composition x (b) of five $Ga_{1-x}Mn_xAs$ samples determined by high-resolution X-ray diffraction mapping.

the entire wafer. Naturally, the flux uniformity should be equally good for the $\frac{1}{4}$ x 2" substrates used for most growth experiments, while the same may not be true for the temperature uniformity.

3.3.2   X-Ray Reflectivity

In order to accurately determine the film thickness, X-ray reflectivity was used. ω-2Θ scans were obtained with a 0.45 mm slit in front of the detector after careful alignment and z-positioning of the sample. The reflectivity curves were fitted using the software WinGixa [106] with a simple two layer model of GaAs substrate ($\rho = 5.32$ g/cm^3) and MnAs epilayer ($\rho = 6.3$ g/cm^3).

Figure 3.10 shows reflectivity scans and fits for several samples. For samples below $\approx$100 nm, thickness-fringes were well resolved. The strong dependence of the Kiessig-fringe amplitude on interface roughness affords one the possibility to gain an estimate of this parameter from the fits. Likewise, the decay of the intensity with angle provides an estimate of surface roughness. For the interface roughness, relatively small values in the range 6 to 12 Å were obtained, confirming the high

quality of the interfaces.
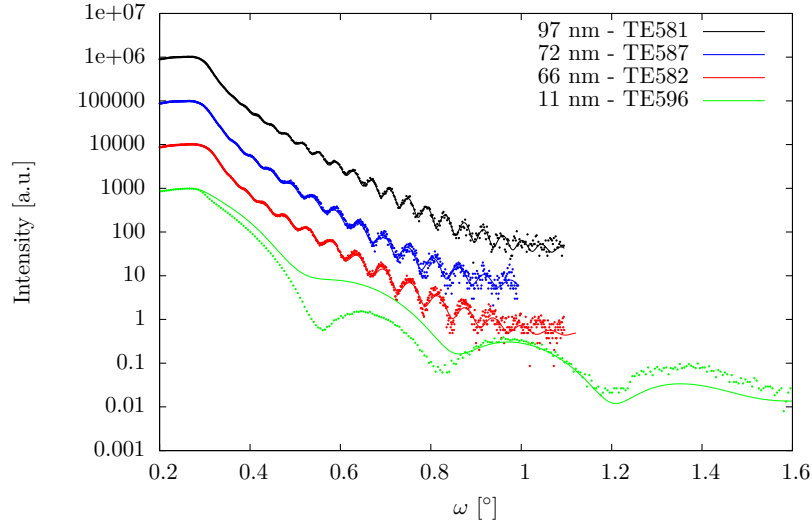
Figure 3.10: X-ray reflectivity scans for different MnAs samples. For clarity, the intensities have been normalized and offset by factors of 10. Solid lines are fits obtained for a simple two layer model.

The larger surface roughness (between 15 and 17 Å) presumably also includes the surface modulation caused by the striped phase-coexistence.

Thickness

The oscillation period in the XRR allows for accurate determination of the film thickness with a resolution on the order of 1 Å. The values obtained for two of the samples used in electrical measurements are tabulated in Table 3.1. For comparison, the thickness can also be evaluated from the electrical resistivity measurements (see 4.3). As a reference temperature, we use 340 K, where the sample is entirely in the β-phase and the temperature dependence of resistivity is very weak. Normalization was done with respect to sample TE580, where the thickness determination from XRR was most accurate.

Sample	XRR [nm]	MBE [nm]	Electrical [nm]	Buffer layer	Wafer size
TE580	68	70	68.0	HT-GaAs	$\frac{1}{4}$ x 2"
TE581	97	105	97.4	HT-GaAs	$\frac{1}{4}$ x 2"
TE600			121.7	HT+LT-GaAs	2"
TE578		140	152.6	HT-GaAs	$\frac{1}{4}$ x 2"
TE579		140	142.1	HT-GaAs, annealed	$\frac{1}{4}$ x 2"

Table 3.1: Sample thickness determined from X-ray reflectivity and electrical measurements compared to target thickness ("MBE").

The samples selected for the magnetotransport, X-ray diffraction, and reflectance difference spectroscopy measurements described in Chapters 4 and 5 are the ones listed in Table 3.1. The run numbers ("TE578" through "TE581") indicate that they were grown consecutively in this order. Aside from the growth duration, these four samples were grown on $\frac{1}{4}$ x 2" semi-insulating wafers under nominally identical conditions. After the growth, sample TE579 was annealed in-situ at a temperature of about 400°C under arsenic flux for 30 minutes. Sample TE600 was grown at a later date on a full 2" wafer, with an additional low temperature GaAs buffer layer before the start of the MnAs layer.

3.4   Atomic Force Microscopy

Atomic force microscopy provides a sensitive probe of the surface morphology. In the case of MnAs, the coexistence of α- and β-phases leads to a surface height modulation that can be conveniently probed using AFM. Here, again, we only show data from one representative sample to illustrate the important features. Scans of a number of other samples are presented in Appendix A for reference.

3.4.1   Experiment

To avoid alteration of the surface from repeated scanning, all AFM scans were obtained in non-contact mode. Here, the tip is vibrated above the surface near its natural resonance frequency using a piezoelectric transducer. A change in the atomic force thus leads to change in vibration amplitude, which is detected by the reflection of the laser beam. The difference between setpoint and detected amplitude (error signal) is fed back to the z-piezo to keep the sample-to-tip distance constant.

3.4.2   Results

In Fig. 3.11, we show a room temperature AFM scan for a very thick (≈ 355 nm) film. The α-phase appears as bright (taller) stripes separated by darker (lower) stripes of β-MnAs. A large area scan (Fig. 3.12(a)) reveals clearly the long-range correlation of the stripe pattern.
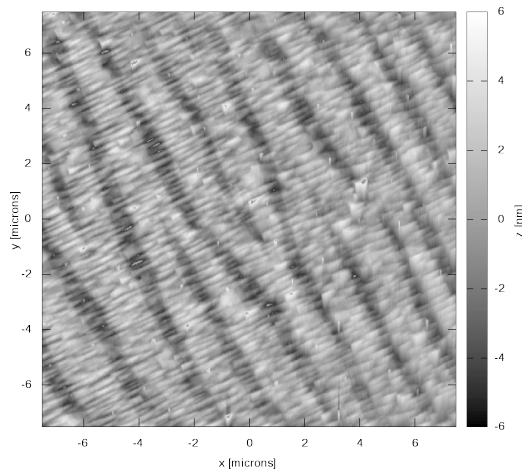
Figure 3.11: AFM scan of sample TE586 (15x15 μm^2).

The stripe period Λ can determined from the calculated 2-D power spectral density (PSD), shown in Fig. 3.12(b). For this particular sample, we find $\Lambda = 1.82$ μm,
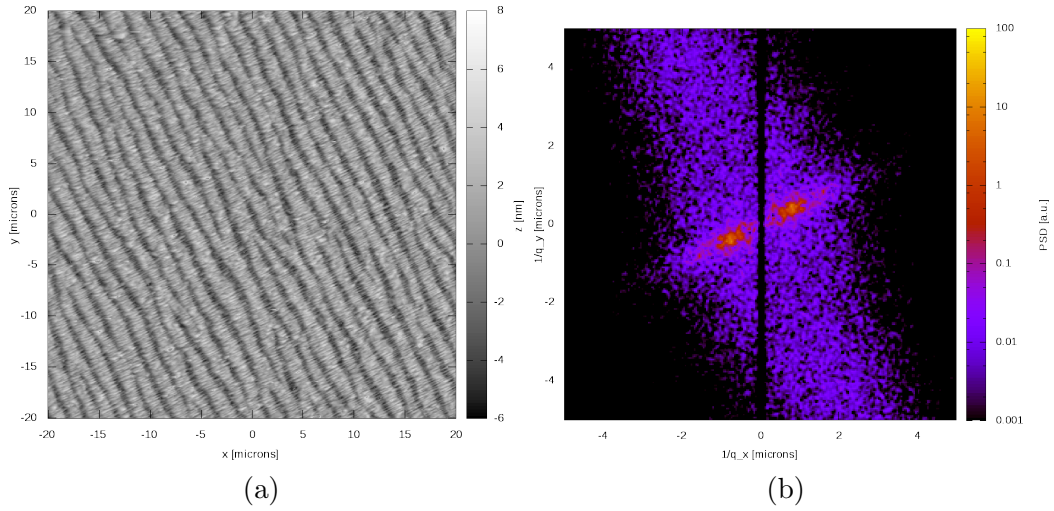
Figure 3.12: (a) Large area AFM scan of sample TE586 (40x40 μm^2) and (b) the associated 2-D power spectral density on a logarithmic scale.

in agreement with the scaling factor of 4.8 (see Section 2.2.2).

In addition to the high modulation from the two phases along [11$\bar{2}$0], a smaller ripple is also visible in the [0001] direction, see Fig. 3.13. This is caused by the large tensile strain in this direction, which cannot be relieved by the phase-coexistence. In contrast to the alternating α/β-stripes, the height modulation in the c-direction does not show a prominent periodicity as evidenced by the absence of a well defined peak in the PSD.

All of the samples selected for further study show the typical α/β-stripe pattern at room temperature.

3.5   Conclusions

With a properly adjusted As$_4$ overpressure, low initial growth rate, and substrate temperature, A$_0$ oriented MnAs films showing the characteristic striped phase coex-
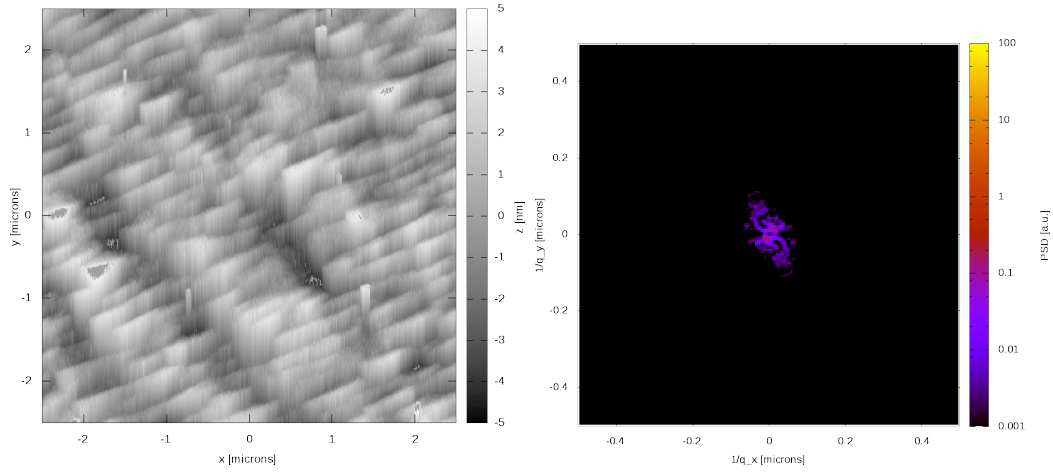
Figure 3.13: 5x5 μm^2 AFM scan of sample TE586 resolving the ripple along the MnAs c-direction and the associated 2-D power spectral density on a logarithmic scale.

istence were reproduced repeatedly on both 1/4 x 2" and full 2" wafers. There was no clear evidence for improved growth quality when a low temperature GaAs buffer layer was inserted. Increasing the growth rate after nucleation to about 50 nm/hr was found to be beneficial to film quality.

The quality of the films is evident from well-defined stripes in AFM images, the low interface and surface roughness determined from X-ray reflection, and the absence of unwanted orientations in X-ray diffraction.

Although growth procedures for MnAs have been established, considerable challenges to perfecting the growth still remain: to explore in more detail the influence of arsenic flux, the use of an arsenic cracker cell, converting As$_4$ to As$_2$ and allowing quick variation of the flux, would be important.

Substrate temperature control — a very important problem for MBE growth in general — is more difficult to address. The relatively poor control in our reactor limits comparability of different growth runs.

Chapter 4

Phase-Coexistence in the α- to β-Transition

The strain-mediated phase-coexistence of α- and β-phase in thin-films has been widely discussed in the literature. Initial studies using X-ray diffraction [69, 70] were followed by more detailed investigations of the relation between strain, phase-coexistence and magnetization (as measured by SQUID magnetometry) [95, 107, 108, 109, 110]. The peculiar arrangement of magnetic stripes has also led to a plethora of papers concerned with their micromagnetic imaging [111, 112, 113, 114] (by magnetic-force microscopy or X-ray magnetic dichroism) and modelling [115, 116, 117, 118]. Surprisingly, very little attention has been paid to magnetotransport near the phase transition — in part perhaps because of the difficulties encountered in patterning the samples (see Section 4.3.2). In this chapter, we will show that magnetotransport actually is a very useful tool to study the phase-coexistence regime, and — in complementing X-ray diffraction and atomic force microscopy — can be used to gain further insights into the hysteresis of the phase-coexistence and micromagnetic properties of the ferromagnetic stripes.

4.1 Temperature-Dependent Atomic Force Microscopy

As a result of the different lattice constants of the α- and β-phase, the phase-coexistence can be monitored by atomic force microscopy [111, 112, 119]. Aside from a series of images in J. Mohanty's dissertation [112], published temperature-dependent AFM images of the transition have either been of relatively poor quality, and/or were only recorded for very few temperatures. Hence, a detailed picture of microstructural changes during the phase transition has not emerged. An attempt was therefore made to improve on this situation, and AFM images of high quality with good temperature resolution were recorded.

4.1.1 Temperature Control

In order to controllably vary the temperature of the sample in the atomic force microscope over the relevant range, a thermoelectric element, mounted on top of a machined copper heat sink was employed. The copper heat sink is kept at a constant temperature by a small ($\approx 1\,\mathrm{l/h}$) flow of water. A key requirement for high resolution scanning probe microscopy is minimization of acoustical vibrations. Therefore, the cooling water was gravity-fed from a reservoir. A commercial temperature sensor (AD590) is mounted next to the sample directly on top the thermoelectric element, both heat sunk using silver paint. To avoid condensation on the cooled surface, the dome covering the AFM was purged with dry nitrogen gas during the entire measurement.

Photographs of the setup are shown in Fig. 4.1.
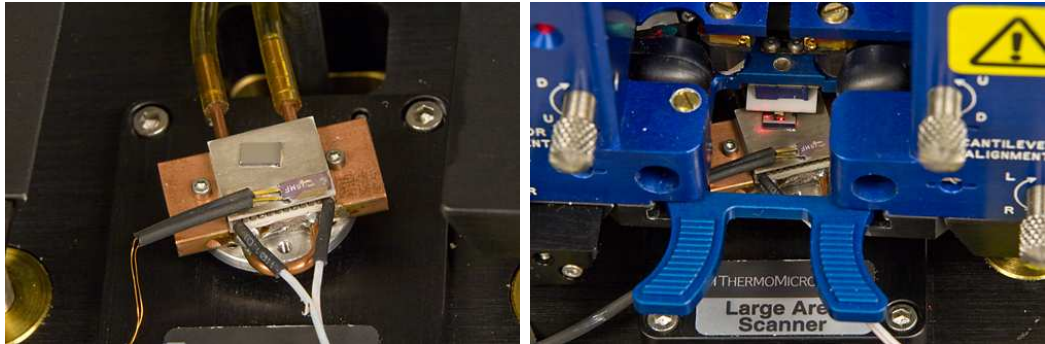
Figure 4.1: Setup for temperature-dependent AFM.

4.1.2 Results

Due to the time consuming experimental effort involved, temperature-dependent AFM measurements were only performed for two samples. Sample TE568 was the first MnAs sample grown in our reactor that shows the typical stripe pattern. The sample is about 260 nm thick. Sample TE574 has a thickness of about 132 nm and is thus more representative of the samples used in other experiments. AFM scans for this sample were recorded in steps of 1 to 2 K, first upon cooling from 326 K to 270 K and then upon heating back to 326 K. The raw images were processed as described in Section 3.4.1. In addition, the thermal and temporal drifts encountered between scans were compensated for by shifting the images. The required shift was computed from the center of mass of the cross-correlation with a reference image. The overall shifts are small and only reduce the field of view from 512x512 to 492x492 pixels.

In Fig. 4.2, we show a selection of the AFM images obtained upon cooling for sample TE568. These images give a very detailed picture of the temperature evolution of the two phases. The nucleation of α-phase stripes is observed just below 315 K. Initially, these short stripes are seemingly randomly distributed. In the temperature range between 312 K and 306 K, they grow rapidly in length, and reorganize so as to be separated by some amount of β-phase to fulfill the lattice constraints on

average. As temperature is further lowered, the stripes become wider, and in some cases connect with other stripes. Gradually, increasing order emerges in the array of stripes.

To better visualize the temperature dependence, vertical cross section profiles were calculated for each temperature by averaging over a 0.78 μm wide horizontal region. Figure 4.3 shows the evolution of this cross section over the phase-coexistence range. Upon cooling, the beginning nucleation of α-phase stripes is clearly discernible between 315 and 310 K. As temperature is lowered further, the width of α-stripes increases and the β-phase decreases. The coalescence of two α-stripes is observed between 290 and 285 K at $y = 2.5$ μm. The transition is not complete until below 280 K. For lower temperatures, peculiar ridges develop in the same places where the β-MnAs troughs were located. Upon heating, strong thermal hysteresis is observed and the typical stripe pattern does not develop until above 305 K. The ridge-like features, however, are not affected by the phase transition and can still be observed for temperature above 320 K. The morphology of the sample has thus been altered in an irreversible way.
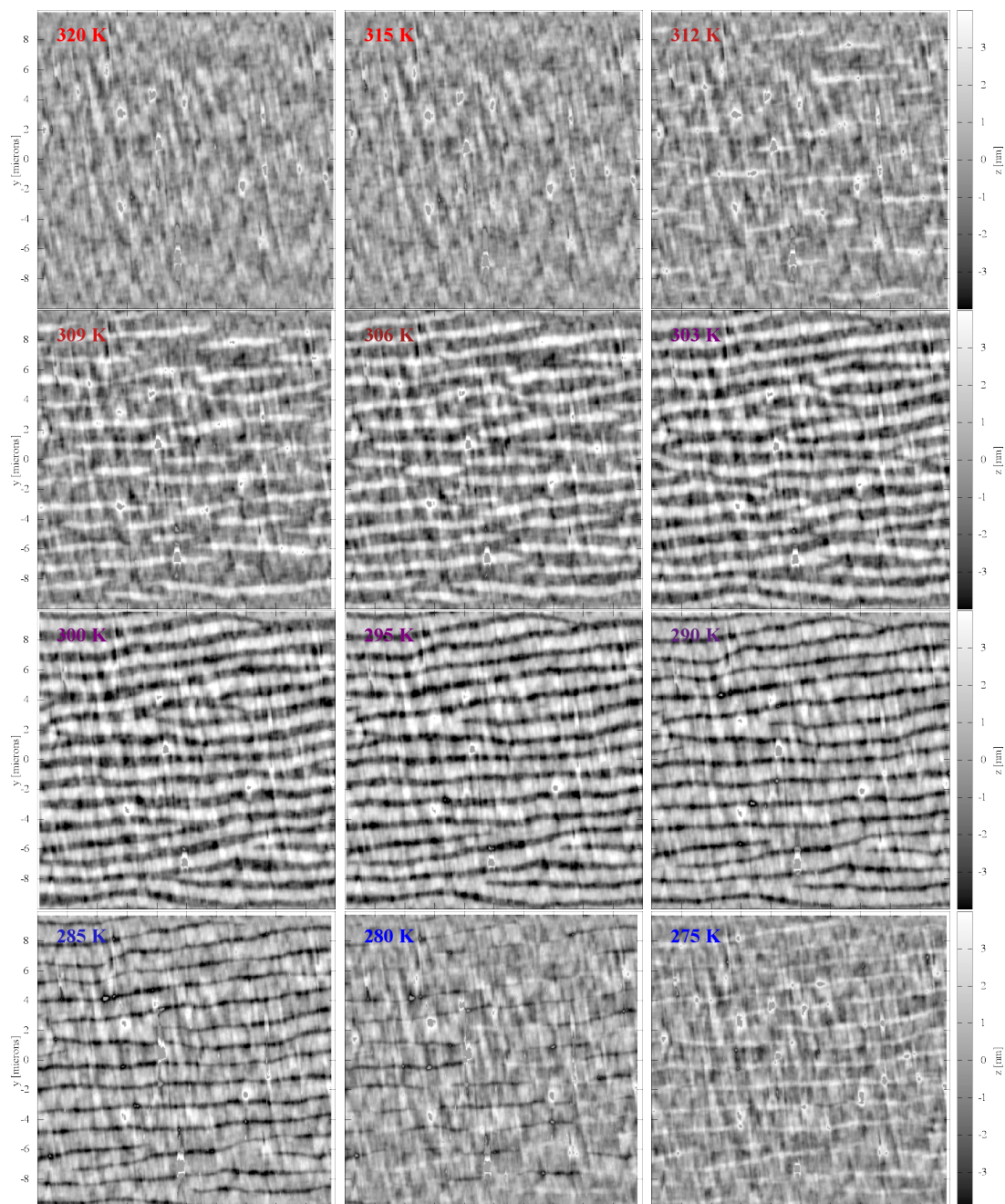
Figure 4.2: Temperature-dependent AFM scans (20 μm x 20 μm) for TE568 during cooling from 330 K to 270 K.
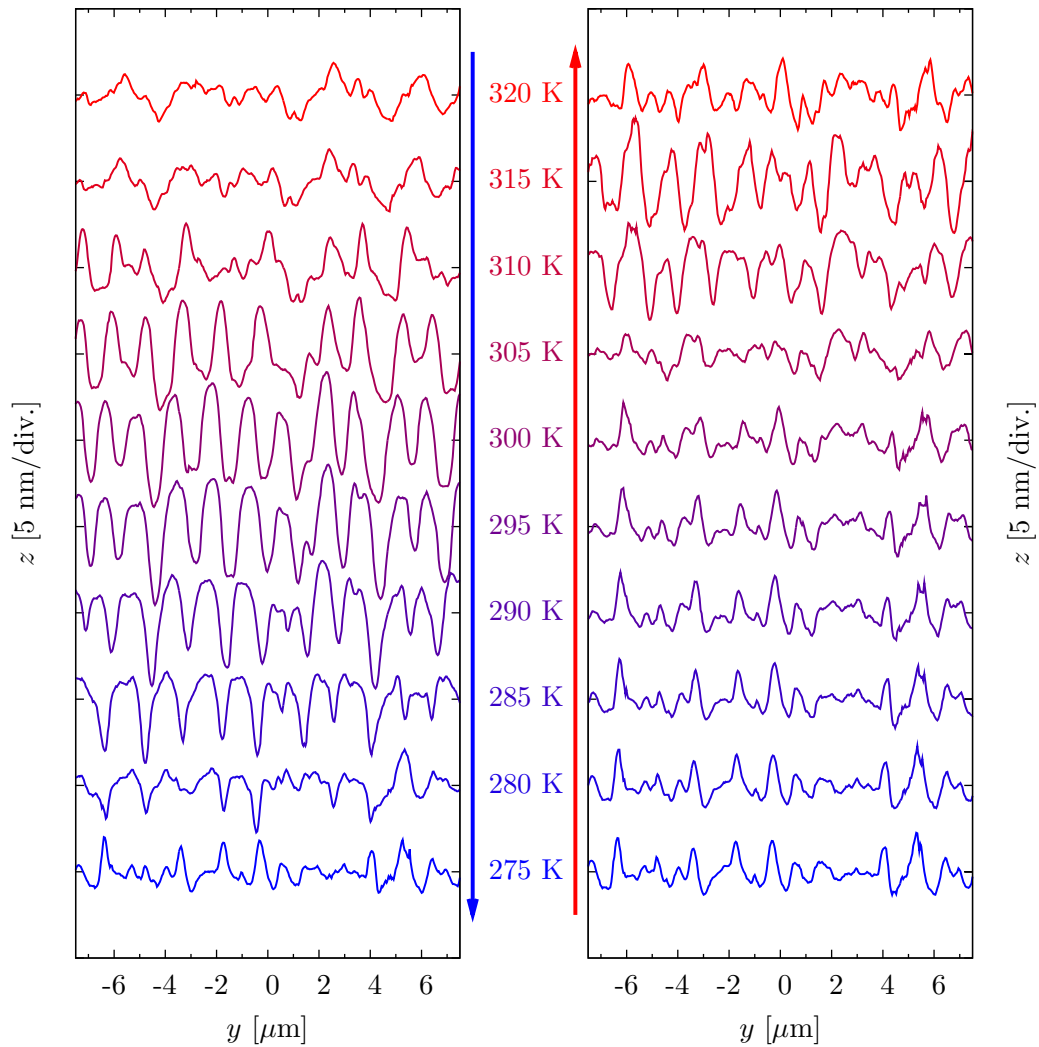
Figure 4.3: AFM profile versus temperature for TE568. Cooling is shown to the left, heating on the right.

Movies

A better impression of the process of the phase transition can be gained from a movie that has been compiled from the single AFM images. The following AFM movies are available for viewing:

TE568

- $(20 \ \mu\text{m})^2$ scan area (Fig. 4.4)

- Power spectral density (http://www.chtm.unm.edu/education/dissertations/ jaeckel/TE568_PSD.mpg)

TE574

- $(7.5 \ \mu\text{m})^2$ scan area (Fig. 4.5)

- Power spectral density (http://www.chtm.unm.edu/education/dissertations/ jaeckel/TE574_PSD.mpg)
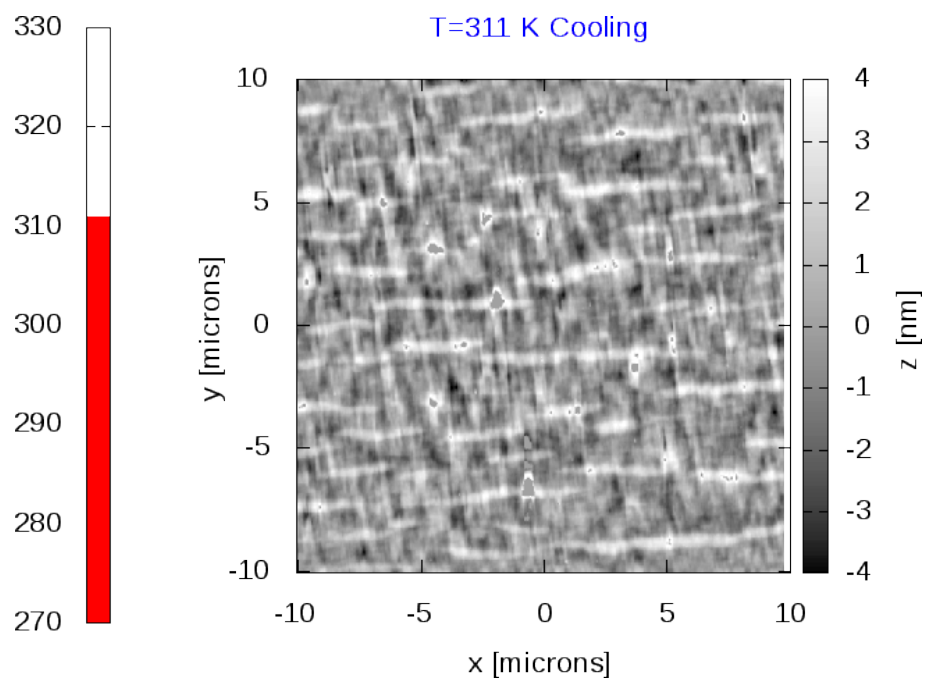
Figure 4.4: Temperature-dependent AFM movie of TE568, also available online at http://www.chtm.unm.edu/education/dissertations/jaeckel/TE568_AFM.mpg.
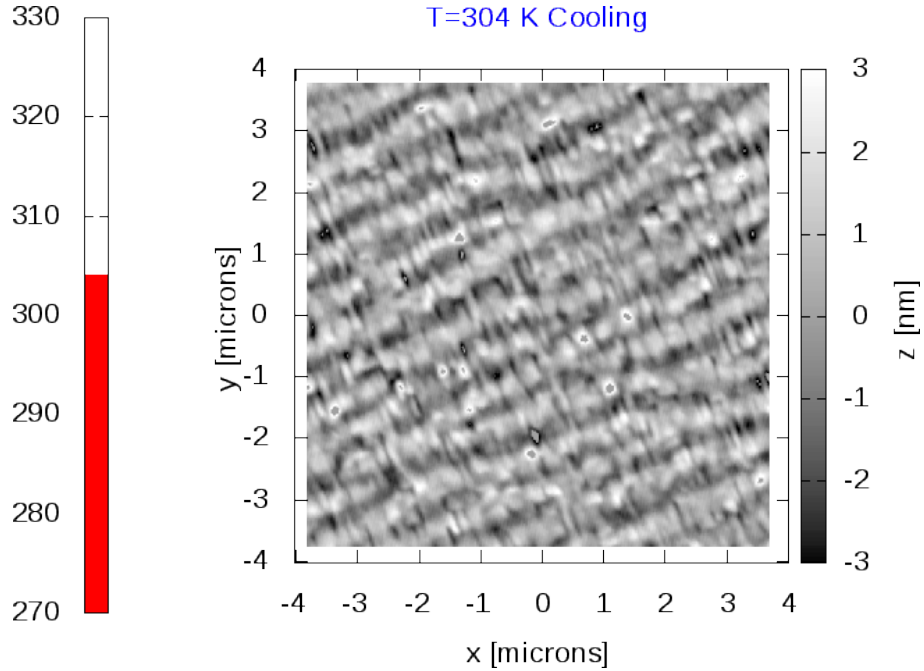
Figure 4.5: Temperature-dependent AFM movie of TE574, also available online at http://www.chtm.unm.edu/education/dissertations/jaeckel/TE574_AFM.mpg.

4.2 X-Ray Diffraction

The phase coexistence regime of the α- to β-transition can be monitored by X-ray diffraction. Since the out-of-plane lattice constant of the α-phase is slightly larger than that of the β-phase, two separate sets of reflections are distinguishable in a symmetric $\omega - 2\Theta$ geometry. The relatively weak structure factors of the α-MnAs ($1\bar{1}00$) and β-MnAs (020) reflections have apparently prevented researchers from monitoring the phase transition with good temperature resolution (typically 5 K steps with one or two 2.5 K steps in the middle of the phase-coexistence region). While sufficient to notice the hysteresis in the phase-fraction [70], this temperature resolution is clearly insufficient to resolve the structure in the hysteresis we will discuss in the following.

4.2.1 Setup

In order to obtain diffraction profiles with good counting statistics and sufficient temperature resolution with reasonable measurement times, the use of a powder diffractometer with a fast parallel detector was necessary. The Panalytical X'Pert Pro diffractometer at Sandia National Lab's Advanced Materials Laboratory, equipped with an "XCelerator Realtime Multistripe" (RTMS) detector proved to be ideal for this purpose. Unlike a high-resolution X-ray diffractometer, this powder diffractometer provides non-monochromatic copper radiation. However, a large fraction of the unwanted Cu K_β ($\lambda_\beta = 1.3926$ Å) peak and the Bremsstrahlung background can be eliminated by insertion of a nickel filter (absorption edge 1.4886 Å) into the beam path. Beam divergence and geometry can be controlled by means of programmable divergence and anti-scatter slits, as well as a beam mask. Incident beam energy for all experiments was 45 keV at 40 mA.

Temperature Control

Temperature control was achieved by mounting the sample on top of a copper heatsink using silver paint. The temperature of the heat sink was controlled by a Peltier cooler, an AD590 integrated circuit temperature sensor, and an ILX LDT-5910B temperature controller.

To prevent strong temperature gradients due to air currents, the entire assembly was shielded with a PVC pipe, while an X-ray transparent window was provided with Kapton tape. An optional provision for nitrogen purging was not used as nitrogen was not readily available in the lab and low humidity made it unnecessary. The sample stage, including cover, is shown in Fig. 4.6.
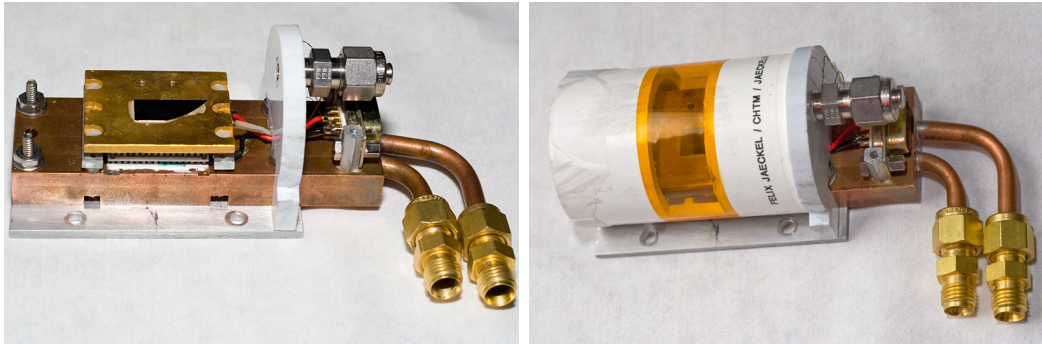
Figure 4.6: Setup for temperature-dependent X-ray diffraction.

K$_{\alpha2}$ Elimination

One obstacle in the analysis of X-ray data is the presence of both Cu K$_{\alpha1}$ and K$_{\alpha2}$ radiation. For narrow peaks, like GaAs (002), this leads to double peak structures. Closely spaced peaks like α-MnAs (1$\bar{1}$00) and β-MnAs (020) show shoulders on the high angle side, making clean peak separation impossible. The integrated intensity of the K$_{\alpha2}$ peak is approximately half that of K$_{\alpha1}$.

Using an analytical representation of the lineshapes of both peaks (see Fig. 4.7), Dong et al. [121] have developed an algorithm to remove the K$_{\alpha2}$ contribution using a "weights" and "levers" approach. Figure 4.8 shows a comparison of a raw spectrum with the one obtained from applying this algorithm. Clearly, the algorithm is successful in stripping the K$_{\alpha2}$ component, and only a weak distortion to the right of the GaAs remains.

Fitting

After Cu K$_{\alpha2}$ elimination, the areas of the two peaks need to be determined separately. Due to the partial overlap of the peaks, fitting with a predefined lineshape is necessary. In X-ray line fitting, the use of Lorentzian and Gaussian lineshapes is cus-
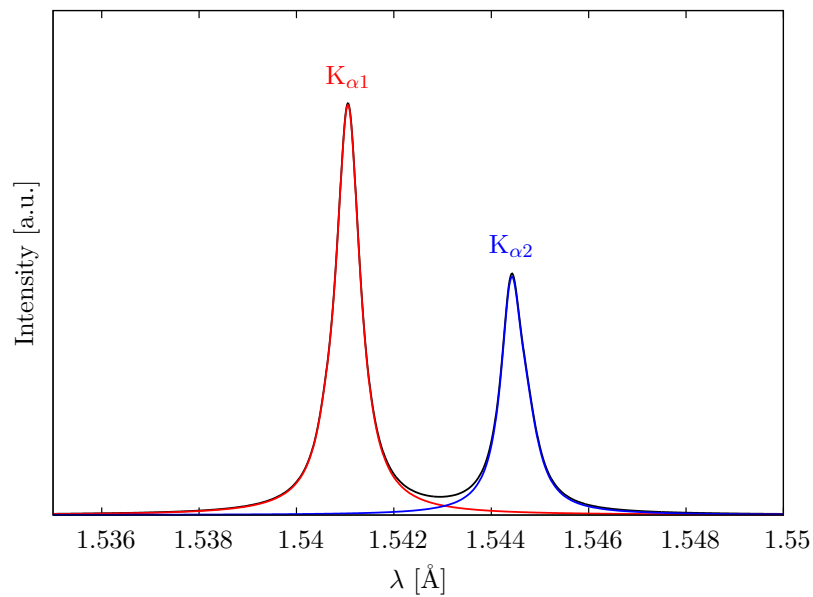
Figure 4.7: Analytical representation of the copper K_α lines, using parameters from Cheary and Coelho [120].
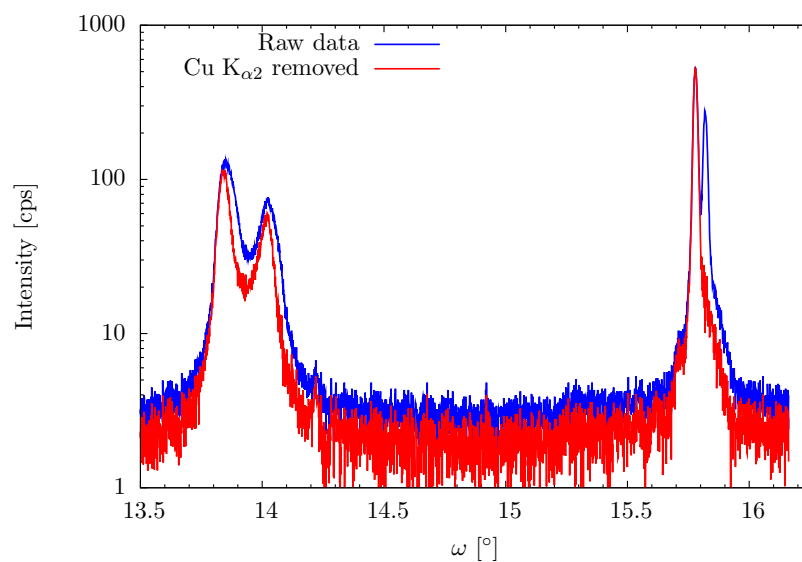
Figure 4.8: Comparison of raw X-ray diffraction spectrum (blue) with a spectrum where the contribution from the Cu $K_{\alpha2}$ line has been numerically stripped (red).

tomary [122]. To obtain satisfactory fits, it is often necessary to use the convolution of Gaussian and Lorentzian lineshapes, known as Voigt profile:

$$V(\omega) = \int_{-\infty}^{+\infty} G(\omega')L(\omega - \omega')d\omega', \tag{4.1}$$

with the Lorentzian

$$L(\omega) = \frac{A}{\pi} \frac{\frac{\gamma_L}{2}}{(\omega - \mu)^2 + \left(\frac{\gamma_L}{2}\right)^2} \tag{4.2}$$

defined by its area A, center position μ, and full-width half-maximum (FWHM) γ_L. For the Gaussian

$$G(\omega) = \frac{1}{\sigma\sqrt{2\pi}} e^{-\omega^2/2\sigma^2}, \tag{4.3}$$

the FWHM is given by $\gamma_G = 2\sigma\sqrt{2\ln 2}$.

The α-phase-fraction f_α is determined from the integrated areas A of the Voigt fits as

$$f_\alpha = \frac{A_{\alpha(1\bar{1}00)}}{A_{\alpha(1\bar{1}00)} + A_{\beta(020)}}. \tag{4.4}$$

4.2.2 Results

Temperature was ramped at a rate of 1 K/min, decreasing from 323 K to 273 K and back to 323 K in steps of 1 K. At each temperature step $\omega - 2\Theta$ scans including both MnAs and for reference the GaAs (002) reflection were recorded. The Voigt lineshape, in the approximation given by McLean et al. [123], was automatically fit to the Bragg peaks of α-MnAs ($1\bar{1}00$) and β-MnAs (020) using the Levenberg-Marquardt algorithm implemented in the GNU Scientific Library [124]. For improved numerical stability of the fitting results, the FWHM parameters γ_L and γ_G were determined for each sample in the single phase state and then kept fixed for intermediate temperatures. Identical FWHM values were obtained for pure α- and β-phases.

In Fig. 4.9 we show the evolution of the diffraction scans versus temperature for one representative sample, along with the fits.
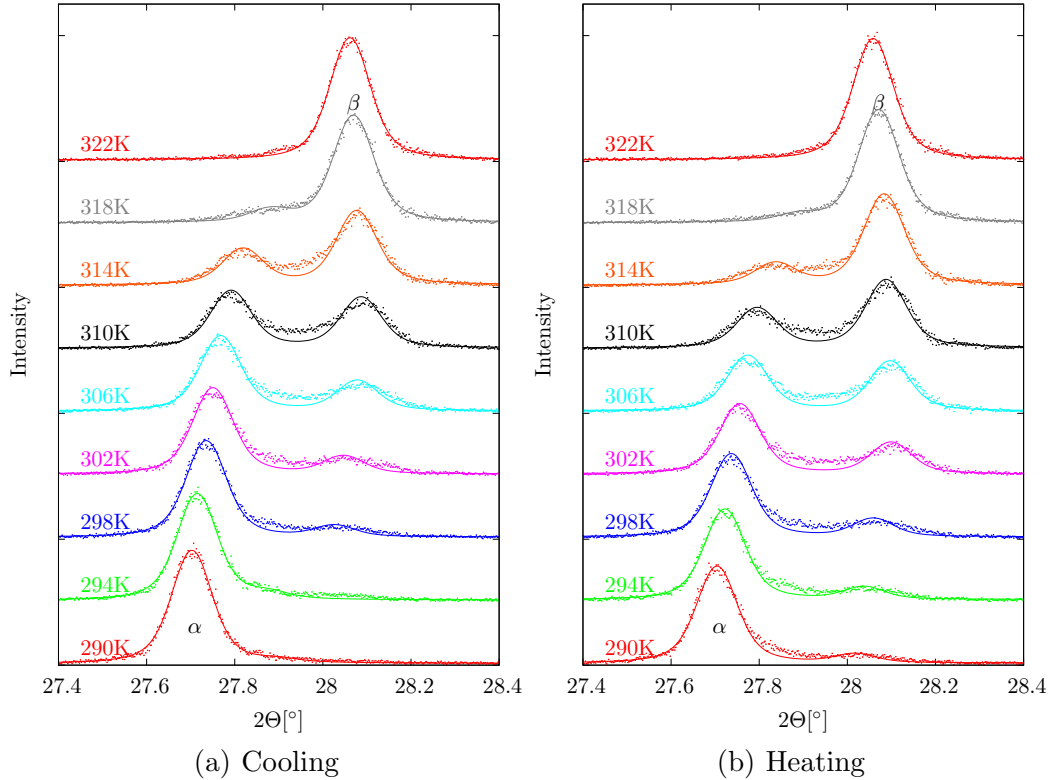
Figure 4.9: X-ray diffraction scans obtained for sample TE580 upon (a) cooling from 330 K and (b) upon heating from 276 K. Voigt profile fits are shown as solid lines.

A plot of the α-phase-fraction versus temperature is shown in Fig. 4.10. The phase-coexistence extends from ≈ 282 to 318 K, a range of about 36 K. Evidently, there is a considerable hysteresis between cooling and heating cycles.

Finally, in Fig. 4.11 we show the lattice constants of the α- and β-phases as a function of temperature. The lattice constants of the α-phase at high temperatures, as well as the β-phase at low temperatures, should be treated with caution, since the low phase-fractions increase the uncertainty in the fits. The trends and absolute values agree with data published by Adriano et al. [68], measured at a synchrotron.
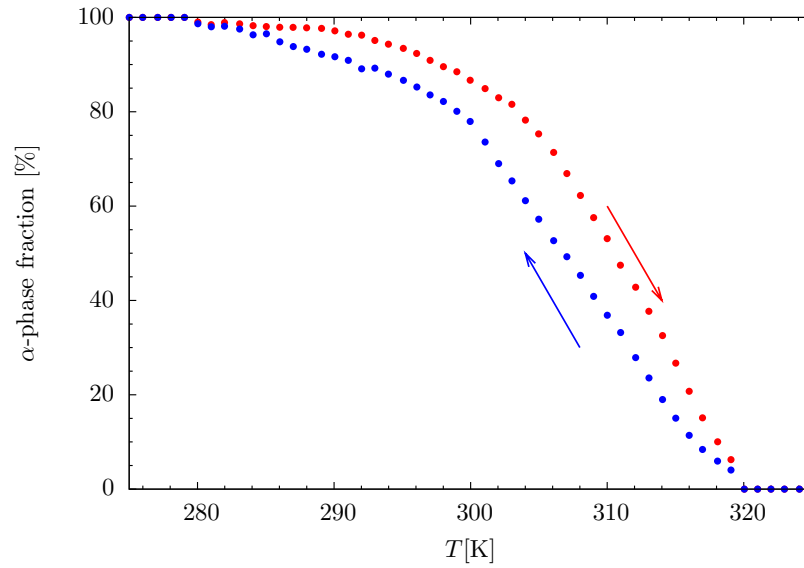
Figure 4.10: α-phase-fraction versus temperature from X-ray diffraction measurements for heating (red) and cooling (blue) cycles.
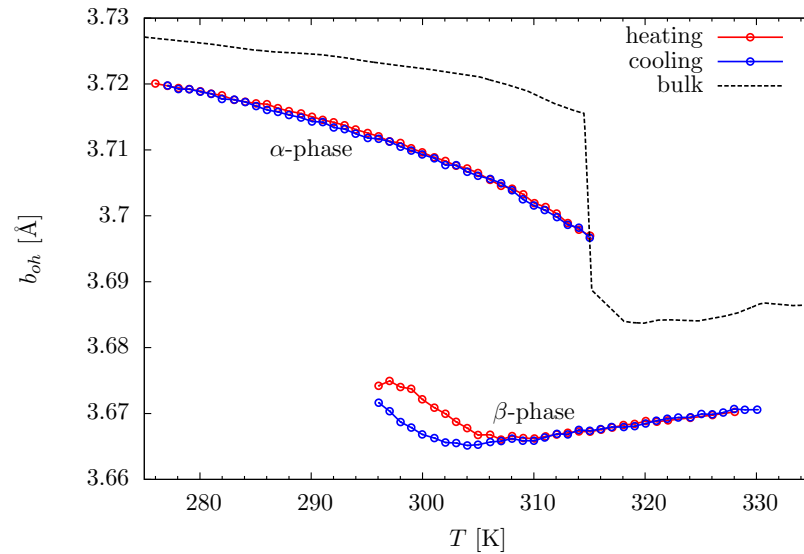
Figure 4.11: Out-of-plane lattice constant of α- and β-phase during the phase transitions as a function of temperature. For comparison, the bulk lattice constant after Suzuki et al. [31] is also shown.

4.3 Magnetotransport

Having established a way to follow the evolution of α- and β-phase across the transition, we now turn our attention towards the magnetotransport properties of these films. Previous studies have suffered from a lack of understanding of the phase-coexistence [125], experimental problems arising from difficulties in etching MnAs [126], have ignored the Hall effect [117, 127], or were entirely focused on low temperature effects [94, 128, 129, 130].

In the following, our choice of coordinate system is dictated by the usual convention of labeling the in-plane components of the conductivity tensor as $\sigma_{xx,xy,yx,yy}$. The x-axis is along $[11\bar{2}0]$ (perpendicular to stripes), the y-axis along $[0001]$ (parallel to the stripes), and the z-axis along $[1\bar{1}00]$, i.e. in the growth direction.

If a magnetic field is applied in the z-direction, the conductivity tensors σ^i ($i = \alpha, \beta$) for α- and β-phase are of the form

$$
\sigma^i = \begin{pmatrix} \sigma^i_{xx} & \sigma^i_{xy} & 0 \\ \sigma^i_{yx} & \sigma^i_{yy} & 0 \\ 0 & 0 & \sigma^i_{zz} \end{pmatrix}.
\tag{4.5}
$$

The off-diagonal elements σ_{xy} and σ_{yx} are due to the Hall effect. For non-magnetic materials, Onsager's reciprocity relations would require $\sigma_{yx} = -\sigma_{xy}$, but we are not forced to follow this assumption. Because of the hexagonal symmetry of the α-phase we find the additional constraint $\sigma^\alpha_{zz} = \sigma^\alpha_{xx}$.

4.3.1 Magnetotransport in a Composite

In the phase-coexistence regime, magnetotransport in the thin-films naturally has to be evaluated in the light of a "composite medium" analysis. In recent years, a lot

of progress has been made towards finding expressions for the effective conductivity tensor σ^e of composite media, see for example Milton [131]. For a system with a parallel slab geometry, relatively simple exact expression have been derived [132]. For the x-axis perpendicular to the slabs with conductivity tensor σ^i and relative phase fractions f_i ($\sum_i f_i = 1$):

$$\frac{1}{\sigma_{xx}^e} = \sum_i \frac{f_i}{\sigma_{xx}^i}, \tag{4.6}$$

$$\sigma_{xa}^e = \sigma_{xx}^e \sum_i f_i \frac{\sigma_{xa}^i}{\sigma_{xx}^i}, \qquad \sigma_{ax}^e = \sigma_{xx}^e \sum_i f_i \frac{\sigma_{ax}^i}{\sigma_{xx}^i} \tag{4.7}$$

for $a = y, z$, and finally

$$\sigma_{ab}^e = \sum_i f_i \sigma_{ab}^i + \sum_i f_i \sigma_{ax}^i \frac{\sigma_{xb}^e - \sigma_{xb}^i}{\sigma_{xx}^i} \tag{4.8}$$

for $a = y, z$ and $b = y, z$. These expressions are valid even for non-symmetric and complex-valued conductivity tensors.

From 4.7 it immediately follows that the effective conductivity tensor of parallel slabs of α- and β-MnAs is of the same form as the one for each phase:

$$\sigma^e = \begin{pmatrix} \sigma_{xx}^e & \sigma_{xy}^e & 0 \\ \sigma_{yx}^e & \sigma_{yy}^e & 0 \\ 0 & 0 & \sigma_{zz}^e \end{pmatrix}. \tag{4.9}$$

Of course, for a thin-film only the in-plane elements of the conductivity tensor are easily accessible and therefore the task at hand is to determine σ_{xx}, σ_{yy} as well as the off-diagonal elements σ_{xy} and σ_{yx}.

For this purpose, a mask was designed with two Hall-bar devices connected in series, allowing us to apply currents $j_x = j_y$ along the two in-plane crystallographic

axes. Using voltage probes on the side of the devices, the electric field components E_x and E_y can thus be determined. From this measurement, the elements of the resistivity tensor are found as

$$\rho_{xx} = \frac{E_x}{j_x} \qquad\qquad \rho_{xy} = \frac{E_y}{j_x} \qquad\qquad (4.10)$$

from the Hall-bar device oriented along x and

$$\rho_{yy} = \frac{E_y}{j_y} \qquad\qquad \rho_{yx} = \frac{E_x}{j_y} \qquad\qquad (4.11)$$

from the other Hall-bar device oriented along y.

The conductivity tensor is obtained as the inverse of the resistivity tensor

$$\sigma = \rho^{-1} = \begin{pmatrix} \sigma_{xx} & \sigma_{xy} & 0 \\ \sigma_{yx} & \sigma_{yy} & 0 \\ 0 & 0 & \sigma_{zz} \end{pmatrix} = \begin{pmatrix} \frac{\rho_{yy}}{\rho_{xx}\rho_{yy}-\rho_{xy}\rho_{yx}} & \frac{\rho_{xy}}{\rho_{xy}\rho_{yx}-\rho_{xx}\rho_{yy}} & 0 \\ \frac{\rho_{yx}}{\rho_{xy}\rho_{yx}-\rho_{xx}\rho_{yy}} & \frac{\rho_{xx}}{\rho_{xx}\rho_{yy}-\rho_{xy}\rho_{yx}} & 0 \\ 0 & 0 & \frac{1}{\rho_{zz}} \end{pmatrix}. \quad (4.12)$$

In practice, both ρ_{xy} & ρ_{yx} are much smaller than ρ_{xx} & ρ_{yy} (in our case by a factor of 100 to 1000), and the above can be simplified to

$$\sigma \approx \begin{pmatrix} \frac{1}{\rho_{xx}} & -\frac{\rho_{xy}}{\rho_{xx}\rho_{yy}} & 0 \\ -\frac{\rho_{yx}}{\rho_{xx}\rho_{yy}} & \frac{1}{\rho_{yy}} & 0 \\ 0 & 0 & \frac{1}{\rho_{zz}} \end{pmatrix}. \qquad\qquad (4.13)$$

One interesting application of the closed form expressions of the composite conductivity tensor (equations 4.6, 4.7 and 4.8) is the possibility to determine the relative phase fractions of a two component system if the the conductivities of the two components are known. We follow this idea in Section 4.3.3 to accurately determine the relative fractions of α- and β-phase.

4.3.2 Experimental Setup

Sample Geometry and Patterning

Due to the anisotropic conductivity of MnAs, the Hall-bar geometry with its well defined current path is preferable over a van-der-Pauw arrangement. Precise lithographic patterning ensures a well defined geometry and reduces contact misalignment voltages. In order to simultaneously measure resistivities in the two in-plane crystalline directions, a double Hall-bar geometry was chosen, see Fig. 4.12. The geometrical design follows the usual rules [133] for obtaining minimal deviations from the ideal case.
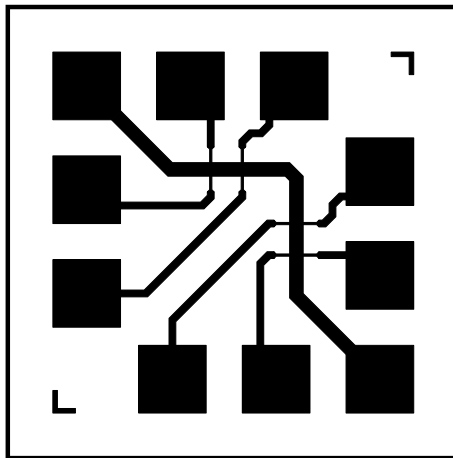
Figure 4.12: Mask layout of the double Hall-bar geometry. The Hall-bars are 300 μm wide, with a contact separation of 700 μm. The size of the contact pads is (1.5 mm)^2.

Patterning of MnAs has been perceived as a challenging problem. MnAs can be wet-etched in solutions of hydrochloric or phosphoric acid, similar to GaAs [134]. Unfortunately, the unequal etch rates of α- and β-phases and the resulting strain lead to cracks in the film [135], unless the sample is heated into a single phase state [126]. It also is slightly attacked by diluted KOH (as used in AZ400K developer) and we have observed permanent alterations of the surface from water condensing on the

surface. Organic solvents like acetone, methanol, or isopropanol, on the other hand, do not seem to have an effect on the surface (see also Mohanty et al. [135]).

It has also been claimed that MnAs cannot be easily processed by dry-etching: For a Cl_2 based reactive ion etch, very small etch rates of 3.5 nm/min have been reported [136]. Therefore, complicated processing schemes involving metal etch masks and subsequent argon ion milling have been proposed. In these cases, the metal etch mask had to be removed from the sample, which was accomplished by either incorporating a PMMA release layer [126] or etching of the titanium mask with hydrofluoric acid [136], again at elevated temperatures. Neither process is satisfactory, as alteration or damage of the MnAs layer seems likely.

In order to reliably pattern the films without any chance of chemical or physical damage, the goal has to be avoidance of contact of the final device with chemicals (including water) other than solvents. Therefore, we chose to pursue the dry etching technique without any intermediate masking layers.

The sample surface was protected with the organic photoresist AZ4330 [137] which can be stripped with acetone. After solvent cleaning of the sample, the photoresist was spun on without adhesion promoter to a thickness of ≈ 3.3 μm and baked at 90°C for 2 minutes.

In initial rounds of processing, for some of the thicker samples high resistances were observed for the voltage probes. At the same time, these samples showed linear trenches in the etched GaAs substrate.

Nomarski and scanning electron microscopy (Fig. 4.13) revealed narrow cracks in the MnAs films running perpendicular to the stripe direction. Cracks that were present before the etch are transferred into the substrate, where deep trenches are formed due to the higher etch rate of GaAs compared to MnAs. Additional cracks are formed after the etch and are confined to the MnAs layer. Cracks are formed

(a) Nomarski

(b) SEM
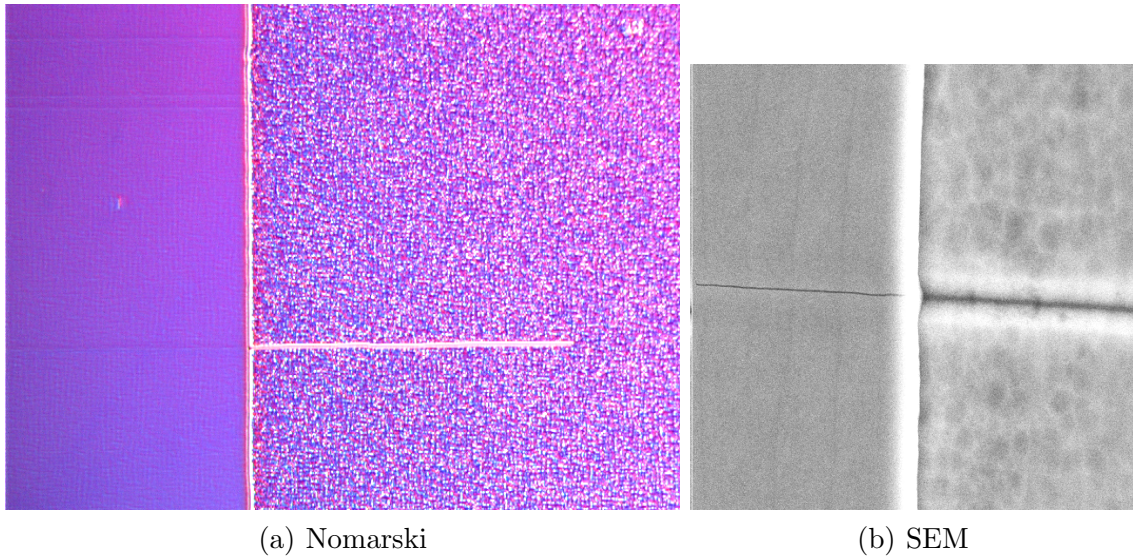
Figure 4.13: Nomarski micrograph (a) and SEM image (b) of cracks observed in a processed MnAs Hall-bar sample. The vertically oriented stripes on the mesa (left) are due to the height modulation of the α/β phase-coexistence. Perpendicular to these stripes, faint cracks are visible. A trench in the GaAs substrates (right) forms the extension of this crack.

when the thermal expansion mismatch strain exceeds a certain value. While the strain along $[11\bar{2}0]$ can be relieved through the phase-coexistence of α- and β-phase, no such relief mechanism exists for the [0001]-direction, leading to the formation of cracks orthogonal to this direction, i.e. perpendicular to the stripes. It was found that the formation of cracks can be avoided by reducing thermal shock during processing. Later, samples were placed on a block of metal for slow heating and cooling. The cracking of much thicker films (0.6 to 3 μm) was recently investigated in more detail by Takagaki [138]. Unlike the straight cracks formed due to rapid thermal cycling, these cracks were found to consist of chains of short inclined segments (angle $\approx 57°$).

After UV exposure, samples were developed in a solution of 1 part AZ400K [137] diluted with 4 parts of deionized water. The water-rinsed and dried samples were then etched in an inductively coupled plasma (ICP) etcher, using the "Zia InP"

recipe (BCl$_3$ flow 35 sccm/min, 500 W ICP power, 90 W RIE power).

Contrary to the very low etch rates [139] reported in the literature for reactive ion etching (RIE) with Cl$_2$ and Ar, we found substantial etch rates in our BCl$_3$ based ICP etch. The etch progress was monitored using a laser reflectivity setup [140]. A few typical curves for reflectivity versus etch time for samples of different thickness are shown in Fig. 4.14. During the etch of the MnAs layer, the reflectance stays fairly constant. As the MnAs layer is locally penetrated the reflectance drops due to surface roughening from the much faster etch rate of GaAs. Once all of the MnAs is removed, the GaAs etch front becomes smooth again and reflectance increases. Etch rates obtained were around 30 nm/min for MnAs, compared to 300 nm/min for GaAs.
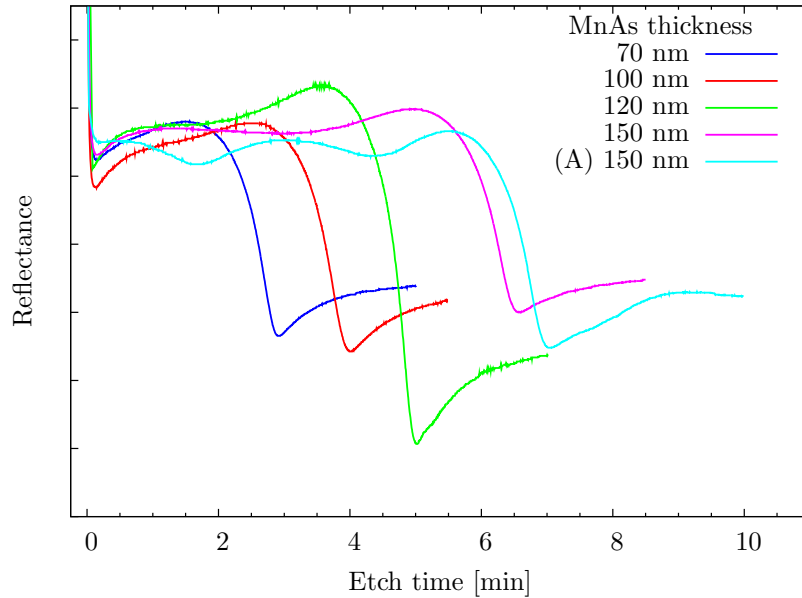
Figure 4.14: Reflectivity measured during the ICP etch of various MnAs samples using a 670 nm laser diode.

After etching, isolation was confirmed by a resistivity measurement, with the probes of a multimeter placed on the etched surface. As the last step, photoresist was removed with acetone, methanol and isopropanol, and the etch step-height recorded

using a profilometer.

This relatively simple processing sequence is in stark contrast to the elaborate process reported by Takagaki [126], where a 4-layer stack of PMMA, negative photoresist, titanium etch mask, and again negative photoresist were employed to finally argon ion-mill the sample and remove the resist stack by releasing the PMMA with a solvent.

Dewar

To measure magnetotransport over a wide temperature range, the samples were mounted inside a MMR-Technologies Hall dewar with a Joule-Thompson refrigerator. The cold stage allows access to temperatures from 78 K to over 700 K. The dewar itself was evacuated with a turbo pump to a pressure of about $2 \cdot 10^{-5}$ mbar.

Temperature Control

Precise temperature measurement and regulation was accomplished through a Pt-100 resistance thermometer and an electrical heating pad, both situated at the end of the cold-finger underneath the sample. For cooling below 300 K ultrahigh-purity nitrogen at a pressure of 500 to 1800 psi was expanded to atmosphere through the Joule-Thompson cold-finger. Using the CryoCon 32B temperature controller with proportional-integral (PI) control, temperature stability at the milli-Kelvin level was achieved over the entire temperature range. The influence of the static magnetic field and induced voltages from transients was noticeable, but smaller than 50 mK.

Magnetic Field

The magnetic field was produced by an electromagnet driven by a constant current source. For the measurements presented here, the pole gap was adjusted to 33 mm, allowing magnetic fields of up to $\mu_0 H = 0.9$ T to be reached. Field reversal was achieved through a pair of SPDT relays, properly interlocked with the power supply for safety reasons. The magnetic field was measured in close proximity to the sample with a Hall probe (BH-200) thermally anchored to the vacuum chamber.

Sample Mounting and Wiring

The samples were mounted on the MMR temperature stage using a small amount of silver paint [141] for excellent thermal contact. Low thermal conductivity phosphor bronze wires were glued to the contact pads also with silver paint, Fig. 4.15.

When only a single Hall-bar was measured, the common ground was connected to that Hall-bar to ensure minimal common-mode voltages. For the same reason, the Hall signal was recorded from the two terminals closest to ground. The sample was wired to minimize induced voltages on the Hall voltage lines by keeping the enclosed loop area as small as possible.

AC Hall Measurement

A Keithley 6221 precision AC/DC current source was used to supply current through the sample at a frequency of 38.347 Hz[1]. All voltage signals were buffered by four battery-powered AD743 low-noise FET operational amplifiers having an input impedance of about 300 GΩ, with an input voltage noise of ≈ 4 nV/$\sqrt{\text{Hz}}$, and a

---

[1]This frequency was chosen at random to eliminate interference with harmonics or sub-harmonics of other noise sources.
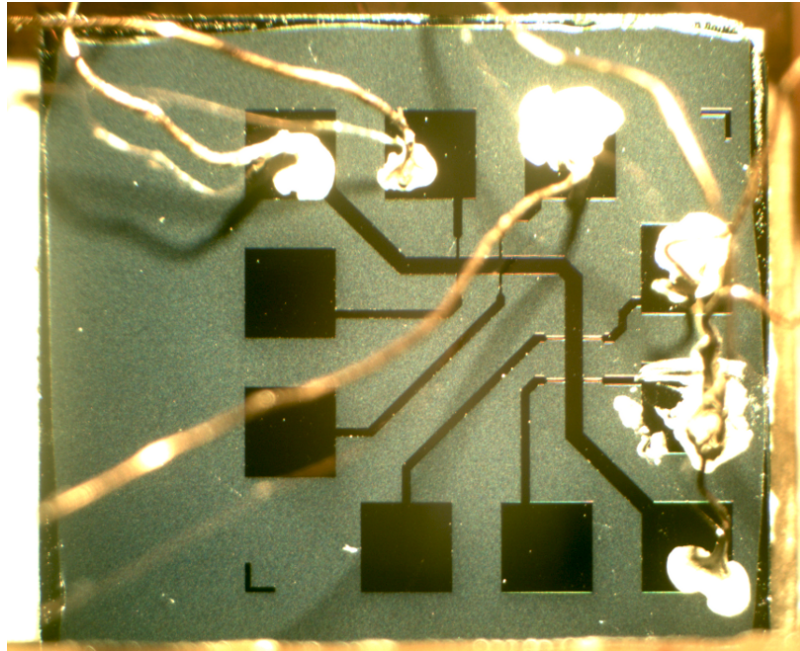
Figure 4.15: Sample mounted on MMR cold-finger and phosphor bronze wires attached with silver paint. This particular sample was wired for simultaneous resistivity measurement along the two in-plane crystallographic directions.

current noise of ≈ 30 fA/$\sqrt{\text{Hz}}$ at 20 Hz. Triaxial cable connections were used for the voltage contacts, with the inner shield connected to the output of the unity-gain FET buffers to provide guarding, thus eliminating any leakage currents and reducing capacitive phase shifts. The outputs from the FET buffers were connected differentially to two Stanford Research 830 lock-in amplifiers with a common-mode rejection ratio (CMRR) of > 100 dB.

4.3.3   Resistivity, Phase-Coexistence, and Phase-Hysteresis

Figure 4.16 shows a log-log plot of film resistivity versus temperature for the two in-plane crystalline directions.

From the log-log plot, one finds that the resistivity in the α-phase varies as T^2.
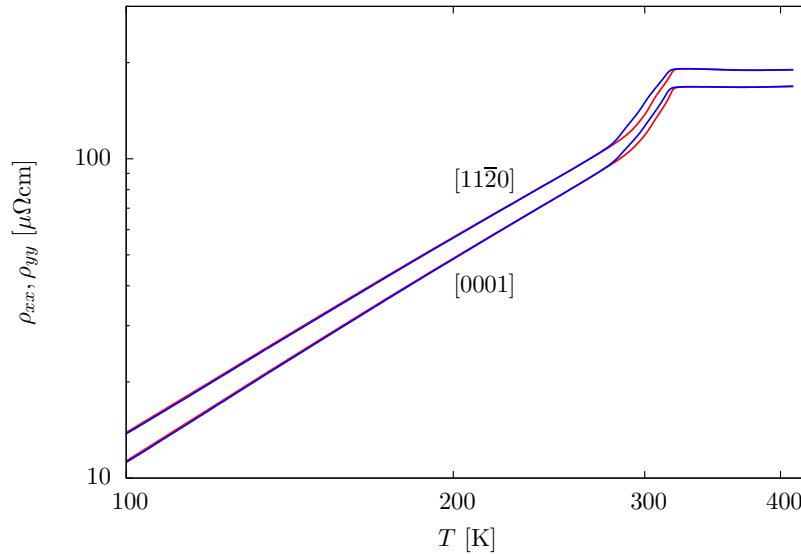
Figure 4.16: Log-log plot of resistivity versus temperature for the two crystalline in-plane directions. Note the hysteresis observed for heating (red) and cooling (blue). Temperature was ramped at 2 K/min.

This exponent can be ascribed to electron-electron or magnon scattering. For the β-phase, we find a very weak temperature dependence, usually with a slightly negative slope below 360 K. The origin of the negative slope will be discussed in Chapter 5. In the phase-coexistence region, a clear hysteresis is discernible, similar to the one observed in X-ray scattering experiments.

Resistivity Anisotropy

The resistivity of MnAs is anisotropic. Figure 4.17 shows the ratio of resistivity along GaAs [110] and along [1$\bar{1}$0]. Aside from the bump caused by the more complicated behavior in the phase-coexistence region, we see that for the unannealed samples the resistance of MnAs is larger for the [11$\bar{2}$0] direction by about 15% in the α-phase and 13% in the β-phase. Takagaki et al. report anisotropies of only 10% for α-MnAs and $7 - 8\%$ for β-MnAs [126]. The relatively high anisotropy compared to literature
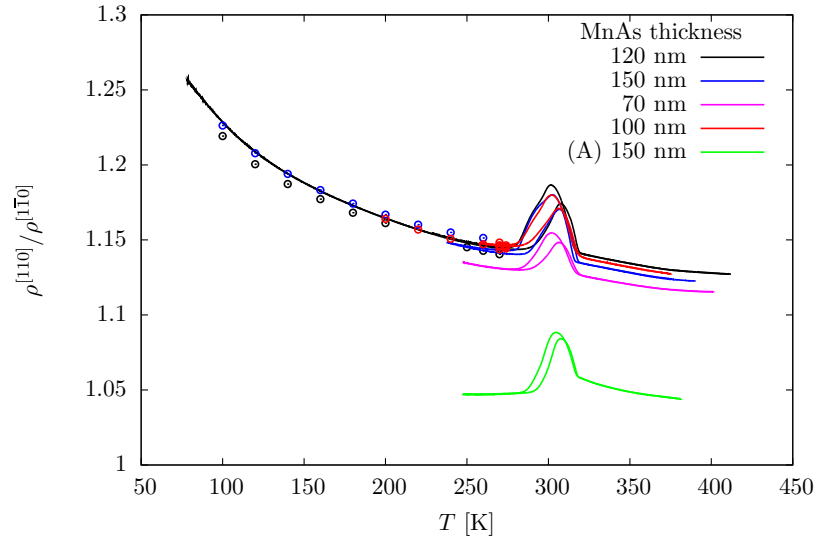
Figure 4.17: Ratio of the resistivities simultaneously measured along GaAs [110] and [1$\bar{1}$0] for different samples.

values for the unannealed samples provides evidence that our samples are almost purely in A_0 orientation. Furthermore, X-ray diffraction measurements for sample TE600 show that no B_0-oriented MnAs is present (see Section 5.2.3).

For the annealed sample, the anisotropy is much reduced, likely due to the presence of MnAs in both the A_0 and B_0 orientations.

Using the thickness determined by XRR (see 3.3.2), we find β-phase resistivities (at 340 K) of 1.68 $\mu\Omega$m for the c-axis and 1.88 $\mu\Omega$m for the a-axis. For comparison, absolute resistivities for thin-films at that temperature are given by Takagaki [126] as 2.57 $\mu\Omega$m and 2.78 $\mu\Omega$m respectively. The significantly higher resistivity seen by Takagaki may be due to the unusual geometry and complicated processing in their experiment. Interestingly, both numbers are much lower than the bulk number of 3.6 $\mu\Omega$m for the same temperature.

Phase Coexistence from Electrical Measurements

As alluded to before, the simple closed-form expressions for the effective conductivity tensor allow one to extract the relative phase fractions of a two component system, if the conductivities of the two components are known and sufficiently different. The simplest case is the σ_{xx}^e component, where from 4.6 we find

$$\rho_{xx}^e \approx \frac{1}{\sigma_{xx}^e} = \sum_i \frac{f_i}{\sigma_{xx}^i} \approx \sum_i f_i \rho_{xx}^i, \tag{4.14}$$

independent of any of the other tensor elements. The case of σ_{yy}^e is more complicated

$$\rho_{yy}^e \approx \frac{1}{\sigma_{yy}^e} = \left(\sum_i \frac{f_i}{\sigma_{yy}^i} + \sum_i \sigma_{yy}^i \frac{\sigma_{xy}^e - \sigma_{xy}^i}{\sigma_{xx}^i} \right)^{-1}, \tag{4.15}$$

but for $\sigma_{xy} \to 0$ (no Hall effect) simplifies to

$$1/\rho_{yy}^e \approx \sigma_{yy}^e = \sum_i f_i \sigma_{yy}^i \approx \sum_i \frac{f_i}{\rho_{yy}^i}. \tag{4.16}$$

These are the same expressions one would obtain by approximating α- and β-phase stripes by two different resistors, with the resistors in parallel for current along the stripes and resistors in series for current perpendicular to the stripes:

$$\frac{1}{\rho_\parallel} = \frac{f_\alpha}{\rho_\alpha^{[0001]}} + \frac{f_\beta}{\rho_\beta^{[001]}} \tag{4.17}$$

$$\rho_\perp = f_\alpha \rho_\alpha^{[11\bar{2}0]} + f_\beta \rho_\beta^{[100]}. \tag{4.18}$$

Here, the phase fractions are denoted as f_α and $f_\beta = 1 - f_\alpha$. To obtain the phase fractions, one has to extrapolate the pure α- and β-phase resistivities into the phase-coexistence regime. The pure α-phase shows quadratic temperature dependence and ρ_α is thus quadratically extrapolated from the low-temperature ($T < 270$ K) α-phase

resistivity. For the β-phase, the temperature dependence is very weak, and a linear extrapolation of ρ_β from $T > 335$ K seems sufficient. The resulting extrapolated resistivities are shown in Fig. 4.18.
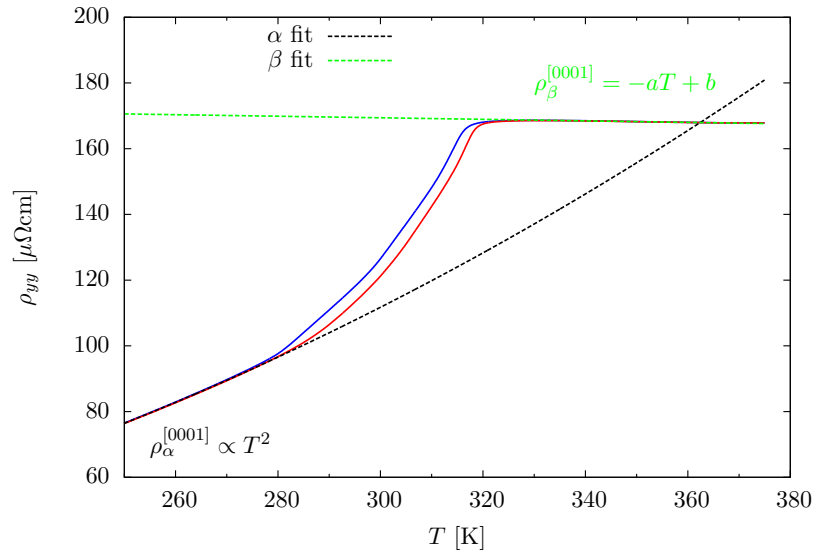
Figure 4.18: Temperature dependence of the measured in-plane [0001] resistivity, along with quadratic (α-phase) and linear (β-phase) extrapolation into the phase-coexistence regime.

The result of this procedure is the phase fraction as a function of temperature for heating ($f_\alpha^\uparrow$) and cooling ($f_\alpha^\downarrow$) cycles. Because the phase fraction can be determined independently from resistivity data for both in-plane directions, one also obtains two separate phase hysteresis curves, shown in Fig. 4.19. The close agreement between these two curves confirms the validity of the simple underlying model.

The same resistor model has already been proposed by Takagaki et al. [126]. In their data analysis, however, they used linear instead of quadratic extrapolation of the α-phase resistivity, leading to a rather poor agreement of the phase fractions derived for the two in-plane crystallographic directions (see Fig. 4.20). Their unusual sample geometry along with the complicated processing required for Ar milling of
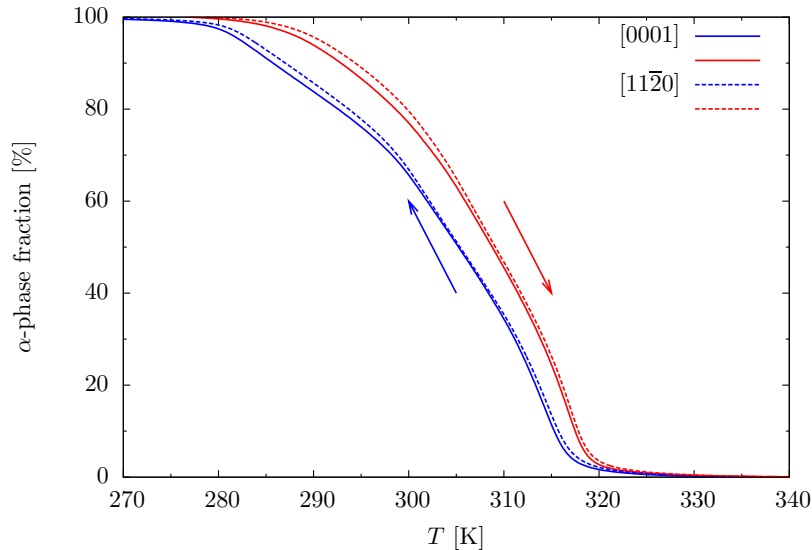
Figure 4.19: Temperature dependence of α-phase fraction determined from resistivity measurements for the [0001] (solid) and [11$\bar{2}$0] (dashed) directions. A clear hysteresis between cooling (blue) and heating (red) cycles is observed.

the MnAs film may have further deteriorated their results.

In our case, the agreement between the two independent models is excellent.

We can also compare data obtained from the resistivity measurements to the phase fraction determined from the area ratio of the X-ray diffraction peaks (Section 4.2). One such plot is shown in Fig. 4.21. The agreement between these two very different techniques is quite good, at least for high temperatures. The deviation at lower temperatures may be caused by the use of different pieces of the same wafer, difficulties of accurately fitting the overlapping X-ray peaks, or the different thermal cycling times used in both experiments. Even with this small error, we find that the thermal hysteresis is reproduced nearly equally by both techniques. For the other samples (see Appendix B), a similarly good correlation is found, with the exception of the in-situ annealed sample TE579, where the presence of both A_0 and B_0 orientations may cause the resistivity model to break down.
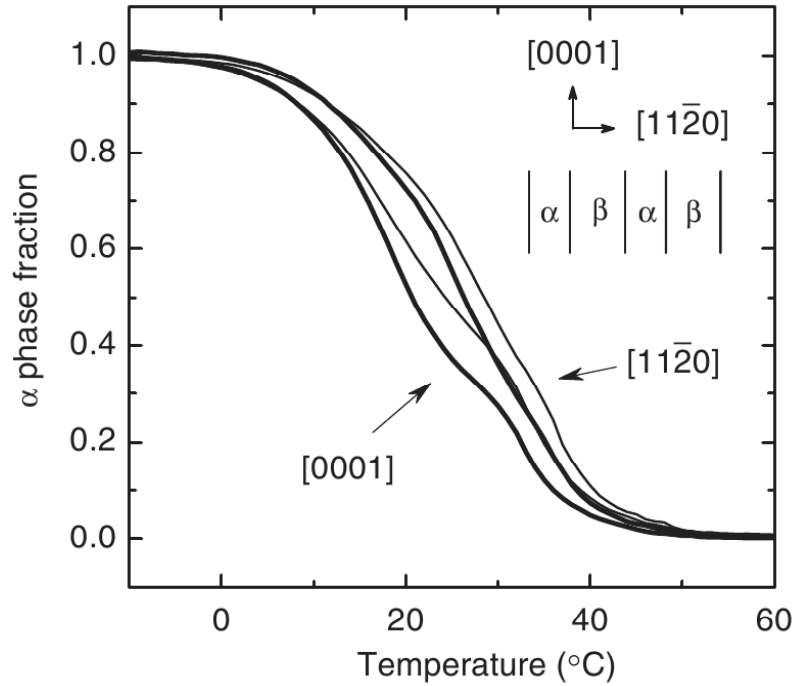
Figure 4.20: Phase fraction from resistivity for the two different in-plane crystalline directions from Takagaki et al. [126]. Reprinted with kind permission of Elsevier.

To be able to compare different samples, it is more instructive to separate the phase-coexistence hysteresis loops into two separate plots: the average phase fraction $\overline{f_\alpha(T)} = \frac{f_\alpha^\uparrow(T) + f_\alpha^\downarrow(T)}{2}$ is shown in Fig. 4.22, while the difference $\Delta f_\alpha(T) = f_\alpha^\uparrow(T) - f_\alpha^\downarrow(T)$ is shown in Fig. 4.23 for five different samples. In principle, one could also choose to perform the averaging and differencing at equal phase-fraction instead of equal temperature, but the latter is more convenient.

It is clear from these plots, that the average phase fraction behavior shows only small variations of $\approx 2 - 3$ K for these samples. This indicates that despite different film thicknesses and differences in growth conditions, the overall strain in the samples does not strongly alter the equilibrium phase fraction.

On the other hand, significant quantitative differences are found in the hysteretic
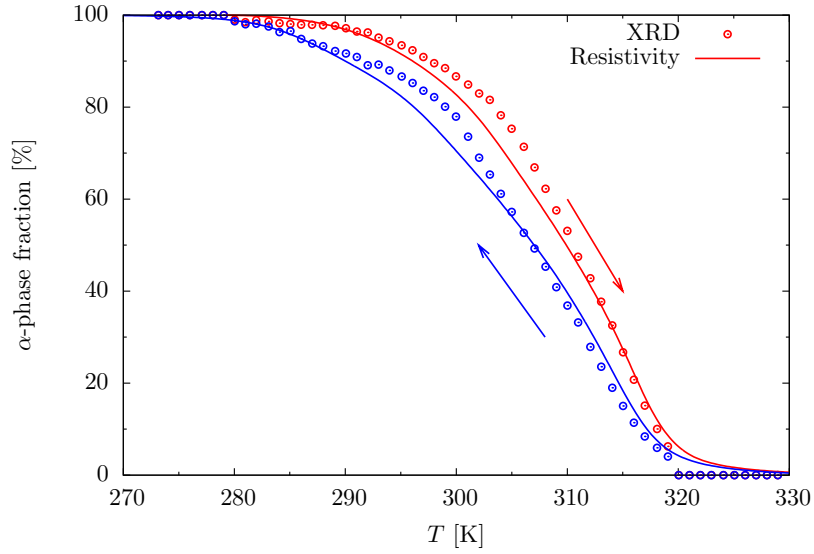
Figure 4.21: Phase fraction from resistivity (solid lines) and fitting of X-ray diffraction curves (symbols) for sample TE581.
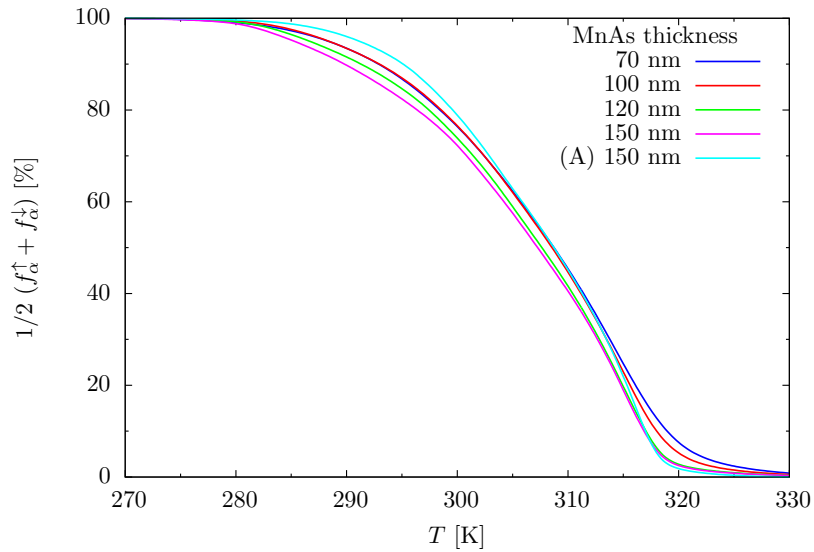
Figure 4.22: Average phase fraction from resistivity for five different samples.

behavior of the phase-coexistence. The 150 nm thick sample exhibits the strongest hysteresis, peaking at about 18%. The absence of a clear trend with sample thickness suggests that the difference may be mainly caused by variations in the growth con-
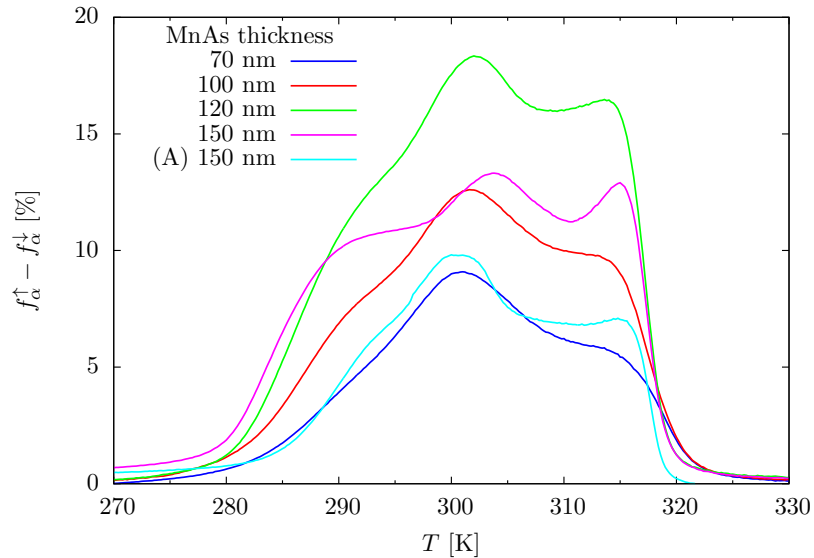
Figure 4.23: Difference in α-phase-fraction between heating and cooling cycles from resistivity measurements.

ditions. Despite these differences, all curves show qualitatively the same structure, namely a sequence of two maxima in Δf_α, the first at ≈ 300 K and the second at ≈ 317 K. For several of the samples, a shoulder around ≈ 290 K is also discernible.

Phase Fraction Hysteresis from X-Ray Diffraction

While the fitting of the X-ray results as described before is too noisy to resolve the structure in the phase hysteresis, we can use a different approach to obtain more accurate results. We will assume that the measured X-ray profile at any given temperature (corrected for the Cu $K_{\alpha 2}$ contribution) is the sum of the two line profiles

$$I_T(\omega) = f_\alpha(T)I_T^\alpha(\omega) + f_\beta(T)I_T^\beta(\omega), \tag{4.19}$$

with identical, basic line profiles $I_T^\alpha(\omega) = I_T^\beta(\omega - \delta\omega(T))$ shifted by $\delta\omega$, independent of the temperature history of the sample. Using diffraction patterns $I_T^\uparrow(\omega)$ and $I_T^\downarrow(\omega)$

measured at the same temperature, but for heating and cooling cycles, we then find

$$\int \left| I_T^\uparrow(\omega) - I_T^\downarrow(\omega) \right| d\omega = (f_\alpha^\uparrow - f_\alpha^\downarrow) \int \left| I_T^\alpha(\omega) - I_T^\beta(\omega) \right| d\omega. \tag{4.20}$$

With proper normalization ($\int I_T(\omega)d\omega \equiv 1$) of the measured profile to compensate for drift in X-ray intensity, we may then extract the phase fraction hysteresis $\Delta f_\alpha(T) \equiv f_\alpha^\uparrow(T) - f_\alpha^\downarrow(T)$ as

$$\Delta f_\alpha(T) = \frac{\int \left| I_T^\uparrow(\omega) - I_T^\downarrow(\omega) \right| d\omega}{\int \left| I_T^\alpha(\omega) - I_T^\beta(\omega) \right| d\omega}. \tag{4.21}$$

The denominator is ≈ 2 for non-overlapping peaks. An analytical expression depending on the peak separation $\delta\omega$ and the FWHM γ can be derived both for Gaussian and Lorentzian lineshapes. For the more complicated Voigt lineshape used in the actual fitting the integral cannot be given in analytical form. However, we may approximate it by taking the average of the Gaussian and Lorentzian integrals, i.e.

$$\int \left| I_T^\alpha(\omega) - I_T^\beta(\omega) \right| d\omega \approx \mathrm{erf}\left(\sqrt{\ln 2}\frac{\delta\omega}{\gamma_G} \right) + \frac{2}{\pi}\arctan\frac{\delta\omega}{\gamma_L}. \tag{4.22}$$

In our experiments, $\gamma_L \approx 0.032°$ and $\gamma_G \approx 0.055°$ are nearly independent of temperature. Because $\delta\omega$ is at least a factor of two larger (shown in Fig. 4.24), the correction due to peak overlap amounts to only a few percent at low temperatures and about 10% at 320 K.

Another contribution to the numerator of 4.21 is due to the statistical noise which of course differs from measurement to measurement. This is easily corrected for by subtracting the average noise contribution as determined from measurements at temperatures above 324 K where the true hysteresis signal is zero.

In Fig. 4.25 results obtained using this procedure are compared to results from electrical measurements. Although the agreement is not quantitative, good quali-
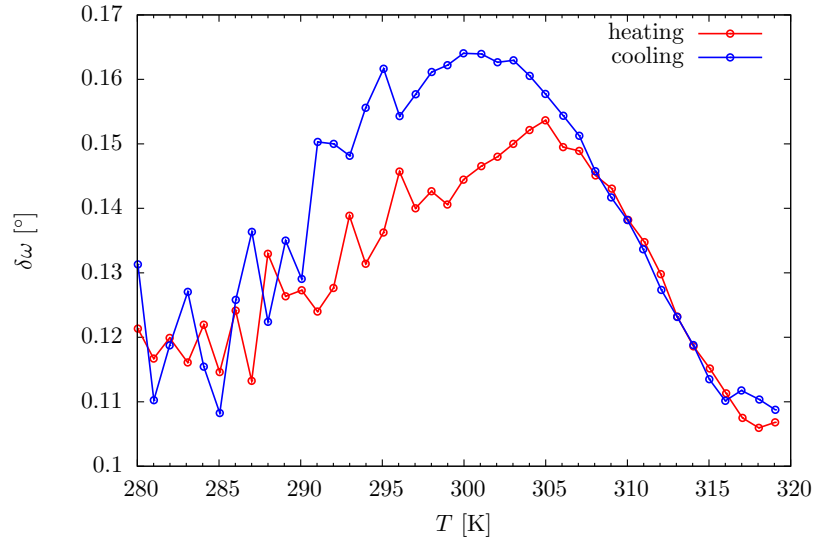
Figure 4.24: Typical separation of α and β-MnAs peaks versus temperature.

tative agreement is found for all three samples. In particular, three maxima in the hysteresis are well resolved.
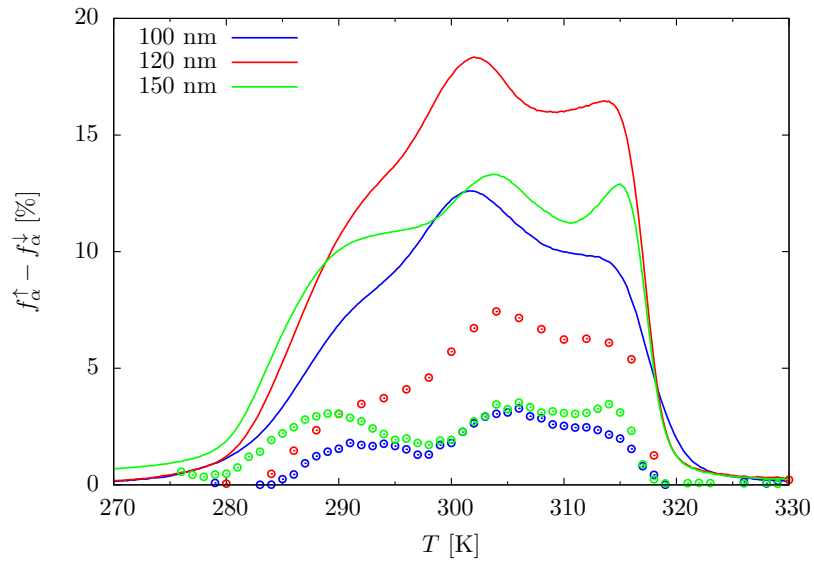
Figure 4.25: Difference in α-phase-fraction between heating and cooling cycles from resistivity (solid lines) and XRD (data points) measurements.

Several resons may account for the quantitative discrepancies:

- Different pieces of the wafers were used for the two techniques.

- Samples on the X-ray stage were not cooled below 276 K to avoid condensation. Thus, they may only represent minor loops (see next section).

- X-ray measurements took about 10 hours to complete, while less than 4 hours were needed for the electrical measurements. If there is any rate dependence in the hysteresis it may thus contribute.

- The electrical model may be overly simple.

Minor Hysteresis Loops

The ability to accurately determine phase fractions from electrical measurements allows us to inspect the hysteretic nature of the α- to β-transition in more detail. To this end, in addition to the full "envelope" hysteresis loops (EHL) shown above, we can also measure minor hysteresis loops (MHL) in two ways:

- Type I: Starting at low temperatures in the pure α-phase, we continuously heat the sample at a controlled rate to a target temperature within the hysteresis range. From here, we cool the sample back into the α-phase at the same rate and from the measured resistivities we calculate the phase fraction during the cooling cycle.

- Type II: Starting from the high temperature pure β-phase, we continuously cool the sample to a target temperature within the hysteresis range. From there, we heat the sample back into the β-phase.

In principle, these measurements could also be performed using X-ray diffraction, but the electrical measurements allow much more rapid and continuous determination of the phase fraction once the α- and β-phase resistivity fits have been established.

Measurements of minor hysteresis loops have been performed for other phase-coexistence materials: Chaudhary et al. [142] determined the capacitance-temperature hysteresis in the coexistence regime of the ferro- and paraelectric phases of $(\text{NaBi})_{1-x}\text{Ba}_x\text{TiO}_3$. Majumdar et al. [143] measured minor loops of the resistivity hysteresis at the martensitic transformation of a NiFeGa alloy. Hitherto, no such measurements have been reported for MnAs and this may be the first time that minor loops of the actual phase fractions have been determined for any material.

The result of such measurements is shown in Fig. 4.26. As in the previous section, for clarity we choose to show Δf_α instead of $f_\alpha^\uparrow$ and $f_\alpha^\downarrow$, and plot data from type I in the usual positive y-direction, while data from type II measurements is in the negative y-direction. If the measurements were executed perfectly, curves of the same temperature endpoints (color) from types I & II should join at the zero-line. The deviation from this ideal behavior allows one to roughly gauge the error of the measurement, which is relatively minor.

Looking at the cooling return curves, several features are noteworthy:

- Hysteretic behavior extends over a temperature interval of about 40 K.

- After the sample is cooled to only about 315 K (20% α-phase), the return branch already shows a considerable hysteresis.

- As the cooling endpoint temperature increases, hysteresis is increased at *all* higher temperatures.

- Even if the sample is cooled to about 280 K ($\approx 95\%$ α-phase), the return branch still shows substantially lower hysteresis than the heating envelope curve.
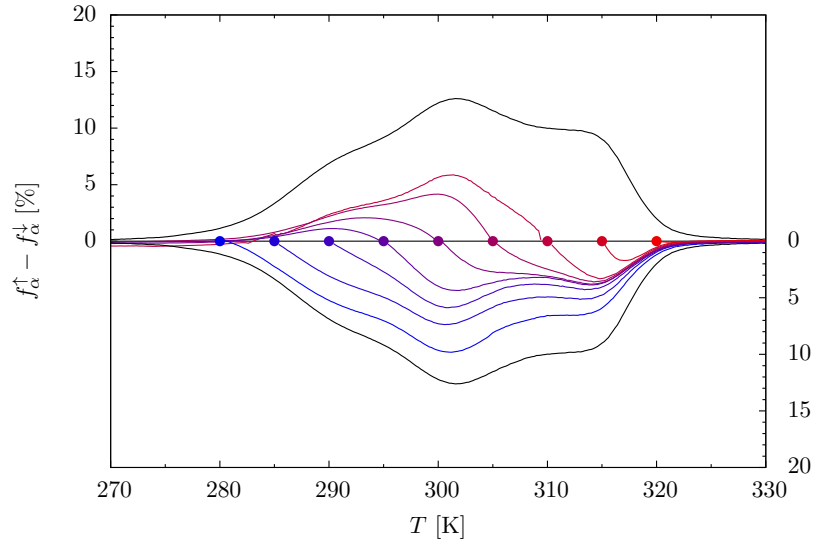
Figure 4.26: Phase-fraction hysteresis Δf_α for major (black) and minor (color coded according to end-point temperature) hysteresis loops for the 100 nm thick sample. Heating-return curves ("type I") are shown in the upper half, cooling-returns ("type II") are shown in the lower half.

Analogous observations can be made for the heating return curves, although here the hysteresis in the low temperature regime develops much more gradually.

Comparing loops obtained in this manner for three different samples (Fig. 4.27), we find qualitatively the same behavior. In particular, three peaks are discernible in the hysteresis. From an energetic standpoint, the appearance of peaks in the hysteresis should be related to energy barriers between these peaks, or, equivalently, extended local energy minima at these temperatures. To understand the origin of these features, we seek to relate them to qualitative structural changes in the films: The peak at $\approx$ 303 K roughly coincides with the sample being in a roughly 50% α, 50% β state, where both phases are in a highly ordered striped state, as seen in the AFM images in Section 4.1. The peak at just above 315 K can be related to the nucleation of disordered, striped inclusion of α-phase inside the relatively well ordered β-phase, while the less well developed peak around 290 K may be related to

(a) 70 nm

(b) 120 nm

(c) 150 nm, annealed
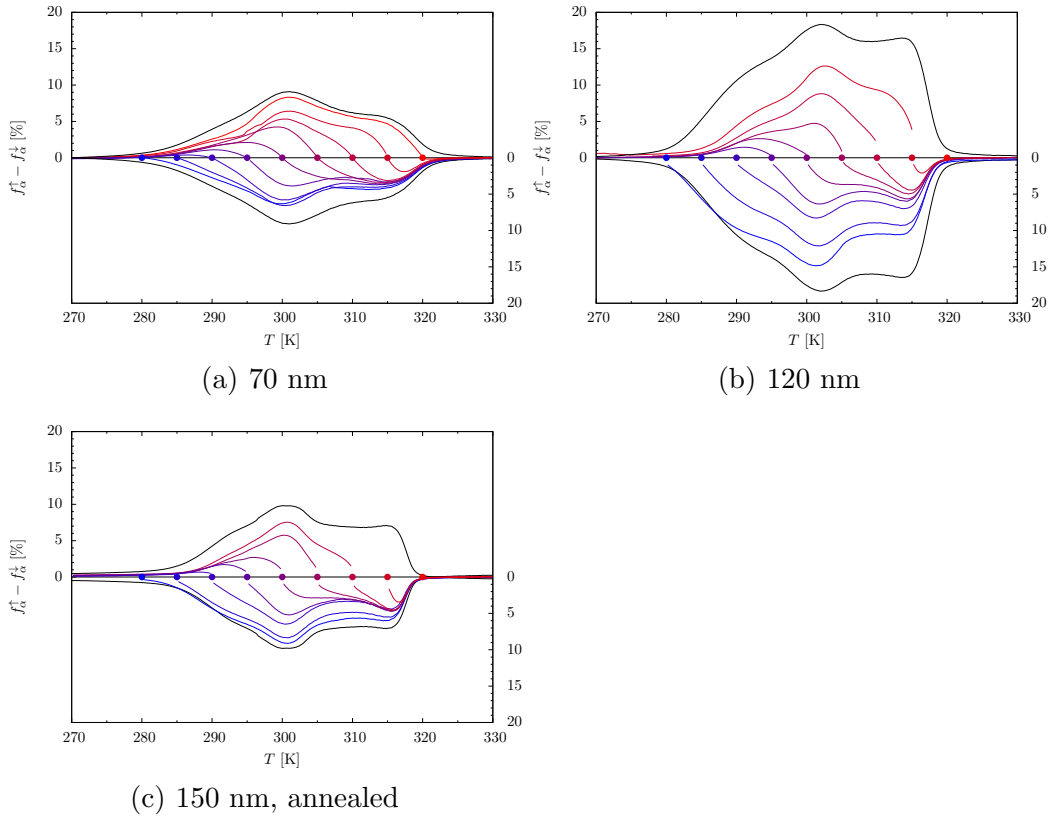
Figure 4.27: Phase-fraction hysteresis Δf_α for major (black) and minor (color coded according to end-point temperature) hysteresis loops for samples of different thickness.

the nucleation of β-phase inside the ordered α-phase continuum.

4.3.4 Hall Effect and Magnetoresistance

The anomalous Hall effect dominates the ordinary Hall effect in magnetic materials and can be used as a sensitive probe of their perpendicular magnetization. As such, it complements other probes of magnetization, such as SQUID magnetometry (which yields only bulk information) and magnetic force microscopy. While the latter is an extremely useful technique giving access to spatially resolved information

(a) 304 K   (b) 300 K
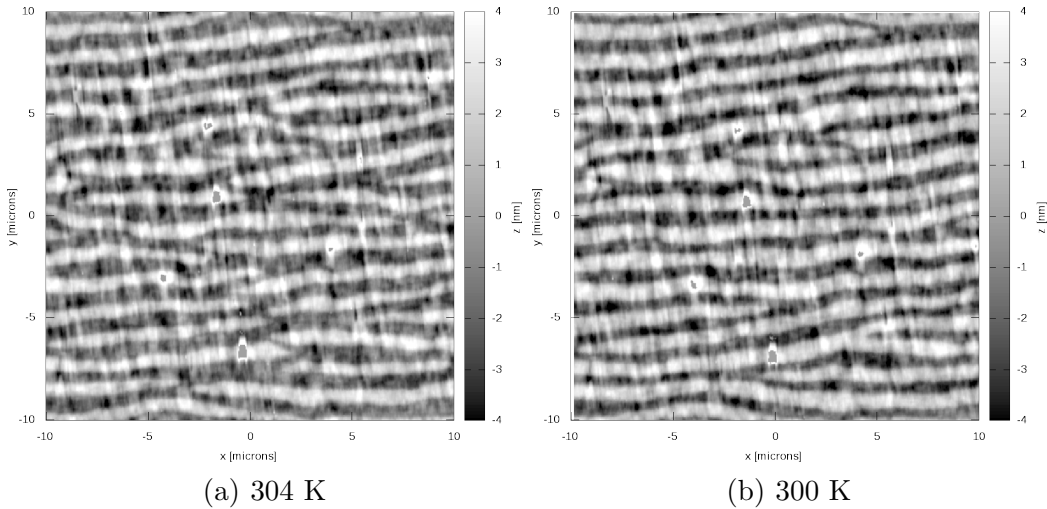
Figure 4.28: AFM images of sample TE568 during cooling.

on magnetic domain structure, it still suffers from several drawbacks:

- Considerable care in the measurement is required to remove the influence of topographic features on the scanned image. While this is not too much of a concern with uniformly flat films, this becomes a serious issue in the case of MnAs, where a strong spatial modulation exists due to the phase-coexistence.

- As a measurement of the stray field carried out above the surface of the sample, the interpretation of the image requires the solution of an "inverse problem". In practice, this is achieved in an iterative process of forward calculation from a model of the magnetic structures of both sample *and* magnetic tip, comparison with the experimental result, and refinement of the model. The complexity of this problem can be gauged from the number of publications dealing with the interpretation of MFM images in MnAs [116, 118, 144, 144, 145, 146, 147].

- The stray field of the tip may alter the magnetic structure of the domains in the sample.

We therefore propose that magnetization measurements obtained through the anoma-
lous Hall effect should complement the magnetic force microscopy studies.

Berry et al. [125] have surveyed magnetotransport in MnAs thin-films between 2
and 360 K with high magnetic fields. Unfortunately, at the time of their study they
may not have been aware of the ordered phase coexistence of α- and β-phases, first
described by Kaganer et al. in a paper [69] published in July 2000. Consequently,
they provided little interpretation of their results, aside from the AHE in the pure
α-phase. The anisotropy of conductivity was also neglected and may have gone
unnoticed if their MnAs films exhibited random epitaxial orientations. In any case,
for temperatures below 150 K, they were able to separate the AHE contribution of
the Hall effect from the ordinary contribution by fitting the measured ρ_{xy} using

$$\rho_{xy} = R_H B_0 + a\rho_{xx}(B_0, T)^\gamma M(B_0, T), \tag{4.23}$$

where $M(B_0, T)$ is the magnetization measured in a separate experiment. Such fits
yielded $\gamma = 1.8 \pm 0.2$. Unfortunately, the value for a was not reported in their
publication. Using a computer program [148], we were able to extract the necessary
raw data for $T = 150$ K from plots in their publication to perform the fit. Due to
experimental limitations, magnetization was only measured for applied fields of up to
7 Tesla, but was linearly extrapolated for the fits. Unfortunately, the quality of the
magnetization plot in Berry et al. [125] is rather poor, and the resulting inaccuracies
for the extracted numbers lead to deviations of the fit at low fields (see Fig. 4.29).

Almost identical fits were obtained for $\gamma = 1.8$ and $\gamma = 2$, implying that the
statistical error for γ is large. For convenience, we make the choice $\gamma = 2$. Naturally,
the value of a depends strongly on the choice of γ. For $\gamma = 2$ we obtain $a \approx$
$1.14 \cdot 10^{-3} (\mu\Omega \text{cmT})^{-1}$, which we will use in the following to show absolute values of
magnetization.
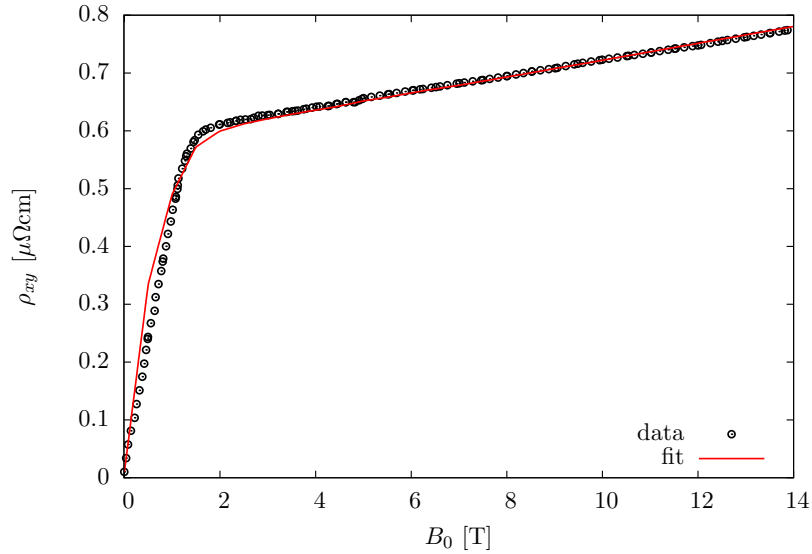
Figure 4.29: Fits of Hall resistance obtained for data from Berry et al. [125]. The fit results for $\gamma = 1.8$ and $\gamma = 2.0$ are indistinguishable.

Hall effect and magnetoresistance were measured for each sample orientation in separate experiments. Measurements were performed by sweeping the magnetic field from -0.9 to +0.9 and back to -0.9 T.

Pure α-Phase

In the pure α-phase, i.e. below about 270 K, the Hall effect is completely linear in the magnetic-field and temperature range investigated here. Moreover, no hysteresis between increasing and decreasing fields is observed. This is expected, as for a continuous single-phase thin-film the magnetic shape anisotropy makes out-of-plane domains unfavorable. However, magnetization out-of-plane can still be induced by the external magnetic field.

Figure 4.30 shows the slope $\frac{d\rho_{xy}}{dB}$ for the two different in-plane crystallographic directions. No significant difference between the two directions can be detected.
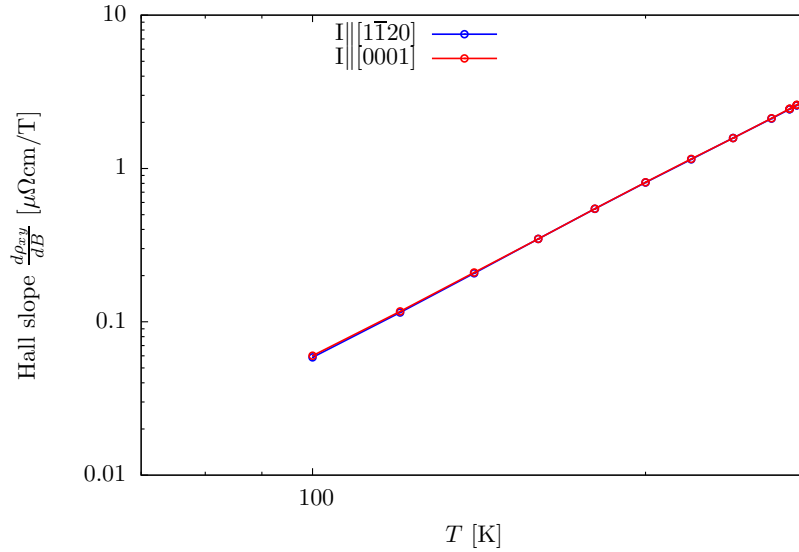
Figure 4.30: Hall coefficient from ρ_{xy} and ρ_{yx} in the α-phase for the 70 nm thick sample. The curves coincide.

On a log-log-plot, the Hall slope is a straight line, i.e. it can be described by $\frac{d\rho_{xy}}{dB} = a \cdot T^b$. Figure 4.31 shows the slope for five different samples for the $[11\bar{2}0]$ direction, and we find that it is almost identical for this set of samples, with $b \approx 3.68$. This exponent is the result of the anomalous Hall effect scaling with ρ_{xx}^2, which in turn scales as T^2.

From equation 2.40, we can find the susceptibility as

$$\chi_\perp \approx \frac{\partial \rho_{xy}/\partial B}{a\rho_{xx}^2}. \tag{4.24}$$

The result of this analysis is shown in Fig. 4.32.

The Phase-Coexistence Regime

Data was collected for both heating from the pure α-phase and cooling from the pure β-phase. Figure 4.33 shows the evolution of Hall and relative magnetoresistance over the phase coexistence region. The following observations can be made for all samples:
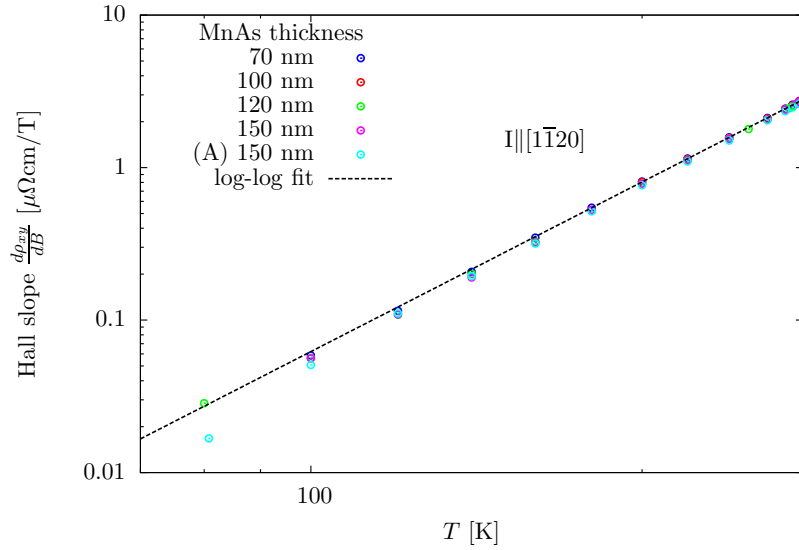
Figure 4.31: Hall coefficient from ρ_{xy} in the α-phase for five different samples. The dashed line is a fit to $\frac{d\rho_{xy}}{dB} = a \cdot T^b$.
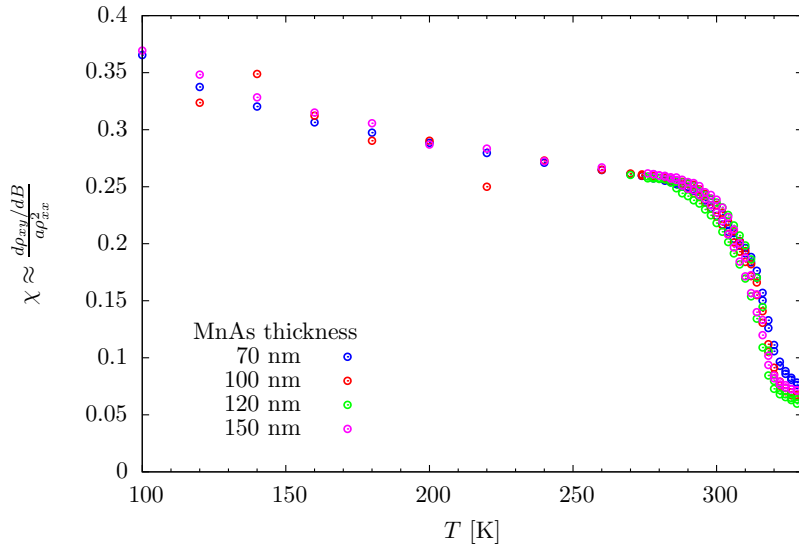
Figure 4.32: Out-of-plane susceptibility derived from anomalous Hall effect measurements. For a, the value from Section 4.3.4 was used.

- Upon heating, a hysteresis in the Hall resistance appears somewhere between 290 and 300 K depending upon sample.

- At temperatures above 310 K, this hysteresis rapidly diminishes.

- The Hall resistance is characterized by two separate slopes, as is typical for the anomalous Hall effect.

- A clear thermal hysteresis is found for both Hall and magnetoresistance.

Hysteresis

To further analyze the data, several parameters were extracted from the Hall hysteresis curves.

As shown in Fig. 4.34, the "strength" of the hysteresis was determined from the integral $\int \rho_{xy} \, dB$. Furthermore, linear fits provide low and high field slopes.

Figure 4.35 shows a plot of the integrated area under the Hall hysteresis loop versus temperature, measured for cooling and heating cycles. Results for the two different in-plane directions are almost identical. The strong thermal hysteresis proves that the out-of-plane Hall hysteresis is directly connected to the phase-coexistence. An interesting feature is the second, smaller peak in the hysteresis area at higher temperatures.

A plot of the hysteresis loop (Fig. 4.36) at 318 K shows that the loop is incomplete. Most likely the applied magnetic field is strong enough to convert some β-back into α-MnAs. It would be revealing to witness this effect with AFM.

Since the appearance of hysteresis is intimately connected to the phase coexistence, it makes sense to analyze hysteresis parameters as a function of phase fraction. As we have seen in Section 4.3.3, we may use the zero-field resistivity to derive the phase fraction for any given measurement.
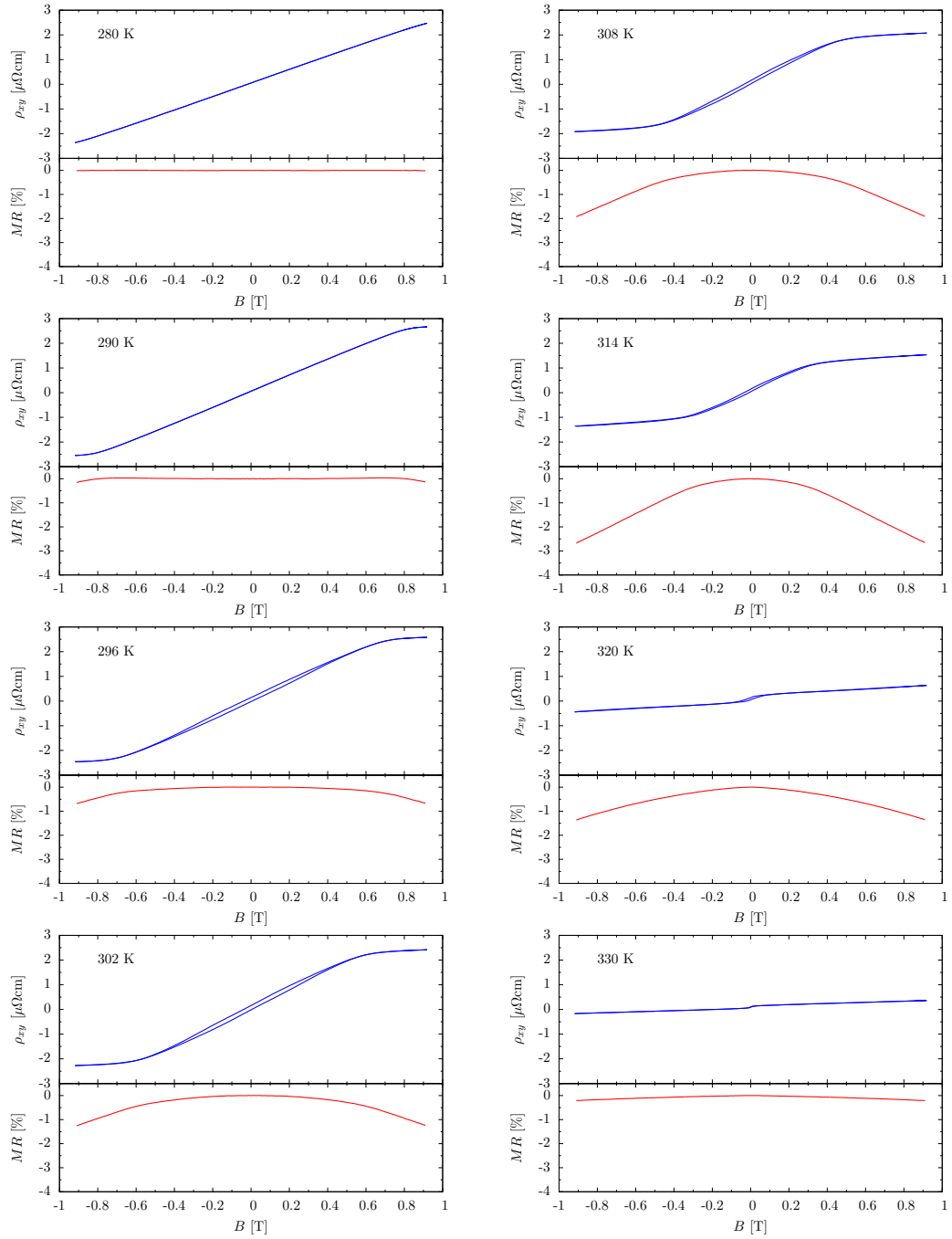
Figure 4.33: Overview of Hall and magnetoresistance (MR) in the phase-coexistence regime (sample TE578H1L).
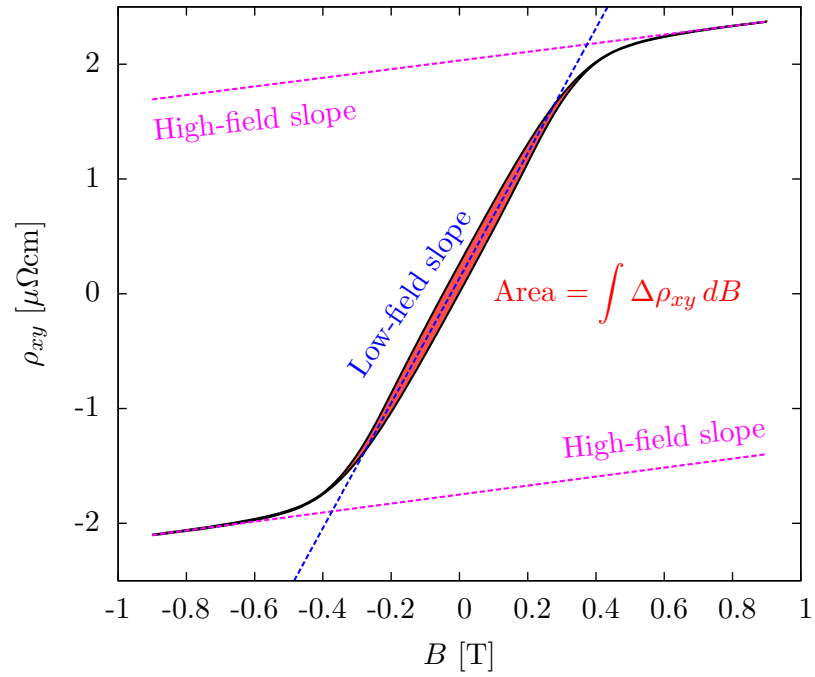
Figure 4.34: Scheme for extraction of hysteresis loop area (red), as well as high- (dashed magenta) and low-field (dashed blue) slopes from Hall resistivity curves.
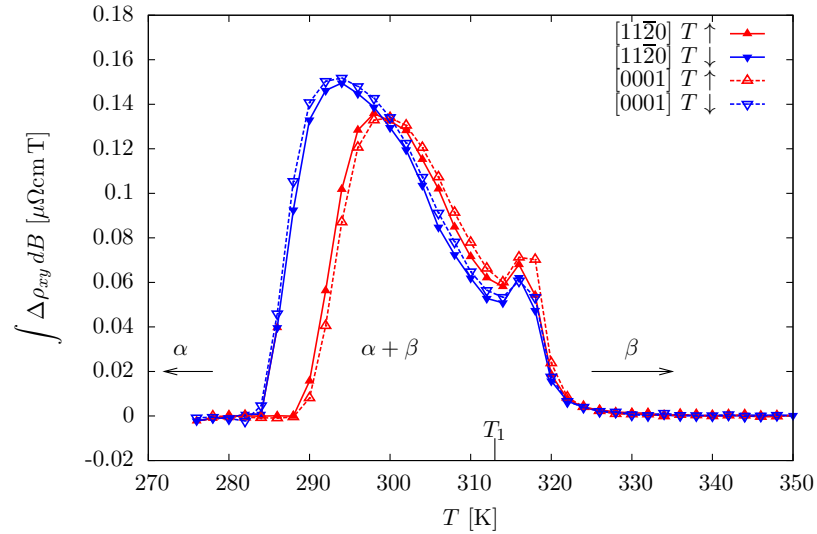
Figure 4.35: Area of Hall hysteresis loop versus temperature for heating (red) and cooling (blue).
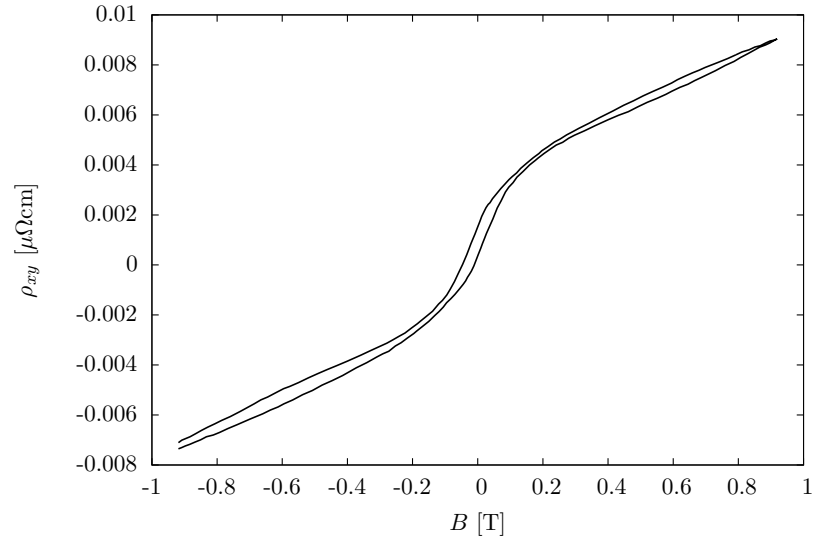
Figure 4.36: Hysteresis loop of the Hall resistance at 318 K.

In Fig. 4.37 we show the area of the hysteresis loop versus phase fraction for both heating and cooling.
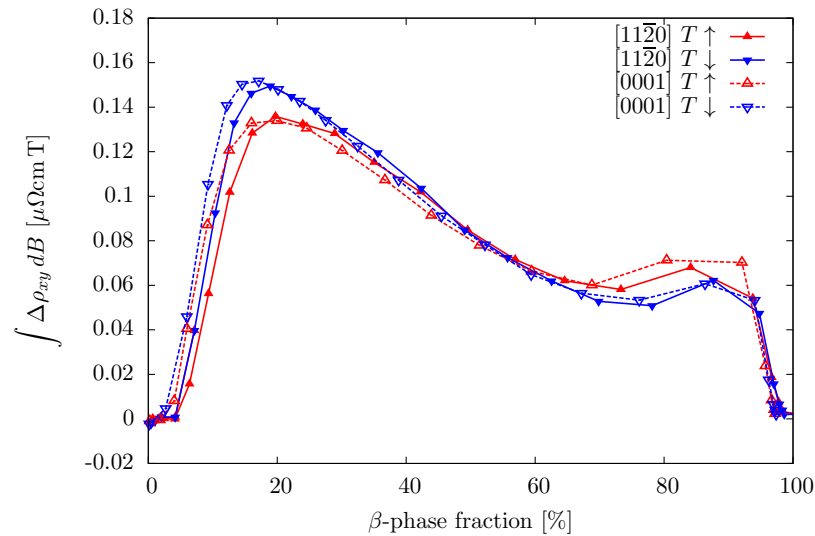
Figure 4.37: Area of Hall hysteresis loop versus β-phase fraction for heating (red) and cooling (blue).

The curves for heating and cooling nearly coincide, identifying the phase fraction

as the governing order parameter for the hysteresis. The hysteresis in out-of-plane magnetization is due to the breaking up of the continuous α-phase film into separated stripes. While in the continuous film stable out-of-plane domains are strongly suppressed due to the shape anisotropy, the situation is different for narrow α-MnAs stripes. Naively, one may expect a prevalence of out-of-plane domains once the height to width ratio $\frac{t}{w_\alpha}$ of the stripes is greater than one. With the stripe period given by $\Lambda \approx 5t$ and the width of the α-phase stripes $w_\alpha = f_\alpha \Lambda$, we find $f_\alpha < 20\%$. In contrast to this simple argument, Fig. 4.37 shows that even for a small fraction of β-phase, hysteresis is observed, with the hysteresis loop area maximal for a phase fraction of about 20%. Of course, for the complex domain structures as they exist in MnAs, the assumption of a simple demagnetization factor cannot be valid and a full micromagnetic simulation, taking into account also the variability of stripe width would be necessary to obtain a clearer picture.

In the spirit of effective media theory (see Section 2.4.3), it seems justified to normalize the hysteresis signal by the fraction of the α-phase f_α since only this phase is expected to contribute to the AHE signal. Figure 4.38 shows this normalized hysteresis loop area for a set of different samples. Again, the curves are qualitatively very similar, with the peak at high β-fraction caused by the incomplete hysteresis loops observed when β-phase is converted to α by the applied magnetic field. Between about 20 and 80% phase fraction, on the other hand, the normalized hysteresis is nearly constant, confirming that the hysteresis signal originates in the α-phase stripes. The somewhat different behavior of the thinnest sample may be due to increase significance of inter-stripe coupling for smaller stripe spacing. This would presumably favor in-plane magnetization, and indeed, we find the onset of out-of-plane domains at a larger β-fraction for this sample.

The magnetoresistance (MR) in a field of 0.9 T is shown in Fig. 4.39. In the pure α- and β-phases, magnetoresistance is very small. Within the phase-coexistence
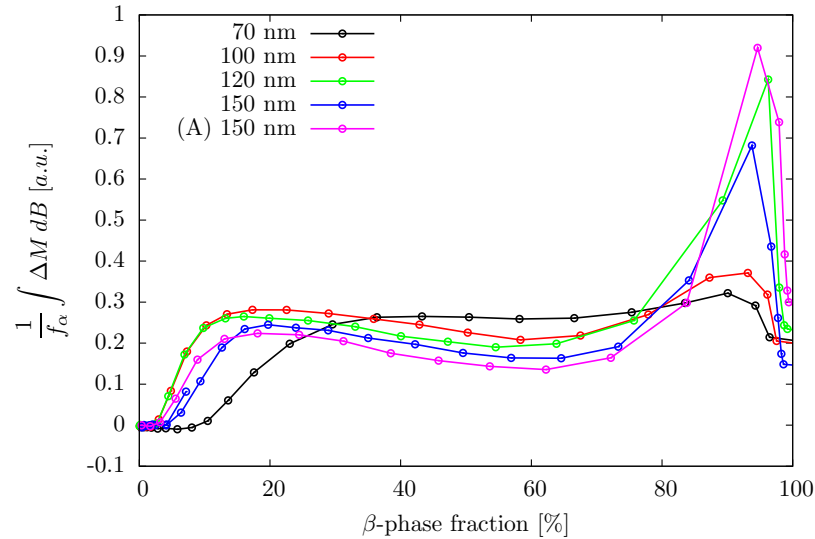
Figure 4.38: Normalized area of Hall hysteresis loop versus β-phase fraction for different samples.

region, negative peak is observed around $316\ K$. This can be understood as a reduction in disorder scattering when domains are aligned by the external magnetic field. Some fraction of the magnetoresistance effect at the high temperature end is likely associated with the back-transformation to the lower-resistivity α-phase.

In addition to the complex micromagnetic situation, a detailed model of the hysteresis curves would also have to take into consideration that back-transformation of β- into α-phase cannot be neglected at the high-temperature end of the phase coexistence. Furthermore, the exact dependence of the anomalous Hall effect on the temperature- and directionally-dependent resistivities of the magnetic α-phase and (presumably) non-magnetic β-phase. These important issues are outside the scope of this dissertation and the interpretation of the Hall data remains necessarily incomplete. It is hoped, however, that the above results may in the future be understood from refined micromagnetic models, and a more fully developed theory of the anomalous Hall effect in inhomogeneous and anisotropic systems.
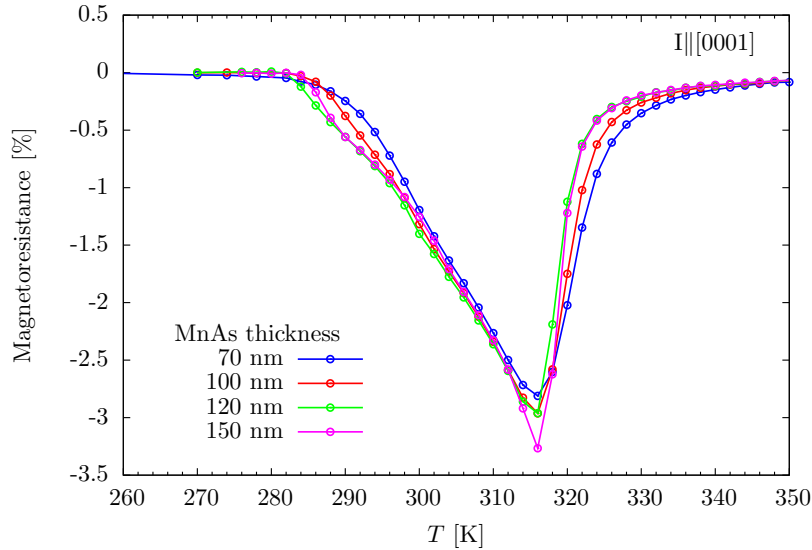
Figure 4.39: Magnetoresistance at 0.9 T for different samples.

4.4 Magnetic Order in the β-Phase

If some kind of magnetic order indeed exists in the β-phase, evidence of the magnetic scattering may be found in magnetotransport measurements. Aside from resistance measurements by Takagaki et al. [126, 128] and the somewhat cursory Hall measurements at 340 and 360 K by Berry et al. [125], no measurements in this range have been reported. To investigate this issue, the temperature range for Hall measurements was extended to above 400 K, covering the presumed existence range of the β-phase, and the beginnings of the γ-phase.

The upper temperature limit is given by the onset of thermally activated parallel conduction in the substrate. Since parallel conduction in the substrate effectively destroys the geometrically well defined Hall-bar geometry, its onset may be detected by a simultaneous measurement of two symmetric contact pairs of the Hall-bar. In Fig. 4.40 the relative deviation of longitudinal voltages measured from the pairs at the top and bottom of the same Hall-bar device is shown. Very minor deviations
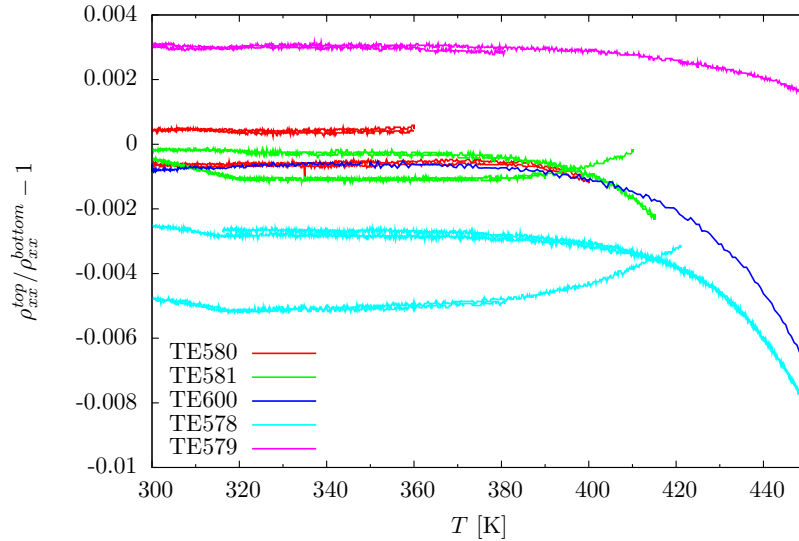
Figure 4.40: Relative deviation of longitudinal resistivities measured on top and bottom Hall-bar contact pairs. Where available, measurements for Hall-bars of both in-plane orientations are shown.

of up to $5 \cdot 10^{-3}$ (more typically $\leq 1 \cdot 10^{-3}$) from the ideal ratio of 1 are found for temperatures up to ≈ 400 K, evidence of the excellent homogeneity of the films and the accurate alignment of the voltage probes. At higher temperatures, parallel substrate conductivity leads to the breakdown of symmetry.

4.4.1 Results

As can be seen from Fig. 4.41, the hysteresis loop does not completely close up to about 335 K. Hysteresis is the hallmark of ferromagnetism and for a purely para-magnetic material, no such hysteresis would be expected. It seems therefore likely that some small amount of α-phase persists at temperatures above 320 K.

At even higher temperatures, the Hall effect at *high fields* is small and completely linear. Near zero field, however, we observe a sharp step. Figure 4.42 shows the Hall resistance in the β-phase after subtraction of the high-field linear part.
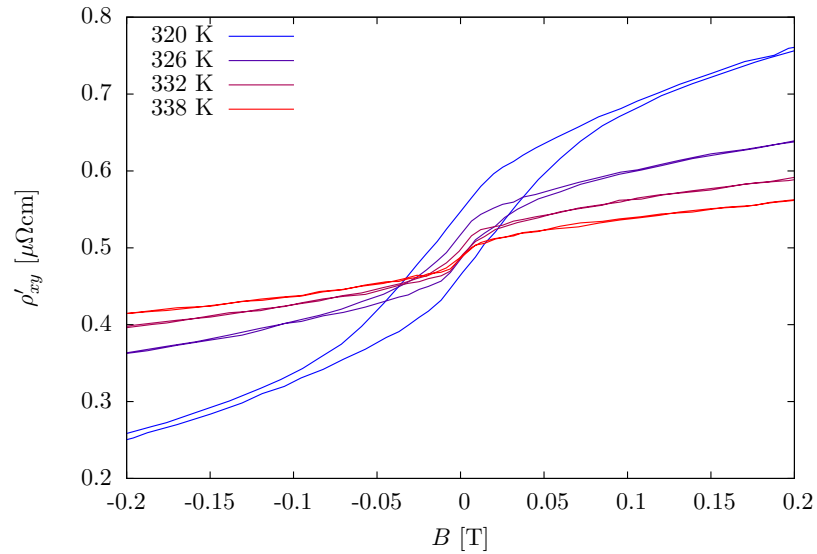
Figure 4.41: Hall hysteresis loops in the β-phase.
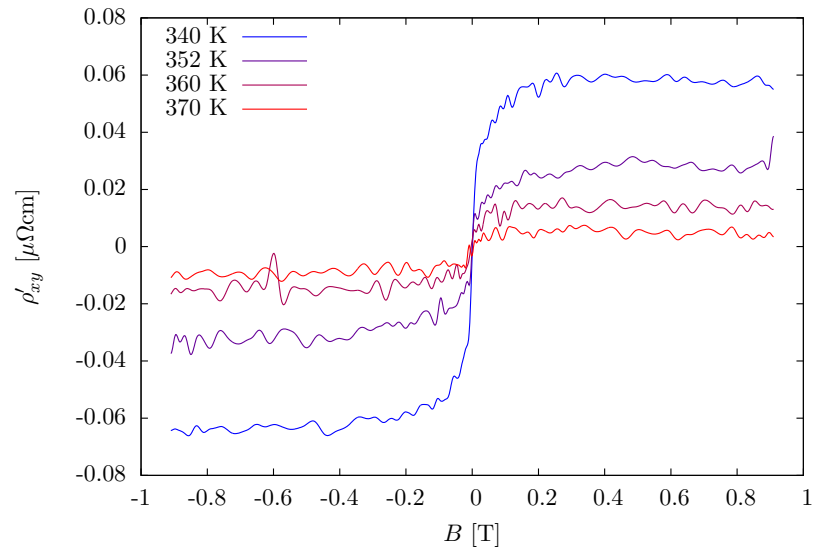
Figure 4.42: Step in the Hall resistance in the β-phase. For clarity, linear high-field dependence has been subtracted and positive- and negative-going field sweeps have been averaged.

Surprisingly, this step is detectable up to 390 K, where we would expect the sample to be purely in the β-phase (or γ-phase, see Chapter 5). For further analysis,

we may fit the Hall resistance ρ_{xy} using the following expression:

$$\rho_{xy} = \rho_{xy}^s \tanh\left(\frac{H \pm H_c}{H_s}\right) + \chi_{hf}H, \tag{4.25}$$

which is analogous to commonly used expressions for magnetization loops (see for example Barabash and Stroud [149])

$$M = M^s \tanh\left(\frac{H \pm H_c}{H_s}\right) + \chi_{hf}H. \tag{4.26}$$

Here, ρ_{xy}^s and M^s are the saturation Hall resistance and magnetization, H_c is the critical field, H_s is the saturation field, and χ_{hf} describes the high-field ("paraprocess") susceptibility. We show two such fits in Fig. 4.43.
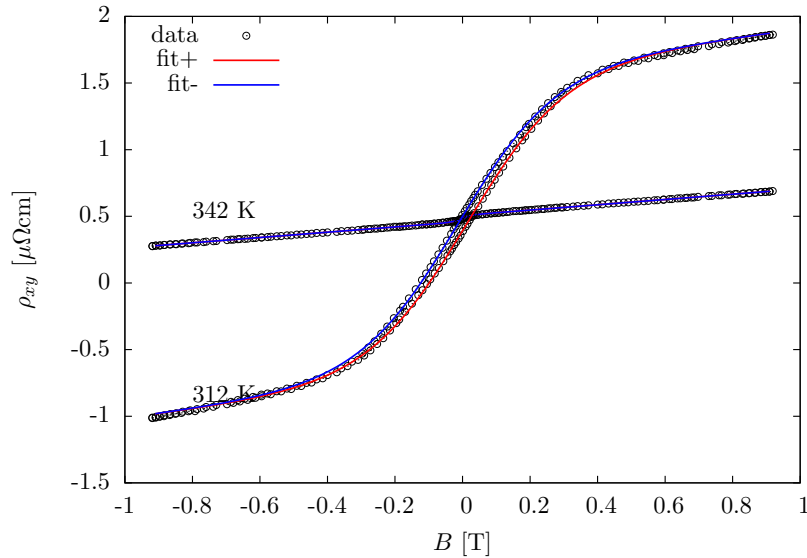
Figure 4.43: Raw Hall resistivity and fits with equation (4.25) for two temperatures.

With the expressions for the anomalous Hall effect, from these fits we can deduce a saturation magnetization as

$$M^s \sim \rho_{xy}^s/\rho_{xx}^2, \tag{4.27}$$

which we plot in Fig. 4.44 for different samples. Also shown is the high-field "susceptibility" χ_{hf} (Fig. 4.45). In the β-phase, both M^s and χ_{hf} decay nearly exponentially with temperature, with very similar absolute values for all samples.
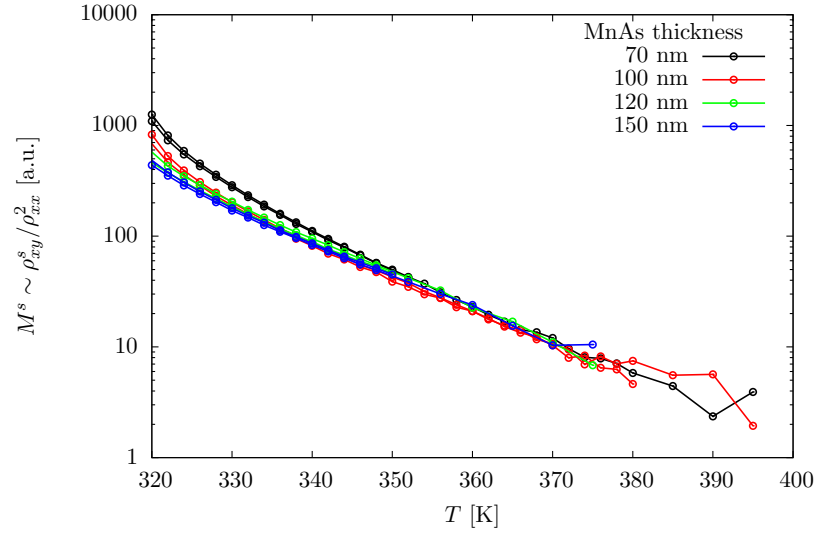
Figure 4.44: Saturation magnetization M^s versus temperature for four samples.
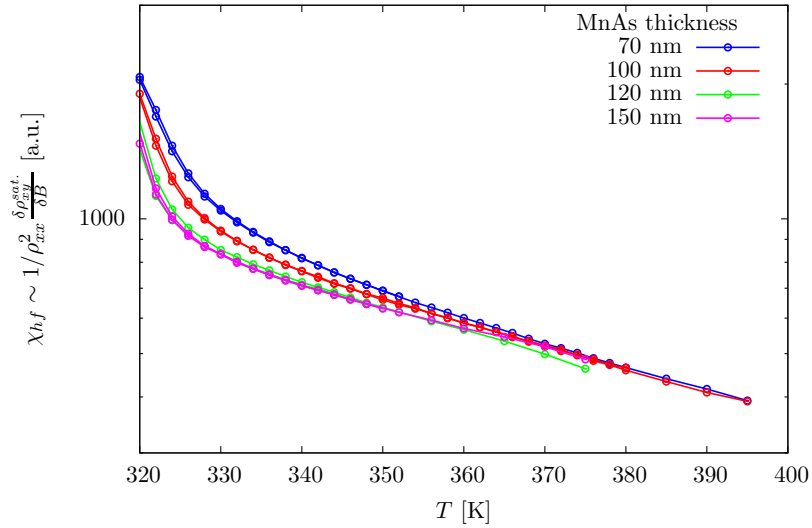
Figure 4.45: high-field susceptibility χ_{hf} versus temperature for four samples.

Below, we will investigate two possible origins of the Hall anomaly:

- Back-transformation of β- to α-MnAs due to the applied field.

- Existence of a ferromagnetic impurity phase.

Back-Transformation to α-phase?

We have seen that the application of an external magnetic field may cause the transformation of a small fraction of the β-phase to the magnetic α-phase. To investigate whether this might cause the observed step, the measurements were repeated with a smaller field range of only ±40 mT. Surely, such small fields could not induce a phase transformation of any significant magnitude. At the same time, to rule out an experimental artifact from the polarity switching of the high current power supply, these measurements were performed with a programmable bipolar power supply (Keithley Instruments Model 228) in order to be able to vary the field through zero in a smooth and continuous fashion.

In Fig. 4.46 we compare the low-field Hall resistance measured using the reduced field swing with those obtained with the full field swing (±0.9T). While raw data are shown for the high-field measurement, the low-field Hall resistances were shifted vertically to compensate for drifts in the Hall offset. The results are nearly identical. We can thus rule out both experimental error or the back-transformation of β- into α-phase as the cause for the step observed at low fields.

In contrast, near the upper end of the phase transition temperature, a clear difference between the hysteresis loops obtained with small and large field ranges is evident, see Fig. 4.47. While this difference may in part be caused by the magnetic-field induced back-transformation of β- into α-phase, the main origin is probably the incomplete magnetic saturation achieved in the low-field measurement, i.e. only the minor loop of magnetization is traced out.

Ferromagnetic Impurity Phase

An out-of-plane magnetization component in films of β-MnAs was already detected by Ney et al. [150]. In MFM measurements, they noticed small isolated magnetic con-
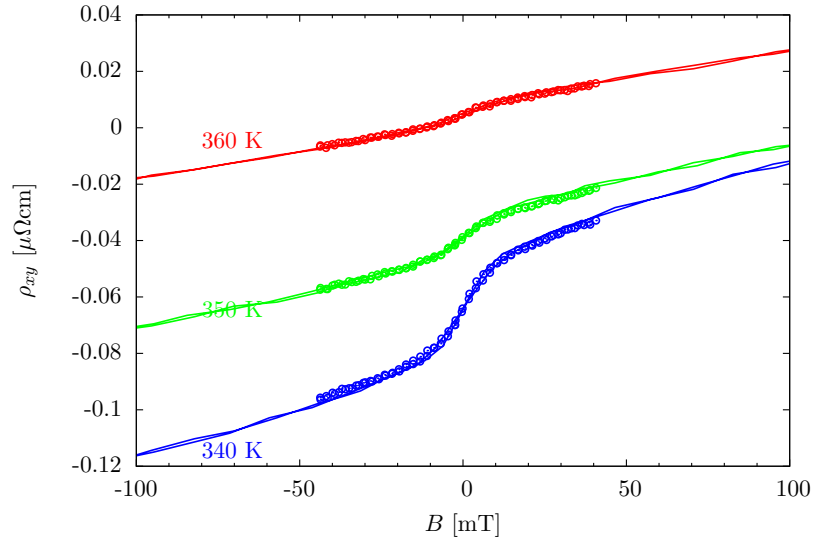
Figure 4.46: Comparison of Hall resistance measurements performed with the full field range of ±0.9 T (solid lines) and with reduced range of ±45 mT (data points) for three different temperatures.
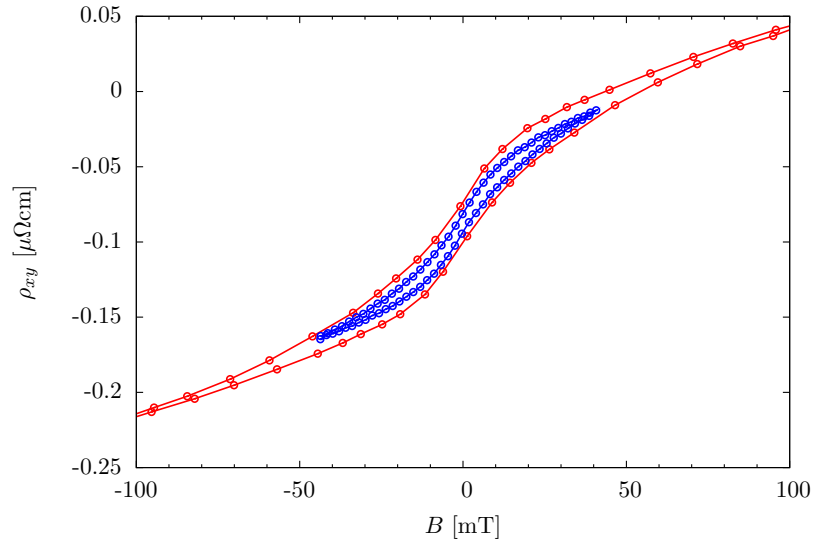
Figure 4.47: Comparison of Hall resistance measurements performed with the full field range of ±0.9 T (red) and with reduced range of ±45 mT (blue) at 326 K.

trast within the otherwise homogeneous β-MnAs. Using SQUID magnetometry they determined that hysteresis loops for in-plane magnetization show zero remanence at

temperatures above 323 K. In contrast, for out-of-plane magnetization, they found a small remanence persisting up to 328 K, at which point they terminated their measurements (see Fig. 4.48).
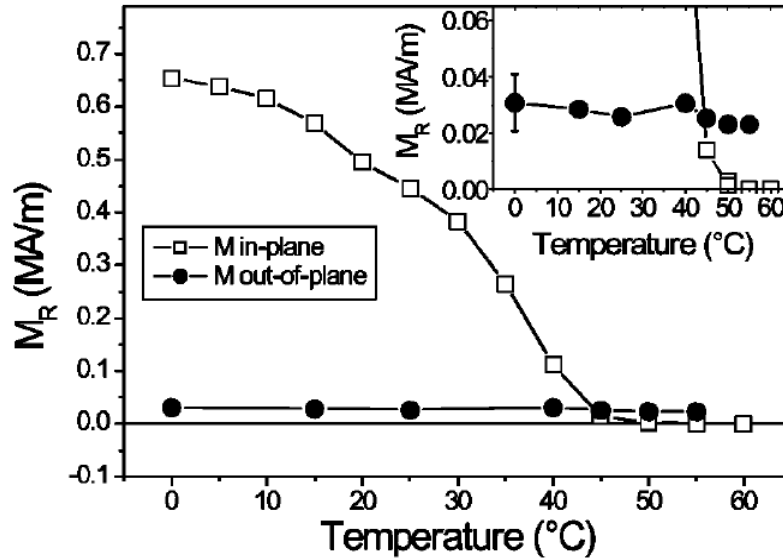
Figure 4.48: Remanence of in- and out-of-plane components of magnetization measured using SQUID magnetometry, taken from Ney et al. [150]. Reprinted with kind permission of the American Institute of Physics.

The weak temperature dependence, together with the isolated contrast in MFM measurements, lead them to speculate that both may be due to "Mn-rich inclusions". The inclusions were apparently identified using X-ray diffraction as Mn_2As (which is antiferromagnetic [26, 27]) and Mn_3As [151].

In our data, we do not find this temperature independence and it would be somewhat hard to explain the almost sample-independent strength of the anomalous effect with such a random process.

4.4.2 Discussion

Non-linear Hall resistance is frequently observed for samples with multi-band conduction. However, these non-linearities appear at field magnitudes on the order of the inverse of the carrier mobility. Commonly, non-linear Hall effect is also observed due to carrier localization effects at low temperatures and high magnetic fields. In our case, the anomalous Hall effect may be a more natural explanation for the observed non-linearity in the Hall effect. However, assuming a paramagnetic β-phase, one would expect a strictly linear anomalous Hall effect at least for small fields (see Section 2.3.1).

Therefore, we have to conclude that a residual magnetic scattering exists within the β-phase. In principle, inclusions of a second phase formed during crystal growth could be responsible for this contribution. On the other hand, the effect is of the same magnitude for several samples, making a random process seem unlikely. If all other explanations fail, we are left to conclude that the anomalous contribution is due to a residual magnetic order in β-MnAs itself. We can only speculate what the nature of this magnetic order is. In any case, the temperature-dependence of the AHE above 330 K (Figs. 4.44 and 4.45) shows no resemblance to the anomalous susceptibility in the bulk (Fig. 2.4). Therefore, it appears clear that the magnetic state of the β-phase in the thin-film is different from that of the bulk.

In this context, it is useful to recall several other experiments that have hinted at the possibility of antiferromagnetic order in thin-films of MnAs:

- Chun et al. [152] have observed an exchange-biasing effect in MnAs samples in the phase-coexistence regime. This implies the presence of an antiferromagnetic component, which could be β-MnAs.

- Using X-ray magnetic circular (XMCD) and X-ray magnetic linear dichroism

(XMLD), Bauer et al. [153] have investigated the magnetic structure in the phase coexistence regime. The XMCD signal is proportional to the net magnetic moment and thus sensitive to ferromagnetic ordering. On the other hand XMLD is sensitive to the axial alignment of spins [77] and can thus provide antiferromagnetic contrast. They found that an antiferromagnetic signal was detected in those areas of the sample where XMCD indicated no ferromagnetic ordering, i.e. inside the β-phase stripes. Interestingly, the intensity of the antiferromagnetic signal decreased with the disappearance of α-stripes, although "some very weak stripe contrast can be seen at much higher temperatures (about 100°C)" [153].

- The negative slope of resistance in the β-phase can also be explained under the assumption of antiferromagnetic ordering (see Chapter 5).

In summary, it appears clear that at least in thin-films the β-phase of MnAs is not simply paramagnetic, but shows a degree of magnetic order. Considerable evidence is suggestive of an antiferromagnetic state. At present, a comprehensive understanding of the non-linear Hall effect data cannot be established.

4.5 Conclusions

We have shown that MnAs can be etched quite readily using a BCl_3 based ICP etch with a conventional photoresist mask, making involved processing using intermediate metal mask layers unnecessary. This enables us to reliably measure the electric properties of *pristine* MnAs thin-films. As expected for a hexagonal material, the resistivity of MnAs is anisotropic between the $[11\bar{2}0]$ and $[0001]$ directions. The anisotropy is a function of temperature. In the pure α-phase, resistivity follows a T^2 behavior, characteristic for electron-electron scattering. In the pure β-phase,

resistivity is only a weak function of temperature. The slope $d\rho/dT$ is negative, a possible indication of antiferromagnetic ordering. Inside the phase-coexistence regime, the temperature dependence of resistivity reflects the periodic arrangement of alternating α- and β-MnAs. From the resistivity measurements, one can accurately determine the relative phase fractions — in good agreement with the phase fractions determined by X-ray diffraction measurements. A clear hysteresis is observed in the α- to β-transition, with the details depending on sample thickness and growth conditions. For all samples, however, we find significant structure in the hysteresis, with three distinct maxima. Comparison with temperature-dependent AFM images leads us to speculate that these maxima are related to the ordering processes in the array of α- and β-phase stripes.

Below 320 K, Hall resistance in MnAs thin-films is dominated by the anomalous Hall effect. Magnetic hysteresis observed in the coexistence regime provides direct evidence of stable out-of-plane magnetic domains (and confirms earlier MFM interpretations). This can be understood by considering the balance between magnetocrystalline anisotropy and shape anisotropy as the α-phase breaks up into separated stripes with increasing temperature. Remarkably, an anomalous contribution to the Hall resistivity is still observed in the pure β-phase. We take this to indicate residual magnetic ordering.

Chapter 5

The β- to γ-Transition

In the bulk, the β- to γ-transition is observed at about 398 K. Considering the influence that strain has on the α- to β-transition, it seems reasonable to assume that in a thin-film the β- to γ-transition temperature may also be modified. While the α- to β-transition is relatively easily studied due to its first order nature, the β- to γ-transition is much harder to detect experimentally and has thus not received any significant attention in the literature. We use a combination of electrical measurements, X-ray diffraction and reflectance difference spectroscopy (RDS) in an attempt to fill this gap.

5.1   Electrical Measurements

While $\delta\rho_{xx}/\delta T$ is generally found to be negative for the β-phase, it changes sign again in a temperature range around 360 to 375 K, and remains positive until thermally-activated parasitic conductivity from the substrate starts dominating (above 415 K). The change in slope has been assumed to mark the β- to γ-transition [128, 154]. If the the β-phase is indeed antiferromagnetic, the incommensurate magnetic and

crystallographic lattice may lead to the appearance of superzone gaps [155, 156] in the Fermi surface, resulting in a reduction in the number of carriers. With increasing temperature, the gap would shrink up to the Néel temperature and hence resistivity would also decrease, as is observed. This effect should have a directional dependence which the Hall-bar geometry allows us to study. Through careful measurements we show that the resistivity minimum occurs at different temperatures for the two in-plane crystallographic directions, supporting the idea of an antiferromagnetically ordered state in the β-phase.

5.1.1   Resistivity Minimum

The procedure for the electrical measurements was already detailed in Section 4.3. Here we show the resistivity measurements in the high temperature regime (β- and γ-phase), where the temperature dependence is extremely weak compared to that of the low temperature α-phase.

Figure 5.1 shows typical resistivity data, measured simultaneously for both crystallographic in-plane directions. The step changes in the measured data are due to the resolution limit of the lock-in amplifier. The same general behavior was observed for all samples: Resistivities for both crystalline directions show well defined minima in the temperature range between 360 and 385 K. Above the minimum, the slope remains positive until parasitic substrate conductivity effects set in above ≈ 415 K. In order to accurately determine the location of the resistivity minima, 5th order polynomials were fit to the data, shown as the solid lines in Fig. 5.1. Separate fits were performed for heating and cooling, which showed only a very small temperature hysteresis (≈ 0.2 K). The results are summarized in Table 5.4 at the end of this chapter.

Notably, we consistently find the minimum at a lower temperature for the [0001]

direction.
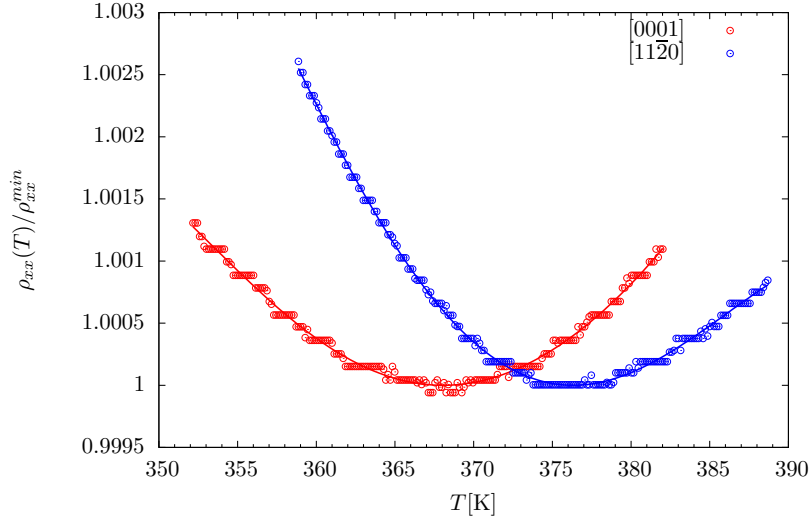
Figure 5.1: Resistivity for sample TE600 measured during heating along the two in-plane crystalline directions. To facilitate comparison, each dataset was normalized to the resistivity at the minimum. Solid lines are 5th order polynomial fits.

In Fig. 5.2, the normalized temperature coefficients $\frac{d\rho_{xx}/dT}{\rho_{xx}(340\text{ K})}$ are shown for the two crystallographic directions and the β- and γ-phase. A systematic difference is found for both phases between the two directions. The magnitude of the slope is larger along the $[11\bar{2}0]$ direction for the β-phase, while the inverse is true for the γ-phase. Clearly, this points to a directionally dependent change in the transport at the phase transition, supporting the idea of an antiferromagnetic superzone gap for the β-phase.

5.1.2   Extrapolation of the α-Phase Resistivity

It was pointed out by Takagaki et al. [128], that the extrapolated α-phase resistivity intersects the measured high temperature resistivity somewhere near the resistivity minimum encountered for the β- to γ-transition, see Fig. 4.18.
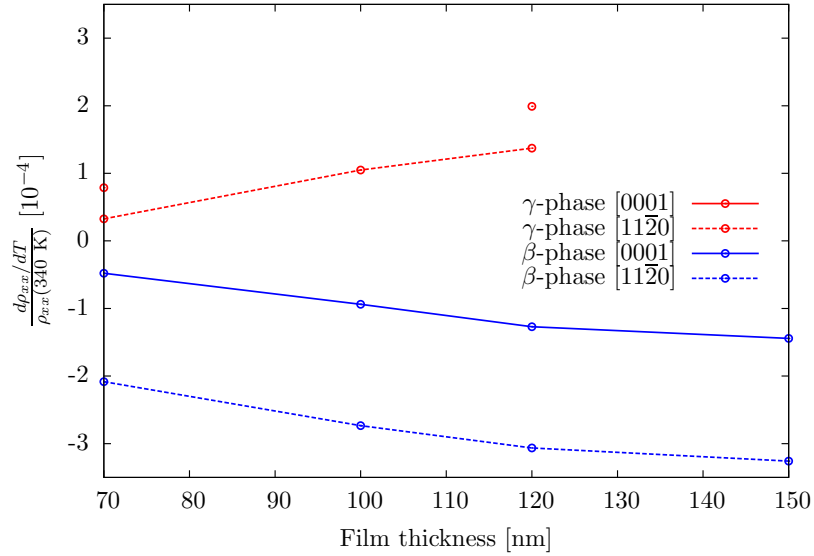
Figure 5.2: Normalized temperature coefficient of the resistivities in the β- and γ-phase for the two in-plane directions.

In Table 5.1 we tabulate the temperatures for this intersection for our samples. The numbers obtained for the two in-plane directions are in close agreement, with the values for the $[11\bar{2}0]$ direction about 2 K lower than for [0001]. Overall, though, the temperatures obtained are about 10 K lower than the ones for the resistivity minimum in the [0001] direction. This does, however, not contradict the interpretation given by Takagaki et al. [128], namely that the resistivity of MnAs would show a continuous variation at a hypothetical α- to γ-transition if it were not for the β-phase.

	$[11\bar{2}0]$	$[0001]$
TE580	355.2 K	356.7 K
TE581	354.0 K	357.2 K
TE600	360.1 K	
TE578	360.3 K	362.5 K
TE579	359.2 K	360.9 K

Table 5.1: Intersection temperatures of the quadratically extrapolated α-phase resistance with the measured high temperature resistance.

5.2 Structural Characterization by X-Ray Diffraction

X-ray diffraction experiments offer the most direct route to determine structural changes of the MnAs films. As seen in Section 4.2, variations in the b_o-lattice parameter are directly accessible by monitoring the $[1\bar{1}00]$ reflection. On the other hand, the a and c in-plane lattice parameters are more difficult to determine. Jenichen et al. [157] used synchrotron radiation for grazing incidence diffraction to determine in-plane lattice parameters during growth and found that at a temperature of 200°C, both a and c lattice constants were very close to the bulk values. At lower temperatures, on the other hand, the epitaxial relationship between the MnAs layer and the GaAs substrate is fixed, and therefore both a and c necessarily follow the thermal expansion of GaAs.

An overview of the reflections accessible by X-ray diffraction without grazing incidence equipment is shown in Table 5.2.

Only the out-of-plane $b_o = 2d_{(020)}$ lattice constant is directly accessible, with the sample surface normal in the scattering plane. The c_o lattice constant can in principle be determined by an additional measurement of the (021) reflection, where

$(hkil)_h$	$1/d^2_{hkil}$	Ψ_h	$(hkl)_o$	$1/d^2_{hkl}$	Ψ_o	Φ
$(1\bar{1}00)$	$\frac{4}{3a_h^2}$	$0°$	(020)	$\frac{4}{b_o^2}$	$0°$	any
$(\bar{1}101)$	$\frac{4}{3a_h^2} + \frac{1}{c_h^2}$	$\arctan \frac{\sqrt{3}a_h}{2c_h} \approx 29.4°$	(021)	$\frac{4}{b_o^2} + \frac{1}{c_o^2}$	$\arctan \frac{b_o}{2c_o} \approx 29.4°$	$0°$
$(2\bar{1}10)$	$\frac{4}{a_h^2}$	$\arctan \frac{1}{\sqrt{3}} = 30°$	(130)	$\frac{1}{a_o^2} + \frac{9}{b_o^2}$	$\arctan \frac{b_o}{3a_o} \approx 30°$	$90°$

Table 5.2: Comparison of hexagonal and orthorhombic reflections, which are accessible by X-ray diffraction. Ψ is the angle between surface normal and scattering plane. Φ is the angle of rotation around the surface normal, with $\Phi = 0°$ defined as $[0001]$ perpendicular to the scattering plane.

the surface normal is under an angle of $\approx 29.4°$:

$$\frac{1}{c_o^2} = \frac{1}{d^2_{(021)}} - \frac{1}{d^2_{(020)}} = \frac{1}{d^2_{(021)}} - \frac{4}{b_o^2}. \tag{5.1}$$

In the same manner, the a_o lattice constant is accessible by recording the (130) reflection:

$$\frac{1}{a_o^2} = \frac{1}{d^2_{(130)}} - \frac{9}{b_o^2}. \tag{5.2}$$

Here, the sample has to be rotated by $90°$ to bring the c-axis into the scattering plane.

5.2.1 Setup

Since the powder diffractometer was not equipped with a (Ψ, Φ) sample goniometer, a special stage had to be constructed.

For the Ψ axis, a manual $\pm 35°$ goniometer with a radius of 6.4 cm was used. Rotation around Φ was accomplished through a simple optical rotation stage. On top of this, a copper heat sink with embedded Nichrome wire heater was mounted as the sample stage. A silicon diode was indium mounted on top for temperature
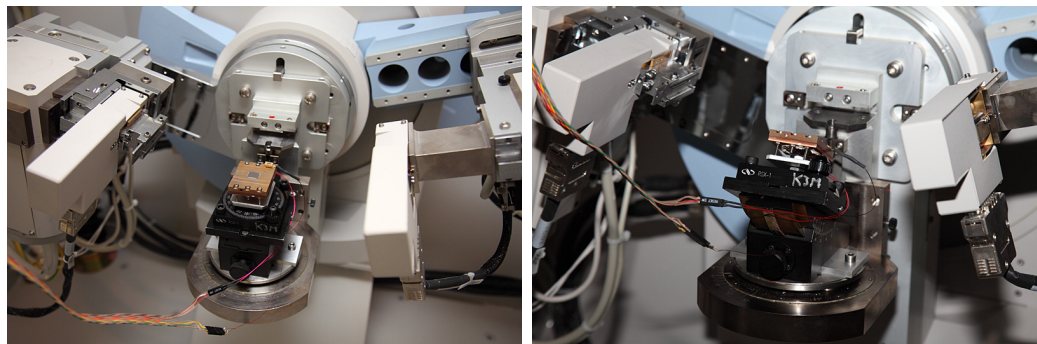
Figure 5.3: Custom heated goniometer stage in Panalytical powder diffractometer at $\Psi = 0°$ (left) and $\Psi = 30°$ (right).

control using a Lakeshore 331 temperature controller. The sample was mounted and heat-sunk using silver paint. Typical control stability was 10 mK. Two photographs of the setup mounted in the diffractometer is shown in Fig. 5.3.

5.2.2 Determination of Lattice Constants

For precise determination of the lattice constant it is necessary to obtain accurate measurements of the Bragg angle Θ. Unfortunately, in the actual experiment peak positions can experience significant instrumental shifts due to shift of the sample height, shift of the goniometer zero point, and axial divergence of the beam.

Sample Height

For a diffractometer of radius R, a sample height misalignment b leads to a shift of the reflection by [122]

$$\Delta(2\Theta) = -2\frac{b}{R}\cos\Theta. \tag{5.3}$$

The sample height for this diffractometer can be measured using a micrometer

and was adjusted at room temperature to a setting predetermined by the instrument owner. Depending on the accuracy of this alignment, this may introduce a constant height shift. Additionally, thermal expansion of the copper stage may cause small changes in the sample height alignment during the measurement.

For temperature change ΔT, the error in lattice constant therefore is

$$\frac{\Delta a}{a} \approx \frac{\Delta(2\Theta)}{2\Theta} = -\frac{\alpha_{Cu} t_{Cu}}{R \cdot \Theta \cos \Theta} \Delta T \tag{5.4}$$

With the thermal expansion coefficient for Copper of $\alpha_{Cu} = 17 \cdot 10^{-6}$ K^{-1} and a 7 mm thick sample stage, one obtains a positional shift of about 12 μm per 100 K. Similar numbers were reported for a commercially constructed X-ray heating stage [158]. On a diffractometer with $R = 24$ cm, this corresponds to a relative error of $2.5 \cdot 10^{-6}/K$ for the (020) reflection, i.e. on the order of the GaAs thermal expansion coefficient.

Goniometer Zero Point

The absolute angle of the reflections is also shifted by any misalignment of the goniometer zero-point, as well as sample tilts introduced by the sample stage. Sample tilt may also vary versus temperature due torsional movements of the sample plate. This error is simply additive:

$$\Delta(2\Theta) = 2\Theta_0. \tag{5.5}$$

Axial Divergence

In our experiment axial beam divergence was limited with two Soller slits to $\delta_{Sol} = 0.04$ rad $= 2.3°$. For this case, the peak shift is given by [122]

$$\Delta(2\Theta) = -2\frac{\delta_{Sol}^2}{6} \cot 2\Theta. \tag{5.6}$$

Since this shift is temperature independent and parameter-free, it can be trivially corrected for before any of the other corrections are considered.

In summary, we obtain the following expression for the observed peak position:

$$\Theta^{obs} = \Theta^{Bragg} - \Theta_0 - \frac{b}{R}\cos\Theta^{obs} - \frac{\delta_{Sol}^2}{6}\cot 2\Theta. \tag{5.7}$$

Correction Procedures

Depending on the assumptions one is willing to make about the sample, different approaches can be chosen to deal with the instrumental peak shift.

One typical correction procedure for dealing with the zero-shift of the goniometer is the so-called "reflection-pair" method developed by Dong et al. [159]. Here the height misalignment is ignored, and only the Θ_0 offset is taken into account.

If one measures a pair of reflections (hkl) and $(h'k'l')$ with $h' = mh$, $k' = mk$, and $l' = ml$, the zero shift can be calculated as

$$\tan\Theta_0 = \frac{m\sin\Theta_{hkl}^{obs} - \sin\Theta_{h'k'l'}^{obs}}{\cos\Theta_{h'k'l'}^{obs} - m\cos\Theta_{hkl}^{obs}}. \tag{5.8}$$

This procedure was followed using the GaAs (002) and (004) reflections as the reflection pair. Almost identical offsets were found from the pair of MnAs (020) and (060). The calculated GaAs lattice constant was very close to literature values, and the thermal expansion coefficient of GaAs was well reproduced.

If one wants to take in account both sample shift and goniometer zero shift, one needs to use additional constraints. One possibility is to take the lattice constant of GaAs as a given and use the (002), (004) pair of reflections to determine both the zero point shift and the sample height misalignment:

$$b = R\frac{(\Theta_1^{Bragg} - \Theta_1^{obs}) - (\Theta_2^{Bragg} - \Theta_2^{obs})}{\cos\Theta_1^{obs} - \cos\Theta_2^{obs}} \tag{5.9}$$

and

$$\Theta_0 = \Theta_1^{Bragg} - \Theta_1^{obs} - b/R \cos \Theta_1^{obs}. \tag{5.10}$$

In principle, the offsets can also be deduced without any assumptions about the absolute value of the lattice constants by using MnAs (020) and (060) as a an additional "reflection-pair". The resulting system of two non-linear equations was solved numerically using GNU Octave. We found, however, that the smaller accuracy of peak determination for the weaker MnAs reflections together with the near-degeneracy of the equation system led to large random fluctuations in the computed offsets.

5.2.3   Results

A plot of the three reflections for two different temperatures is shown in Fig. 5.4. The (021) and (130) reflections are significantly broader than the (020) due to geometrical effects.

Separate temperature scans were taken for the three reflections, each with fixed Ψ and Φ. All data were corrected for Cu $K_{\alpha2}$ radiation as described in Section 4.2.1. Peak positions were determined by center-of-mass.

A plot of the out-of-plane lattice constant b_{oh}, determined using two of the correction procedures above, is shown in Fig. 5.5. While a small but significant difference is found for the absolute values of the lattice constant, the temperature dependence is almost identical. The thin-film lattice constant is smaller than the bulk, as would be expected for a film under biaxial in-plane tensile strain. A clear change in slope is found at 372 K. Below this temperature, the thermal expansion coefficient is $7.22 \cdot 10^{-5}$ K^{-1}, above $3.51 \cdot 10^{-5}$ K^{-1}.
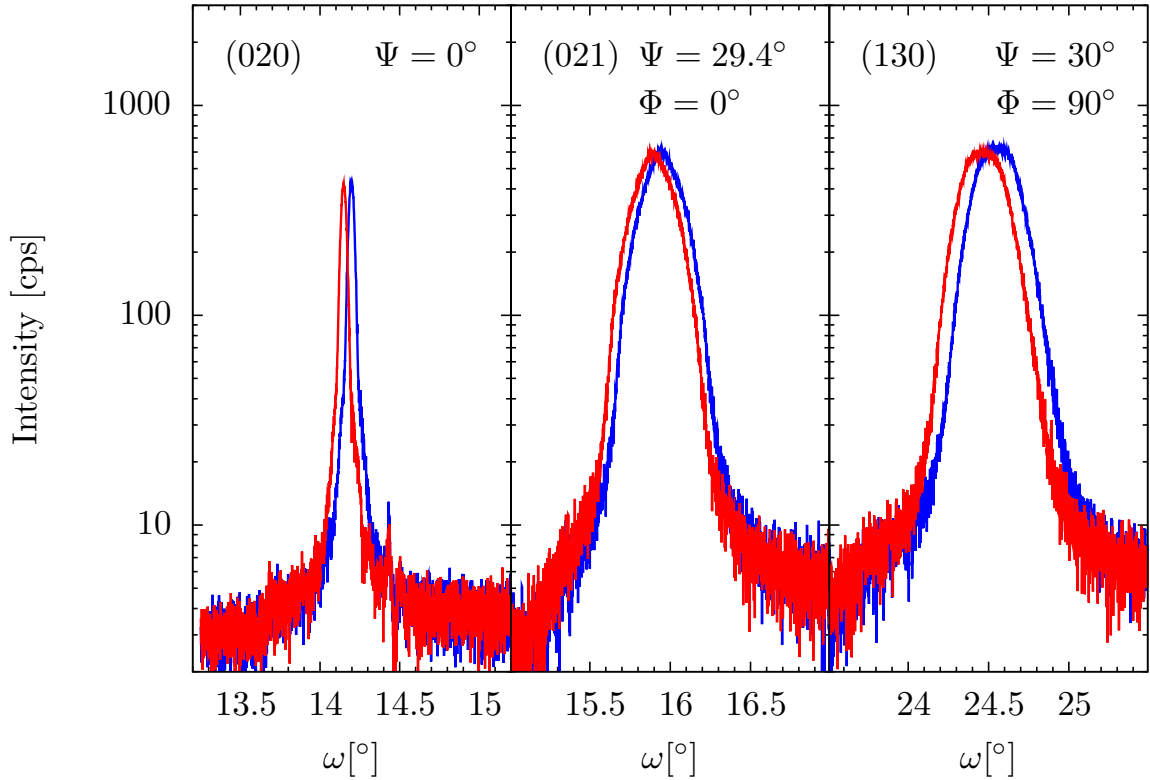
Figure 5.4: X-ray diffraction scans for the MnAs (020), (021), and (130) reflections, after Cu $K_{\alpha2}$ removal. Red curves are at 340 K, blue curves at 420 K. The ω ranges for all plots are 2°.

Under the assumption that the out-of-plane stress σ_{yy} is zero (the film is free to expand in the growth direction), one can derive from the stress-strain relation (equation 2.5) the following expression for the out-of-plane strain component ε_{yy}:

$$\varepsilon_{yy} = -\frac{c_{12}\varepsilon_{xx} + c_{13}\varepsilon_{zz}}{c_{11}} = -\frac{8.7\varepsilon_{xx} + 10.7\varepsilon_{zz}}{41.0} \tag{5.11}$$

For the in-plane lattice strains ε_{xx} and ε_{zz} we may use the temperature dependence calculated in Section 2.2.1. A plot comparing the results of this calculation with the strain calculated from the measured b_{oh} and bulk lattice constants is shown in Fig. 5.6.

The (021) and (130) reflections can also be used to check the orientation of MnAs
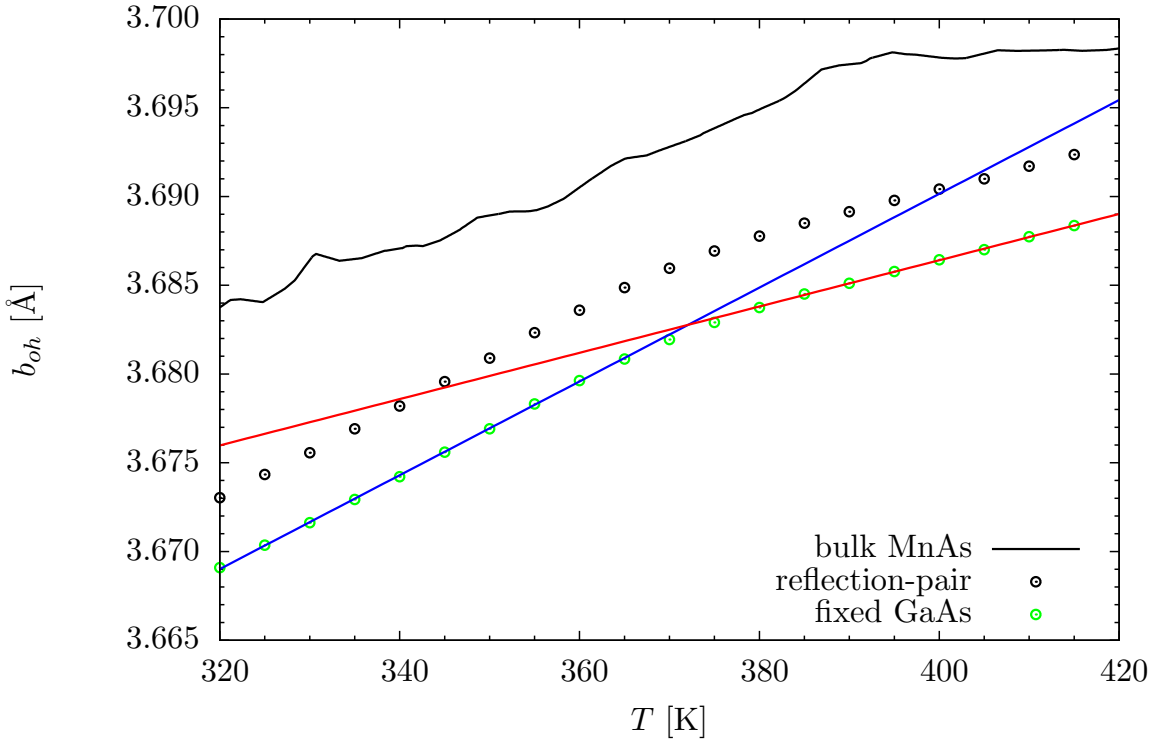
Figure 5.5: Lattice constant $b_{oh} = b_o/\sqrt{3}$ versus temperature for sample TE600, corrected using the "reflection-pair" method (black circles), or by matching to the literature GaAs lattice constant (green circles). For reference, the reported bulk lattice constant is also shown (black curve). The straight lines are linear fits to the low (blue, ≤ 365 K) and high temperature (red, ≥ 375 K) lattice constant. They intersect at 372.2 K.

with respect to the substrate: If MnAs is only present in the A_0 orientation, the (021) reflection should only be observed with the GaAs [110] direction in the diffraction plane. Similarly, the (130) reflection should only be observed for GaAs [1$\bar{1}$0] in the diffraction plane. The opposite would hold for B_0 oriented MnAs. Figure 5.7 shows scans of the MnAs (021) and (130) reflections for different sample azimuths. The results show that MnAs is exclusively A_0 oriented in this sample. This further confirms the results from the resistivity anisotropy (see Section 4.3.3) and demonstrates the good quality of our samples.
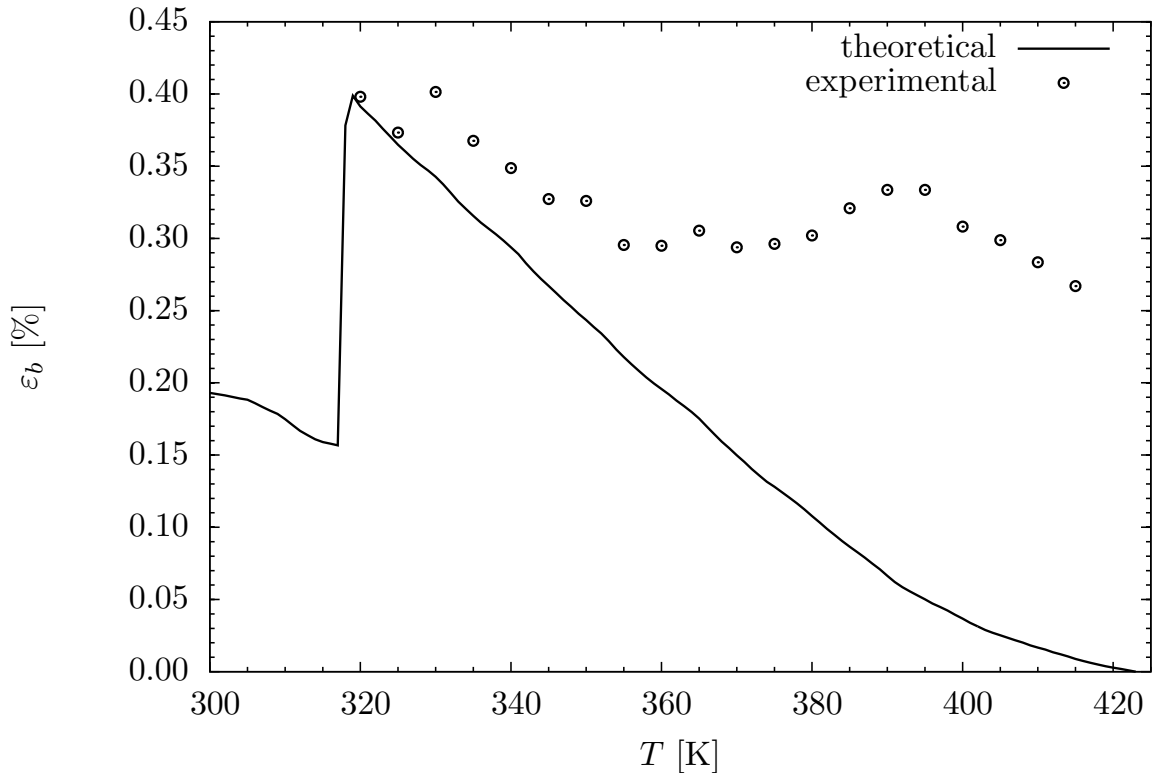
Figure 5.6: Out-of-plane strain versus temperature. The solid line represents strain calculated using the assumed in-plane strains and the elastic constants from Chapter 2. The data points represent strain calculated using the experimental thin-film and bulk lattice constants.

5.3   Reflectance Difference Spectroscopy

Reflectance difference spectroscopy (RDS), also known as reflectance anisotropy spectroscopy (RAS) [1], is a technique that has been used extensively to study the evolution of clean surfaces, usually in ultra-high vacuum (UHV). Polarized light is incident almost perpendicular to the sample surface, and the polarization state of the reflected light is measured. Most applications of RDS so far have focused on materials with

---

[1]Although the term reflectance anisotropy spectroscopy is more explicit about the origin of the effect, namely the anisotropy of the dielectric constant, we will follow the trend in the literature by using the term reflectance difference spectroscopy.
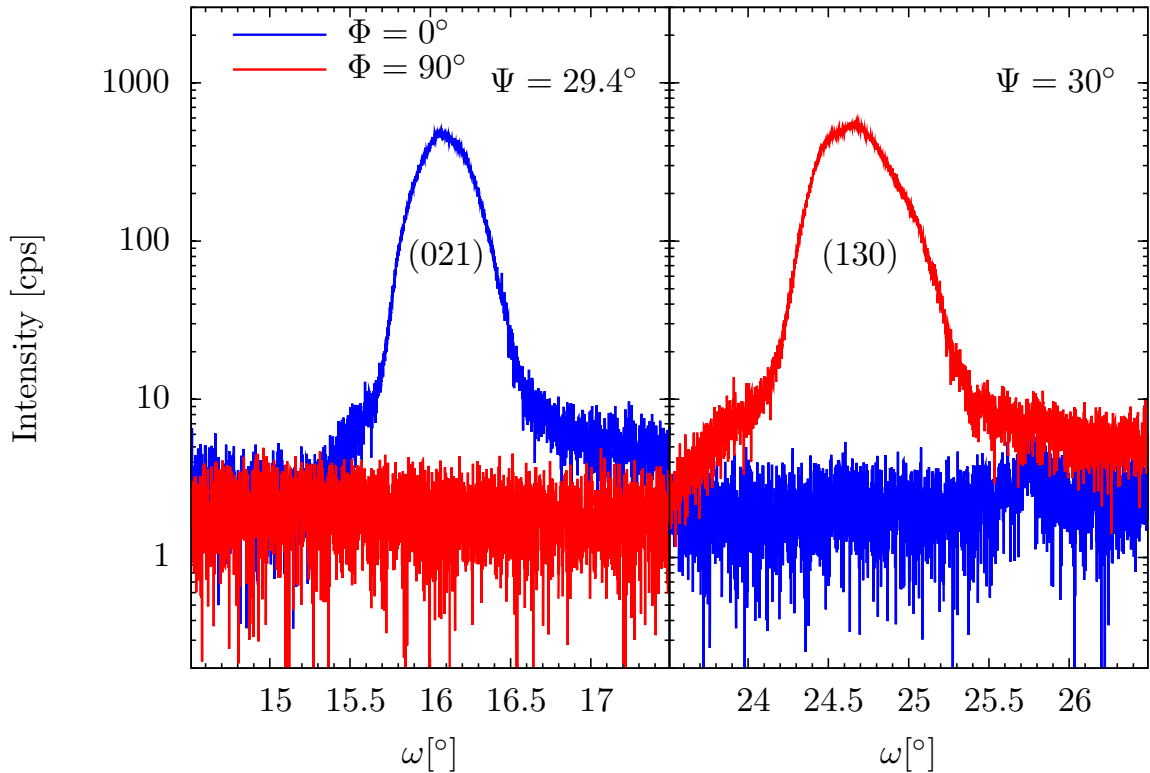
Figure 5.7: X-ray diffraction scans of the MnAs (021) and (130) reflections for two different sample azimuths: the (021) reflection is only detectable for $\Phi = 0°$ (GaAs [110] in scattering plane), the (130) reflection only for $\Phi = 90°$ (GaAs [1$\bar{1}$0] in scattering plane). Sample: TE600.

cubic crystalline symmetry, where the bulk is isotropic and all anisotropy therefore has to originate from the surface. For this case, RDS has been proven to be extremely useful for monitoring surface reconstructions during epitaxial growth, particularly for MOCVD, where other techniques such as RHEED are not available. A recent review of common applications of the technique is given by Weightman et al. [160].

If the material under investigation is not of cubic symmetry, then the reflectance difference can also be due to a bulk effect.

The reflectance difference signal is defined as

$$\frac{\Delta r}{r} \equiv \frac{r_a - r_b}{\frac{1}{2}(r_a + r_b)} \equiv Re\left(\frac{\Delta r}{r}\right) + \imath Im\left(\frac{\Delta r}{r}\right), \tag{5.12}$$

with the amplitude reflectivities r_a and r_b along the crystallographic axes.

Typical reflectance differences from surface reconstructions are on the order of 10^{-3} (= one "RDS unit") [161], see for example the spectra of the GaAs surface reconstructions (Fig. 5.8).

5.3.1 Setup

The setup by Aspnes [163], Fig. 5.9, makes use of a photoelastic modulator to obtain very high sensitivity in the polarization rotation and has become the standard in the field.

The photoelastic modulator consists of a quartz bar, modulated by a piezoelectric driver at a frequency of about 50 kHz. The retardation is $\delta = \delta_c \sin \omega t$.

The resulting signal intensity at the detector can be derived using either Jones or Mueller matrix calculations. The end result — assuming precise alignment of all optical components and neglecting higher order terms — is [163, 164, 165]:

$$\frac{\Delta I}{I_0} = 1 + J_0(\delta_c)Re\left(\frac{\Delta r}{r}\right) - 2Im\left(\frac{\Delta r}{r}\right)J_1(\delta_c)\sin \omega t + 2Re\left(\frac{\Delta r}{r}\right)J_2(\delta_c)\cos 2\omega t \tag{5.13}$$

The DC term $I_0(1 + J_0(\delta_c)Re\left(\frac{\Delta r}{r}\right))$ can be measured by a voltmeter (V_{DC}), while the AC terms at ω and 2ω can be detected with a lock-in amplifier. Proper normalization then yields the real and imaginary parts of $\frac{\Delta r}{r}$:
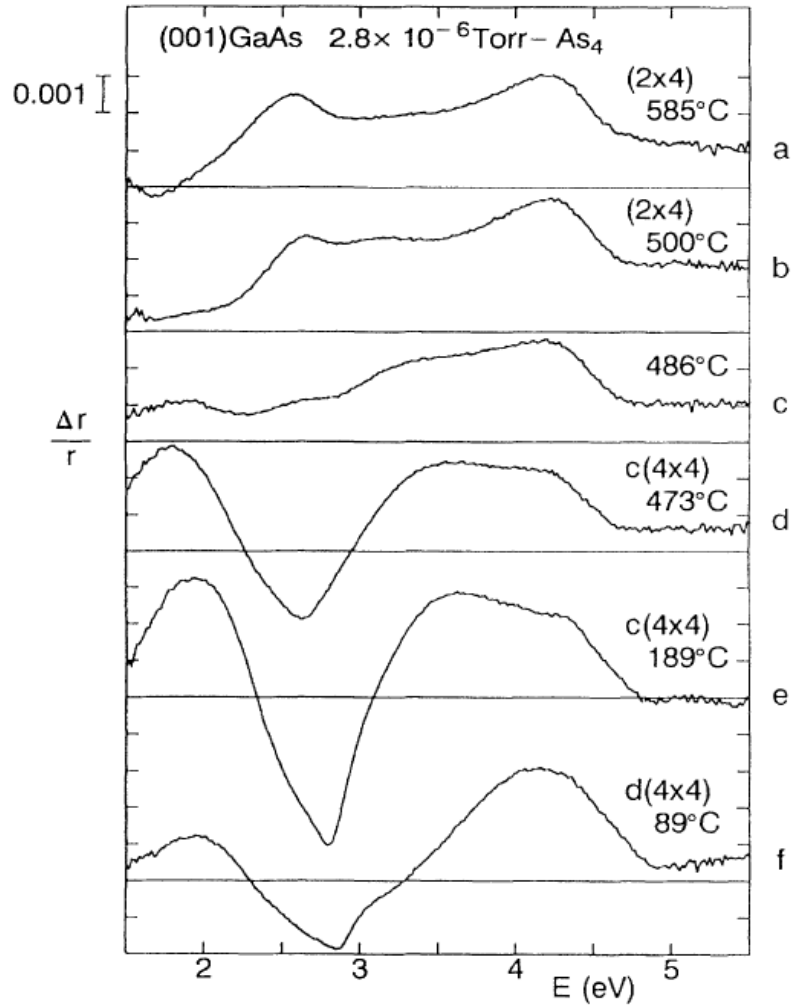
Figure 5.8: Temperature evolution of RDS spectra of the GaAs (001) surface. Taken from Kamiya et al. [162]. (Copyright (1992) by The American Physical Society.)

$$Re\left(\frac{\Delta r}{r}\right) = \frac{V_{2\omega}}{2J_2(\delta_c) \cdot V_{DC}} \tag{5.14}$$

$$Im\left(\frac{\Delta r}{r}\right) = \frac{-V_{1\omega}}{2J_1(\delta_c) \cdot V_{DC}} \tag{5.15}$$

As the lock-in measures root-mean-square (RMS) values $R_{1\omega}$ and $R_{2\omega}$, these val-
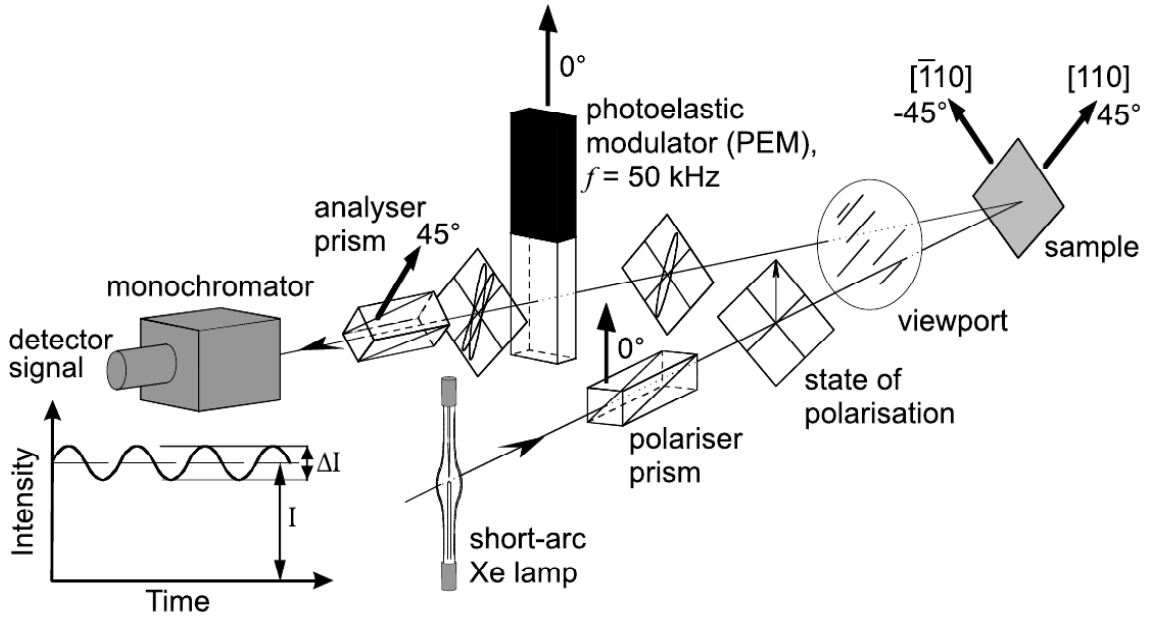
Figure 5.9: RDS setup, after Aspnes. From Kaspari's dissertation [161]. Linearly polarized light is incident upon the sample at near perpendicular incidence. The different reflectivities for the two crystalline directions lead to elliptically polarized light in the reflected beam. A photoelastic modulator and second polarizer are used to analyze the polarization state of the reflected light.

ues have to be multiplied by $\sqrt{2}$ to obtain $V_{1\omega}$ and $V_{2\omega}$.

The peak retardance can be chosen to maximize either $Im\left(\frac{\Delta r}{r}\right)$ or $Re\left(\frac{\Delta r}{r}\right)$ by maximizing $J_1(\delta_c)$ or $J_2(\delta_c)$ respectively, see Fig. 5.10. The usual choice is $\delta_c = \pi$, where J_2 is close to its maximum (see Table 5.3). However, the DC term then contains a contribution of $Re\left(\frac{\Delta r}{r}\right)$, which may only be neglected for $Re\left(\frac{\Delta r}{r}\right) \ll 1$. In our case, where $Re\left(\frac{\Delta r}{r}\right)$ approaches 3%, a better choice is to set $\delta_c = 0.76548\pi$, where $J_0(\delta_c) = 0$.

For our experiments, the sample was mounted on a Joule-Thomson cold stage inside a MMR dewar with optical access through a window. The sample space was evacuated using a turbo pump, and final pressures around $3.4 \cdot 10^{-7}$ mbar were achieved. The glass window itself was held in place by the vacuum on a thick Viton
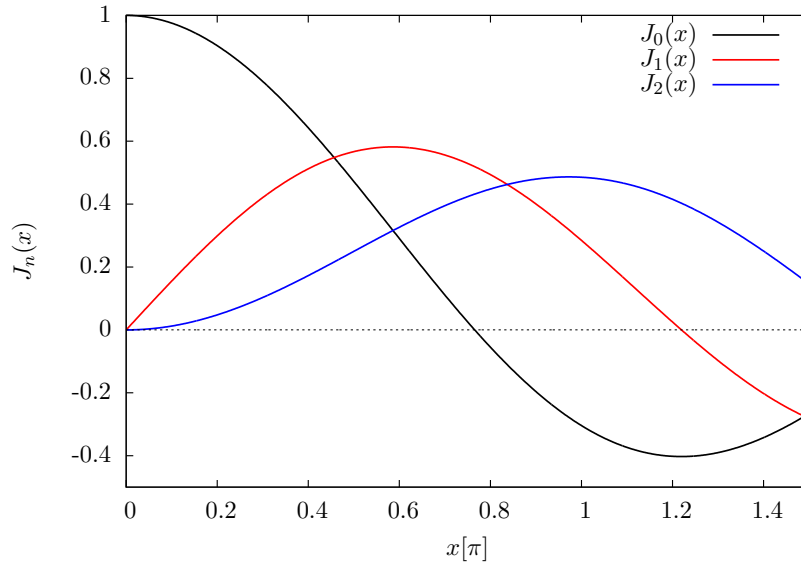
Figure 5.10: Bessel functions of the first kind.

δ_c	$0.586067 \cdot \pi$	$0.76548 \cdot \pi$	$1.0 \cdot \pi$
$J_0(\delta_c)$	0.316028	0	-0.304242
$J_1(\delta_c)$	0.581865	0.519147	0.284615
$J_0(\delta_c)$	0.316028	0.431755	0.485434

Table 5.3: Values of the Bessel function for selected peak retardance settings.

o-ring to minimize strain induced birefringence effects.

As light sources, both a 300 Watt Xe arc-lamp as well as a commercial 407.5 nm (3.04 eV) laser diode were used. The light from the arc-lamp was imaged onto the sample from a small aperture using a lens of $\approx$ 22 cm focal length. A SpectraPro-150 monochromator was used to record spectra with the arc-lamp. Typical spectra of both laser diode and arc-lamp are shown in Fig. 5.11.

While it would be desirable to have a monochromatic incident beam and thus re- duce incident power at the sample, it is more convenient to locate the monochromator
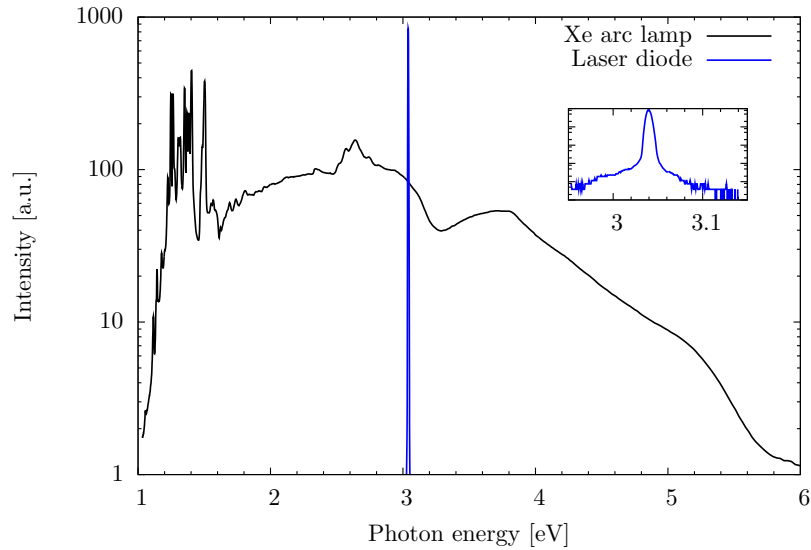
Figure 5.11: Optical spectra of Xe-arc lamp and 407.5 nm laser diode.

directly in front of the detector, eliminating background from stray light. Incident power levels with the Xe arc-lamp was about 3 mW, while very high signal-to-noise ratios could be obtained with incident laser power of less than 1 mW.

For the incident polarizer and analyzer Calcite UV Glan Thompson prism polarizers (Karl Lambrecht Corporation) with an extinction ratio of better than $1 \cdot 10^4$ were used.

It is important that no other optical components are placed inside the polarized beam path, as even minor anisotropies will affect the signal.

Improvement of the Standard Aspnes Setup

One disadvantage of the classical setup by Aspnes is the necessity to measure the DC signal accurately. For spectrally resolved measurements, especially in the UV, this signal may be on the order of just a few microvolts and obscured by voltage offsets and ambient light.

If a third lock-in amplifier is available, or only the real part of the RDS signal is to be measured, a simple solution is to add an optical chopper (in our case $f_{Chopper} \approx$ 345 Hz $\ll$ 50 kHz) to the incident light path and use a lock-in to the detect the chopped "quasi"-DC signal. One problem that arises is that the lock-in will read the RMS amplitude of the signal, which can deviate from an ideal square wave due to the finite size of the beam. Therefore, our measurements were rescaled to fit the data of a measurement taken with the conventional setup. The signal at 2ω can be detected as before, but is reduced by the duty cycle (50%) of the chopper. Since now a large signal exists at $f_{Chopper}$, it is advantageous to remove this signal on the 2ω lock-in using a passive high-pass filter ($f_0^{HP} = \frac{1}{2\pi RC} = 8$ kHz).

This approach was chosen for a subset of our experiments, in particular to resolve small changes in the reflectivity spectra of the β-phase.

5.3.2 Calibration and Alignment

The retardance of the Hinds PEM-90 photoelastic modulator in our setup was calibrated using the oscilloscope method and the 407.5 nm laser diode. A peak retardance of 0.5λ was obtained for a retardance setting of 0.49λ.

The accuracy of alignment of the incident polarization axis with respect to the PEM axis determines the zero offset of $Re\left(\frac{\Delta r}{r}\right)$. A first surface Aluminum mirror was placed into the beam and the incident polarization was carefully adjusted to obtain a minimum in the signal at 2ω.

Figure 5.12 shows RDS temperature scans for sample azimuths of 45°, 90°, and 135°. As expected, for the polarization parallel to one of the principal axes of the sample, the measured signal is almost zero. For the incident polarization at 45° and 135° to the axes, nearly identical results with opposite sign are obtained.
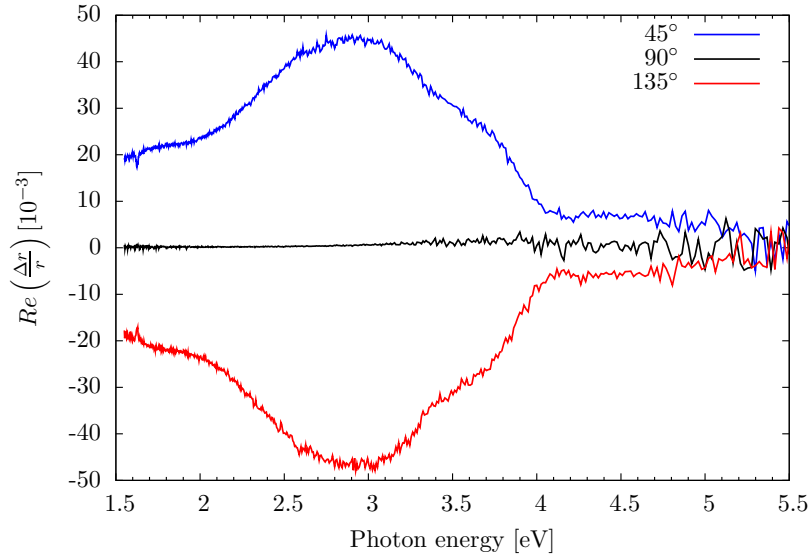
Figure 5.12: RDS spectra (real part) for different azimuths of the sample at 270 K. The sharp spike around 1.65 eV is an artifact from the second harmonic.

5.3.3 The α- to β-Transition

Figure 5.13 shows RDS spectra taken for a range of temperatures. As the sample is cooled into the α-phase, a pronounced feature centered around 2.9 eV develops.

Over the entire temperature range and most of the spectral range, the magnitude of the RDS signal from MnAs is substantially larger (10s of RDS-units) than what is typically observed for surface reconstruction effects (several RDS-units, see Fig. 5.8).

As the temperature is lowered, some saturation effect is observed.

In the β-phase above 330 K, the spectra show no discernible change. Figure 5.14 shows spectra recorded using the chopper-improved technique. It is evident, that in the β-phase there is no change of the feature at 2.9 eV, but a small shift of the entire spectrum is observed.

Figure 5.15 shows laser reflection difference (LRD) temperature scans taken using
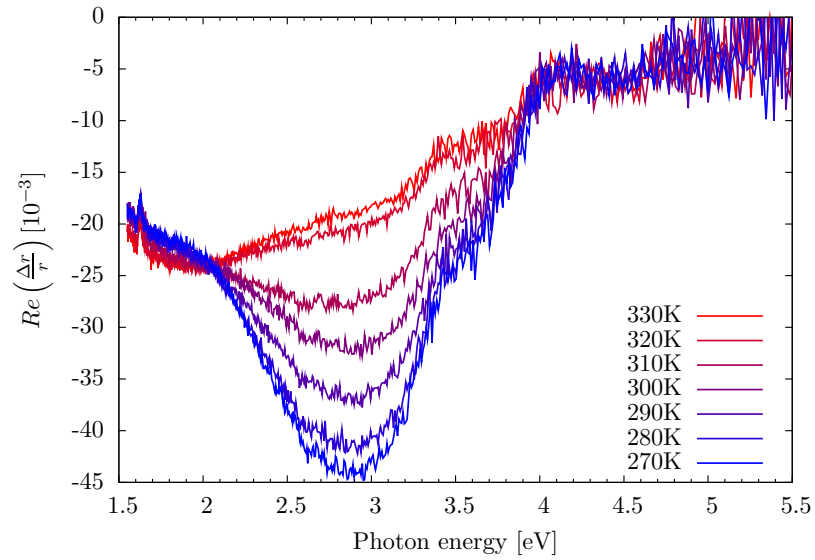
Figure 5.13: RDS spectra (real part) for different temperatures; data taken on sample TE600. The sharp spike around 1.65 eV is an artifact from the second harmonic.

the 408 nm (3.04 eV) laser diode for four different samples.
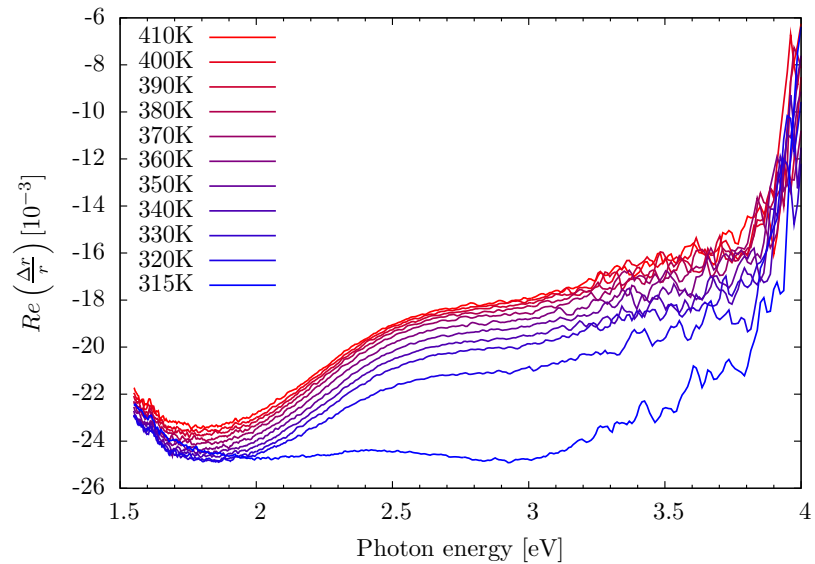
Figure 5.14: RDS spectra (real part) recorded using the chopper-improved setup for different temperatures; data taken on sample TE578.

All curves exhibit a very similar behavior:

- In the β- and γ-phases, above 325 K, the signal is nearly constant — but non-zero — and does not exhibit a hysteresis.

- Below 325 K, the signal rises sharply, but no saturation is observed as the transformation to pure α-phase is completed.

- At low temperatures, a continuous drift of the signal to higher values is observed when the temperature is held constant.

- Drift and possibly hysteresis of the phase transition itself lead to the hysteretic nature of the signal below 325 K.
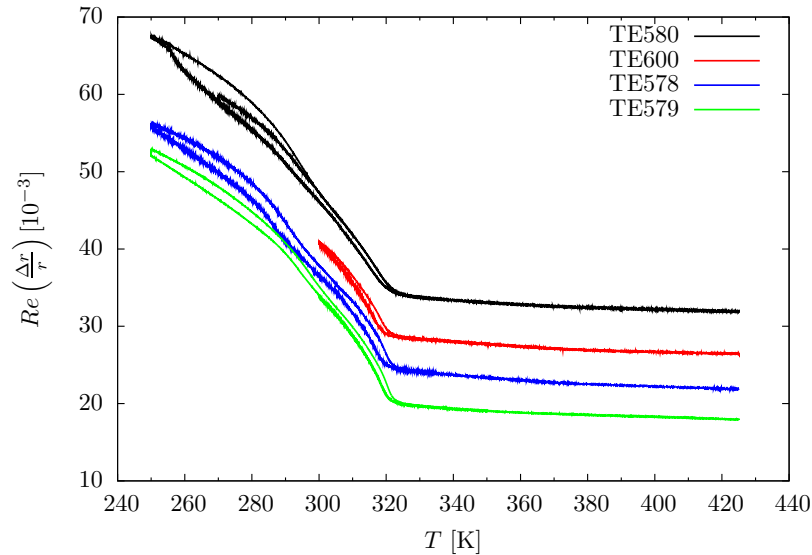
Figure 5.15: Laser reflection difference temperature scans for different samples. For clarity, the curves are offset by $5 \cdot 10^{-3}$.

While it has been claimed by Vidal et al. [166] that the RDS signal may be used to infer the phase fraction, we find that the time-dependent drift encountered in the

relevant temperature range prevents this. Based on the assumption of surface contamination by condensation, several attempts were made reduce the drift. However, neither cleaning of the sample with isopropanol, operation in vacuum after extended "baking" at 350 K, nor operation in a purged dry Nitrogen atmosphere with the window removed seemed to have any substantial impact on the drift. Although we cannot conclusively rule out changes to the surface, we suggest that an intrinsic effect is responsible for the drift. A possible candidate might be the time-dependent alignment of magnetic domains.

5.3.4 Origin of the RDS Feature

Now, we turn our attention towards possible physical mechanisms for the observed reflectance difference.

Surface Effects

Vidal et al. [166] have already speculated on the origin of the RDS signal. One possibility would seem to be the excitation of surface plasmons, facilitated by grating coupling due to the surface corrugation from the array of stripes in the phase-coexistence regime. If this were the case, however, one would expect the signal to be maximal somewhere within the coexistence regime, which is not the case here. The secondary short-period corrugation of the surface along the c-axis could in principle have the same effect. Since this corrugation is not associated with the phase transition, it seems unlikely that this would cause such a sharp increase in the RDS signal as soon as the phase-coexistence regime is entered.

Anisotropic Conductivity

One possible source for anisotropic reflectance may lie in the anisotropic conductivity observed for all phases of MnAs (see Chapter 4).

If the optical coordinate axes x, y, and z coincide with the crystalline axes $\vec{a}$, $\vec{b}$, and $\vec{c}$, the dielectric tensor can be written as

$$\epsilon_r = \begin{pmatrix} \epsilon_{xx} & 0 & 0 \\ 0 & \epsilon_{yy} & 0 \\ 0 & 0 & \epsilon_{zz} \end{pmatrix}. \tag{5.16}$$

.

Hexagonal α- and γ-MnAs are uniaxial, with the ordinary index given by $N_o^2 = \epsilon_{xx} = \epsilon_{yy}$ [167], and the extraordinary index by the permittivity along the optical axis $\vec{c}$ $N_e^2 = \epsilon_{zz}$. Strictly speaking, the orthorhombic β-MnAs has to be treated as biaxial, but we choose to neglect the small distortion from the hexagonal structure and approximate it as uniaxial as well.

Optical measurements of bulk MnAs were already reported by Bärner et al. [168], but due to the polycrystalline nature of their sample anisotropy was not observed. They found a free carrier plasma frequency from d-band electrons of $\hbar\omega_p = 3.03\ eV$ with a scattering time of $\tau = 6.0$ fs. Naturally, this would be an obvious candidate for the observed spectral feature at 2.9 eV.

In the Drude model, the dielectric function is given by

$$\epsilon_D = \epsilon_\infty - \frac{\omega_p^2}{\omega^2 + i\frac{\omega}{\tau}}, \tag{5.17}$$

with $\epsilon_\infty \approx 1$ for metals.

The reflection coefficient is given as

$$r = \frac{N - 1}{N + 1}, \tag{5.18}$$

where $N = \sqrt{\epsilon}$ denotes the complex refractive index.

The calculated RDS signal (assuming a difference of about 12% in the scattering times τ for the two different in-plane crystalline directions) is shown in Fig. 5.16. The shape of the calculated RDS signal is similar to the observed effect (Fig. 5.13), but the magnitude is much smaller.
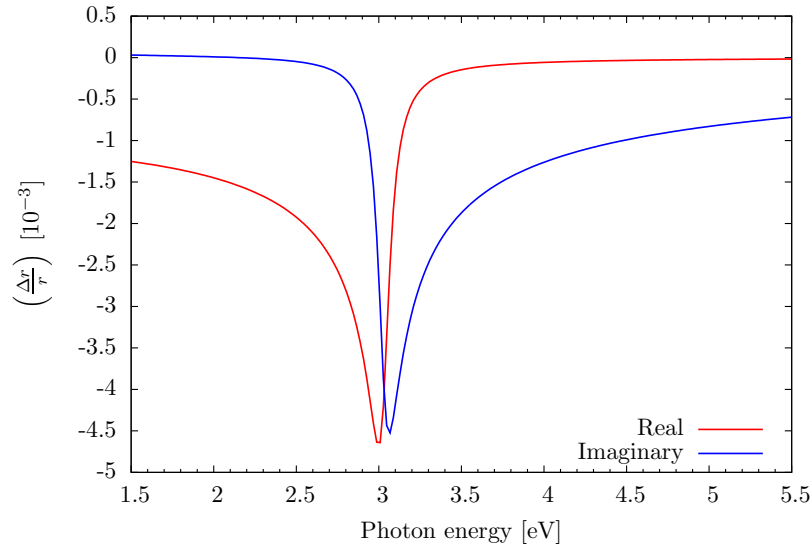
Figure 5.16: RDS signal calculated from Drude model with a 12% difference in scattering times.

The hypothesis can be further evaluated by measuring the reflectance separately for the two in-plane crystalline directions. The setup was modified by removing the PEM, chopping the incident beam for lock-in detection, and inserting a beam pick-up before the polarizer to monitor the total beam intensity. The second polarizer was kept at 45° to ensure constant polarization into the monochromator. The reflectance signal was measured with the incident beam polarized along the two sample directions, and normalized by the reference signal. For each polarization, the measurement was repeated at four temperatures, starting with the $β$-phase at 335 K.

A series of differential reflectance spectra, defined as $R(335\,\text{K}) - R(T_2)$, are shown

in Fig. 5.17. The change in reflectance as the sample is cooled from 335 K to 325 K,
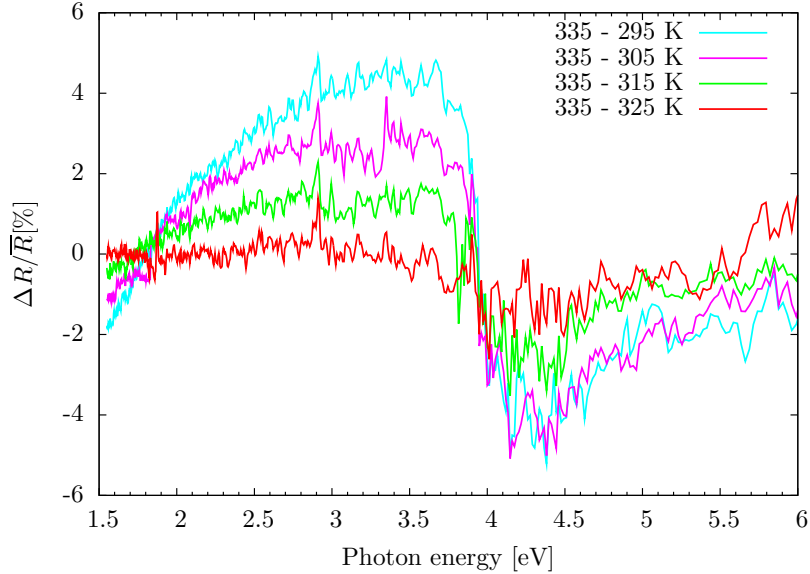
Figure 5.17: Differential reflectance spectra for different temperatures. The light was polarized along the MnAs [11$\bar{2}$0] direction.

entirely in the β-phase, is almost zero. As the sample is cooled into the α-phase, an appreciable reflectance difference is detected.

Figure 5.18 shows a comparison of reflectance differences obtained for light polarized along the in-plane crystalline directions. As can be seen, the change in reflectance is similar for the two directions, but the reflectance along [0001] shows a feature at 3 eV, consistent with the RDS feature centered at 3 eV. This result is in line with the temperature-dependent differential reflectance (TDDR) spectra reported by Vidal [166].

A negative peak in the TDDR is observed at about 4.2 eV, but since the amplitudes are almost identical for both directions, no change in the RDS signal is present at that energy. An additional feature may exist at an energy of 5 eV, where our RDS measurements are not very sensitive due to the small DC signal.
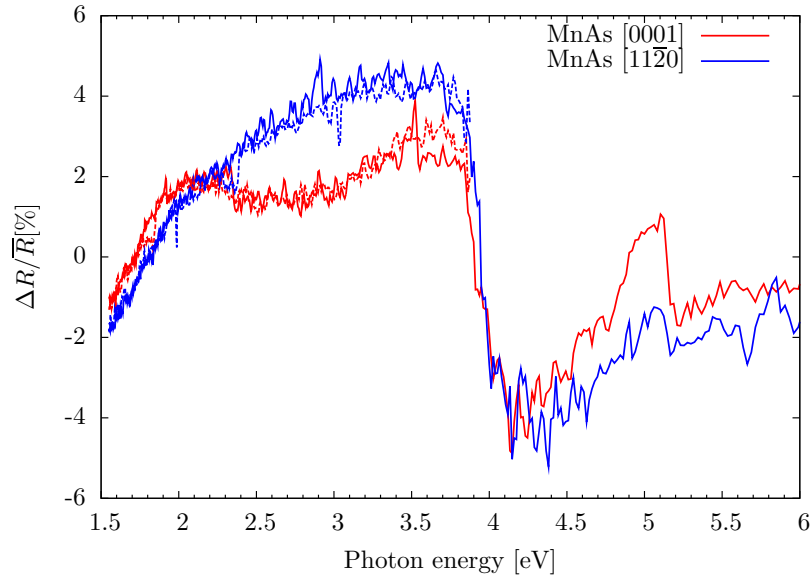
Figure 5.18: Differential reflectance spectra for light polarized along [0001] (red curve) and [11$\bar{2}$0] (blue). The temperature was changed from 335 to 295 K. The dashed lines show results obtained for the sample rotated by 90°.

We conclude that anisotropic intraband scattering may at least partially be responsible for appearance of 2.9 eV RDS feature. The sharp turn-on, however, would imply a very strong change in the scattering time along MnAs [0001].

Interband transitions

Finally, the spectral feature at 3 eV may also originate from interband transitions.

The As and Mn projected density of states of ferromagnetic MnAs, as calculated by density functional theory (DFT), is shown in Fig. 5.19. The dipolar selection rule ($\Delta l = \pm 1$) can be fulfilled for transitions from s- to p or p- to d-bands.

Peaks are found at -2 eV for the As-$4p$ and +1 eV for Mn-$3d$ projected minority spin contributions, with the difference of 3 eV in close correspondence with the 2.9 eV feature observed in the RDS spectrum. Both qualitative and quantitative
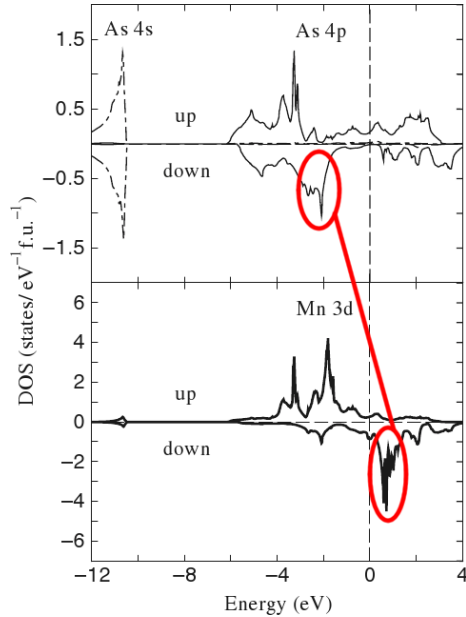
Figure 5.19: Projected density of states for MnAs, calculated by fully-relativistic DFT, from Li et al. [169] (reprinted with kind permission of the Japan Society of Applied Physics). The As-$4p$ to Mn-$3d$ minority band transition is marked in red.

changes in the DOS at the α- to β-transition could be responsible for the temperature dependence of the RDS signal. The exchange splitting of around 3 eV for Mn-$3d$ and 1 eV for As-$4p$ presumably would be reduced for β-MnAs, thus shifting or eliminating the observed RDS feature.

Magneto-Optic Kerr Effect

An additional contribution to the RDS signal (not considered by Vidal et al.) could arise from the magneto-optic Kerr effect (MOKE). Originating from spin-orbit coupling, it leads to non-zero off-diagonal elements of the dielectric tensor, which also give rise to a rotation of the incident polarization. Indeed, surface MOKE measurement are a standard tool to characterize magnetic properties of thin-films.

The basic optical setup for MOKE measurements is identical to the one used for

RDS. Three typical configurations are usually considered for the MOKE:

- Longitudinal (Magnetization in plane, parallel to plane of incidence)

- Transverse (Magnetization in plane, perpendicular to plane of incidence)

- Polar (Magnetization out of plane)

For near-normal incidence, the dominating contribution would normally be from the polar Kerr effect. However, since the magnetic easy axis is in the plane, the out-of-plane magnetization component should be small.
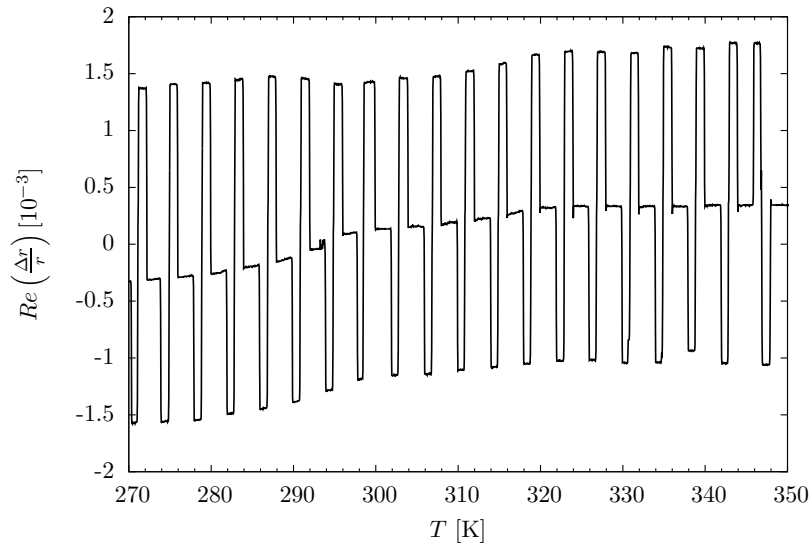
Figure 5.20: Magneto-optic polarization rotation observed with cryostat window in place. The permanent magnet was placed near the sample for a one Kelvin interval, then the polarity rotated for one Kelvin, and then removed for a two Kelvin interval.

To understand the influence of the Kerr effect on the RDS signal, a strong rare-earth magnet was brought close to the sample and changes in the RDS signal were observed.

The sensitivity of the experimental arrangement was demonstrated, when initial experiments indicated strong, systematic variations of RDS signal when the magnet

was brought close to the sample (Fig. 5.20). Since the amplitude of these variations was temperature independent, it became clear that this change in signal was in fact not due to the sample, but originated from the Faraday effect of the window glass, with its non-zero Verdet constant (≈ 10 rad/T $\cdot$ m for BK7 at 400 nm [170]). After removal of the window, the experiment was repeated in a purged Nitrogen atmosphere. The results are shown in Fig. 5.21.
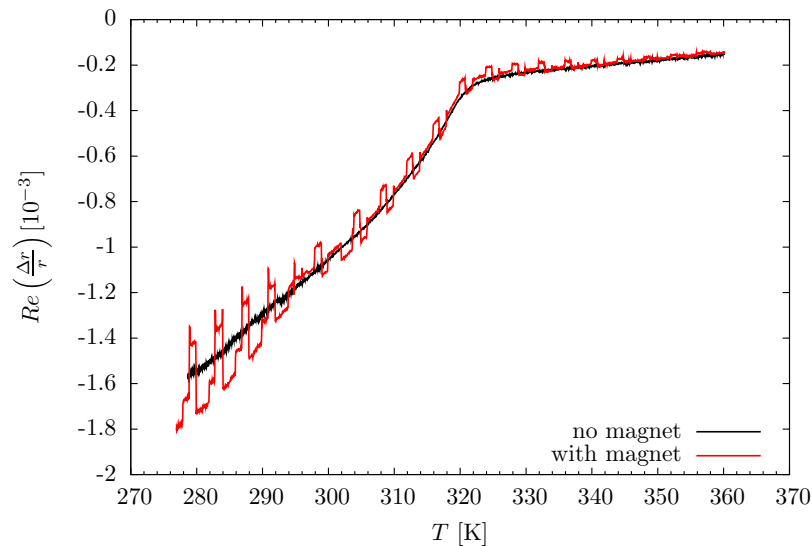
Figure 5.21: Magneto-optic polarization rotation observed on sample TE568 without the cryostat window.

Clearly, switching the orientation of the magnetic field leads to appreciable magneto-optic effect with a strongly temperature-dependent amplitude.

We conclude that the Kerr effect gives an important contribution to the RDS signal in the α-phase, but quickly disappears in the β-phase and can be in the temperature range of the β- to γ-transition.

5.3.5   The β- to γ-Transition

While there is no detectable change in the spectrum going from the β- to the γ-phase, the LRD measurement (Fig. 5.22) reveals a change in slope around 375 K. To extract the position of this kink, the intersection of separate linear fits to the low- (330 to 365 K) and high-temperature (390 to 425 K) RDS signal was computed.
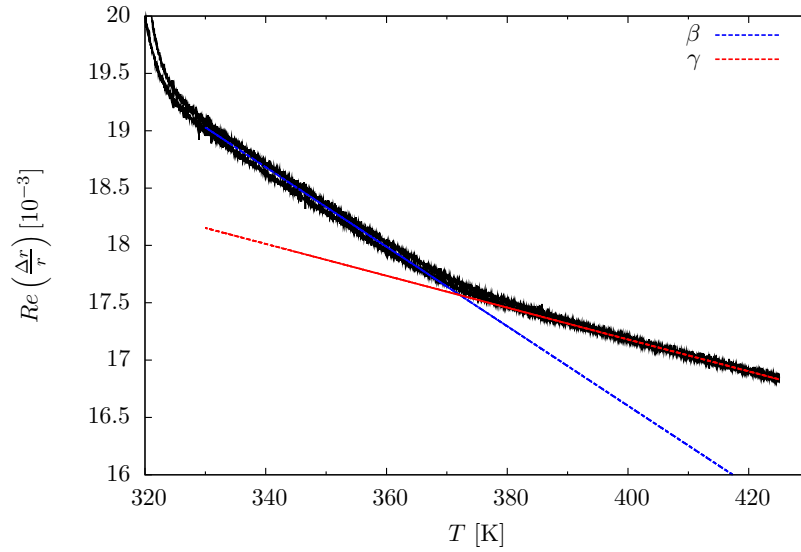
Figure 5.22: Laser reflection difference at 3.04 eV versus temperature. The straight lines are linear fits to the low-temperature (330 to 365 K) and high-temperature (390 to 425 K) regions.

The chopped RDS setup affords us the ability to also record RDS temperature scans for other fixed wavelengths using the Xe-arc lamp. Thus, we may obtain the data presented in Fig. 5.22 for a range of different photon energies, shown in Fig. 5.23.

For each of these scans, we obtained the relative change in slope, defined as

$$\frac{(dRDS/dT)_\beta - (dRDS/dT)_\gamma}{(dRDS/dT)_\gamma}, \tag{5.19}$$

and shown in Fig. 5.24. The normalization was chosen with respect to the slope of the γ-phase, which is only a weak function of photon energy.
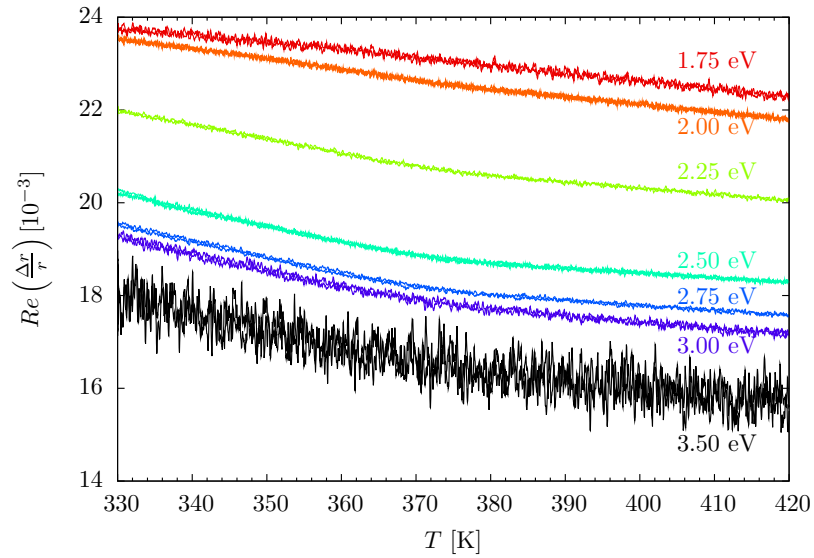
Figure 5.23: "Laser"-RDS temperature scans on sample TE578 for different energies, measured with Xe-arc lamp in the chopper setup.
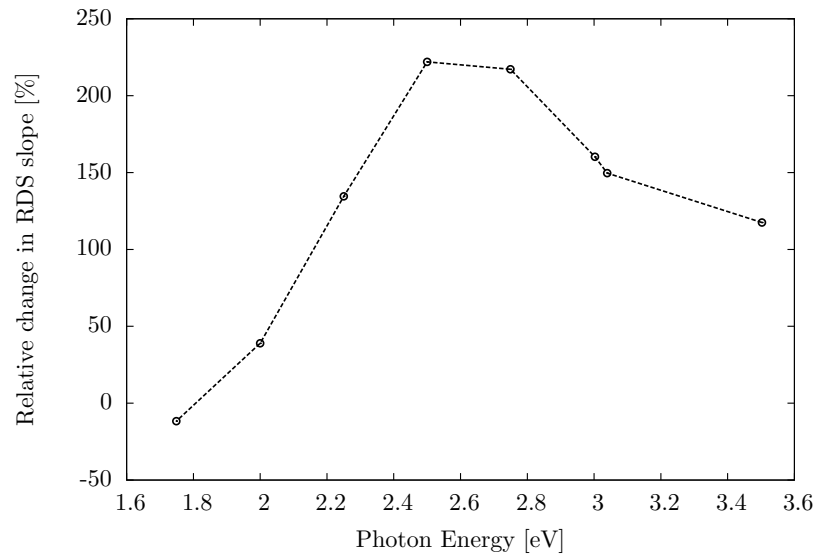
Figure 5.24: Relative slope change of the temperature-dependent RDS signal at the β- to γ-transition versus photon energy.

Clearly, the maximum change in slope occurs at a photon energy of around 2.7 eV, i.e. at a somewhat lower energy than the RDS spectral feature observed for the α-

phase. Nevertheless, this feature may arise from the same electronic transition, shifted to a lower energy due to a reduction in the exchange splitting.

5.4   Summary of the Results

In the foregoing, we have seen evidence of the β- to γ-transition using three different experimental techniques. Figure 5.25 gives an overview of the results for all three techniques on a single sample. The temperatures of the kinks in reflectance difference and out-of-plane lattice-constant coincide and are bracketed by the temperatures of the resistivity minima for the two in-plane crystallographic directions.
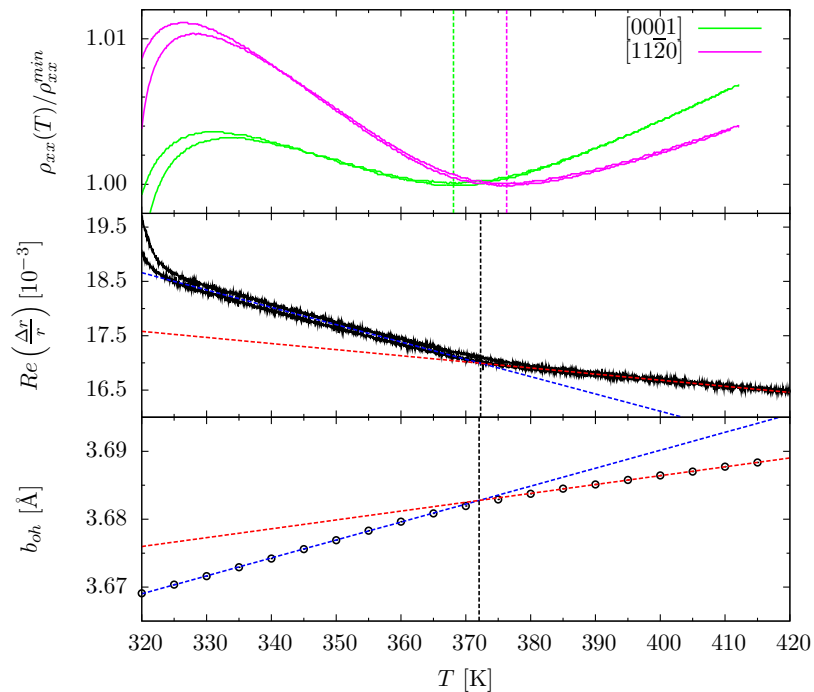
Figure 5.25: Resistivity, RDS signal, and out-of-plane lattice constant (from XRD) versus temperature for sample TE600.

The picture is completed by Table 5.4, which summarizes the β- to γ-transition temperatures obtained for several samples with the different methods. That the

close temperature correlation is not just a mere coincidence is confirmed by the considerable lower transition temperatures observed for both $\rho^{[0001]}$ and RDS signal in sample TE579.

	$\rho^{[11\bar{2}0]}$	$\rho^{[0001]}$	XRD	RDS
TE580	379.7 K	365.6 K		367.5 K
TE581	377.6 K	365.7 K		N/A
TE600	376.3 K	368.1 K	372.2 K	372.3 K
TE578	378.8 K	370.6 K		372.2 K
TE579		358.3 K		≈358 K

Table 5.4: β- to γ-transition temperatures from electrical ($\rho^{[11\bar{2}0]}$ & $\rho^{[0001]}$), X-ray diffraction (change in slope of b_o), and optical (RDS) measurements. For sample TE579, the RDS transition temperature given is only approximate, as the transition was more gradual and the RDS signal in the β-phase was not completely linear.

As can be seen, the transition temperature obtained from the minimum in $\rho^{[0001]}$ is always about 8 to 10 K lower than the one for $\rho^{[11\bar{2}0]}$. Since these measurements were taken simultaneously we can exclude systematic errors.

Interestingly, early X-ray diffraction measurements on bulk MnAs (see Fig. 2.3) also indicated that the c lattice constant temperature dependence changes slope at a lower temperature (≈ 403 K) than the a lattice constant (≈ 418 K). This sequence and difference in the transition temperatures is consistent with the results from our electrical measurements.

On the other hand, the crystallographic symmetry is not affected by the evolution of the c lattice constant. Rather, the evolution of both a and b lattice constants is relevant. To our knowledge, for thin-films no direct measurements of a and b lattice constants around the β/γ transition have been published (measurements of all three lattice parameters around the α- to β-transition have been reported in Adriano et al. [68]). Nonetheless, for the bulk Wilson and Kasper [33] observed that at a

temperature of about 398 ± 5 K, the orthorhombic distortion of the β-phase had disappeared and the structure had reached hexagonal symmetry again.

For the thin-film, the temperature of the β- to γ-phase transition seems to be lowered substantially. A likely cause is again the strain induced by the fixed epitaxial relationship.

Figure 5.26 shows a temperature-pressure phase diagram for the bulk as measured by Menyuk [44]. It can be seen that with increasing pressure, the β- to γ-transition shifts to higher temperatures, with a slope of approximately 23 K/kbar. If one extrapolates this to negative pressure (corresponding to tensile stress on the film), one finds that for a β/γ transition temperature of 370 K, a pressure of -1.23 kbar would be required.

As the thin-film is cooled from the growth temperature, both a- and c-axis experience strain due to the mismatch of thermal expansion coefficients. This is a plausible reason for the lowering of the β- to γ-transition temperature.

Owing to the biaxial nature of the strain-field, the observed shift cannot be directly related to the shift expected for a hydrostatic pressure.

5.5   Conclusions

The β- to γ-transition of MnAs has received much less attention than the α- to β-transition. Because of its second-order nature, the transition is subtle and therefore requires careful experimentation to observe.

Studies in thin-films so far have only remarked on the sign-change in resistance temperature-coefficient which is observed to occur at temperatures below the bulk transition temperature. Our careful directional electrical measurements reveal that
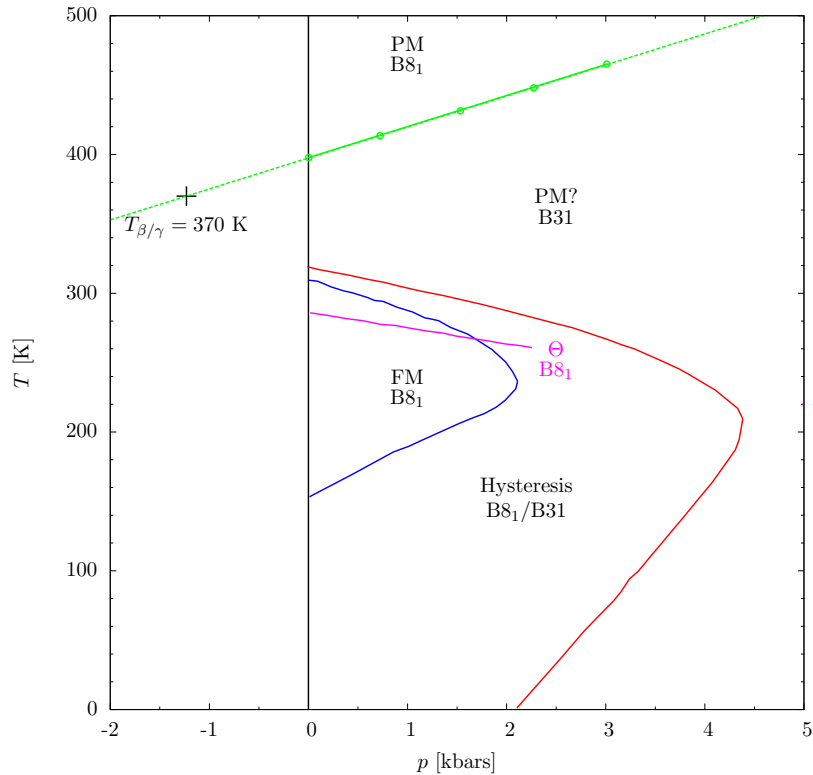
Figure 5.26: Temperature-Pressure phase diagram for bulk MnAs, after Menyuk et al. [44]. "Θ (B8$_1$)" denotes the apparent Curie temperature of the γ-phase. The cross marks a transition temperature of 370 K on the extrapolated (to negative pressure) β/γ transition curve.

the change in slope happens at different temperatures for the in-plane components of the resistivity tensor, namely at a lower temperature for the *c*-direction than the *a*-direction. This is in line with some early X-ray results on bulk MnAs, pointing toward the possibility of two closely spaced, but distinct phase transitions. Furthermore, the temperature coefficients of resistivity differ for the two in-plane crystallographic directions. As the phase transition is crossed, the high and low slope directions are reversed. The appearance of superzone gaps in the band-structure due to antiferromagnetic ordering in the β-phase may explain this behavior.

We discovered further evidence of the β- to γ-transition using X-ray diffraction

measurements of the out-of-plane lattice constant, where a change in slope is unambiguously observed in the same temperature interval.

Reflectance difference spectroscopy also reveals a change in the slope of the anisotropy signal at about the same temperature, with the maximum relative change occurring at an energy of about 2.7 eV. Although this energy is somewhat lower than the one of the RDS feature observed for the α-phase, it could in principle be caused by the same minority band transition.

Chapter 6

Conclusions

In this work, we have shown that new insights into phase transitions in MnAs thin-films can be gained from techniques that involve "local" measurements as opposed to conventional "bulk" methods such as SQUID magnetometry and calorimetry.

For this purpose, thin-films of MnAs were epitaxially grown on GaAs. It was found that high-quality films can be successfully grown at increased growth rates if the nucleation takes place at low growth rates and high enough Arsenic overpressure. Using X-ray reflection and AFM measurements, we were able to confirm the sharpness of the interface as well as the smoothness of the surface. X-ray diffraction measurements confirmed that films grown under the right growth conditions are purely in the A_0 orientation. This was further corroborated by the high degree of resistivity anisotropy observed for the in-plane directions. AFM scans of the surface revealed the periodic structure of the phase-coexistence stripes.

We demonstrated that previous difficulties in the patterning of MnAs thin-films can be overcome using a boron trichloride based inductively coupled plasma etch. This allowed us to perform directionally-dependent magnetotransport measurements on pristine films. The geometric arrangement of the stripes allowed us to determine

the phase-fractions of α- and β-MnAs using a simple electrical model. Excellent agreement was found for phase fractions determined independently for current along the two in-plane crystallographic directions.

In looking at the hysteresis of the phase fractions, we discovered a surprising substructure with the hysteresis going through three distinct maxima over the coexistence range. The evolution of this substructure was illustrated in minor hysteresis loops. Temperature-dependent X-ray diffraction experiments with a high-throughput powder diffractometer enabled us to independently check the structure of the hysteresis without the need for explicit fitting of the spectra. Comparison with AFM scans at the same temperatures lead us to suggest that the hysteresis is coupled to the ordering of the stripe structure.

Measurements of the anomalous Hall effect allowed to us follow the out-of-plane magnetization component across the phase transition. In the phase-coexistence regime, we discovered the evolution of stable out-of-plane magnetic domains induced by the change in shape anisotropy of the shrinking α-phase stripes. The phase fraction of the α-phase was shown to be the dominating order parameter for this phenomenon.

An anomalous Hall effect signal was found to persist to temperatures far above the α- to β-transition. The fact that the magnitude of this signal is independent of growth conditions led us to speculate that a residual magnetic ordering is inherent to the β-phase, not in contradiction to speculations about the possibility of antiferromagnetic order existing at least in strained β-MnAs.

Interestingly, although film morphology can vary quite substantially for different growth procedures, many of the electrical properties are qualitatively unaffected.

Reflectance-difference spectroscopy was used to probe for changes in the electronic structure across the phase transitions. A clear qualitative change in the spectra is

observed at the α- to β-transition, with a distinct feature appearing close to the d-electron plasma frequency (3 eV). We confirmed that the reflectance difference originates from a change of the reflectance along the [0001] direction. A minority Mn-3d to As-4p interband transition was identified as a likely source. However, in the presence of the ferromagnetic α-phase, the influence of the magneto-optical Kerr effect cannot be neglected.

A distinct change in slope of the RDS signal at about 375 K was identified as a subtle signature of the β- to γ-transition. Besides the slope change in the reflectance-difference signal at 2.7 eV, evidence of the transition was also found in:

- A change in slope of electrical resistance. For the γ-phase, a the thermal coefficient of resistance is positive. Unlike in earlier reports, we consistently find a negative coefficient in the β-phase. The change in slope occurs at a lower temperature for the [0001] than for [11$\bar{2}$0] direction. If indeed the slope is a consequence of a superzone gap due to antiferromagnetic ordering, this hints at the disappearance of magnetic coupling at a lower temperature in the [0001] direction.

- A change in slope is also clearly resolved at the same temperature in the out-of-plane lattice constant as determined by X-ray diffraction. The measured out-of-plane strain correlates well with the strain determined from simple assumptions.

We were thus able to show that the second-order β- to γ-transition is shifted to significantly lower temperatures than in the bulk, as a consequence of the biaxial strain induced by thermal expansion mismatch between MnAs and GaAs.

In summary, it becomes clear that important information about phase transitions can be gleaned from the use of more traditional thin-film techniques. The price for this is paid, however, in the more involved interpretation of the experimental results.

On the other hand, a combination of techniques may allow to substantiate and interpret the results from single experiments.

For the example system of MnAs, the high degree of structural order in the phase-coexistence regime simplifies some of the challenges. It is expected that the techniques demonstrated in this dissertation may also be applicable to other systems of current interest, e.g. functional nanomaterials such as thin-film ferroelectrics [171], where ordered phase structures are also common.

Appendices

Appendix A

AFM scans

AFM scans for a number of samples grown for this dissertation are shown in Figures A.1,A.2, and A.3. All scans were obtained at room temperature in non-contact mode. The x and y scales for all figures are chosen identical to allow for direct comparison, while the height (z) scale varies.

(a) TE568

(b) TE573
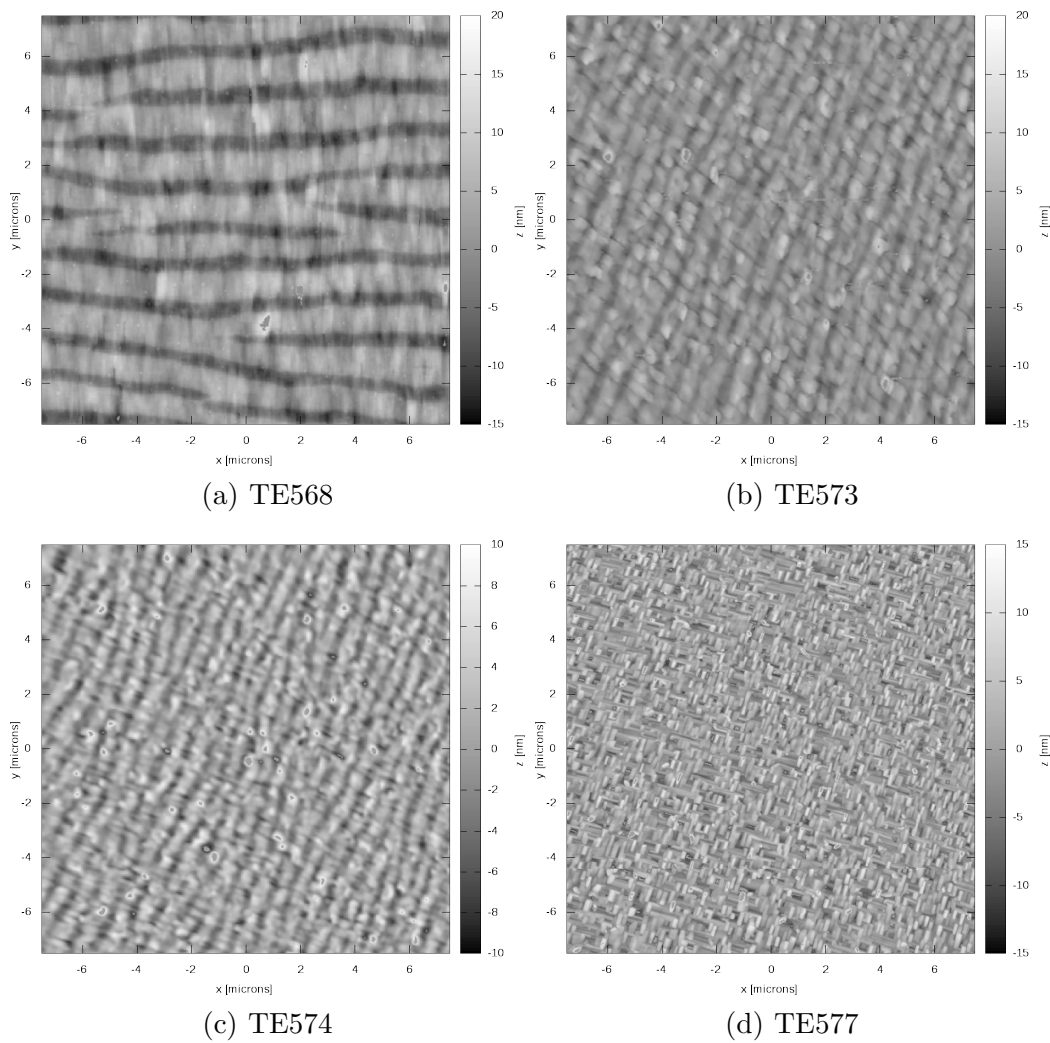
(c) TE574

(d) TE577

Figure A.1: AFM scans of samples TE568 through TE577.

(a) TE578

(b) TE579

(c) TE580

(d) TE581
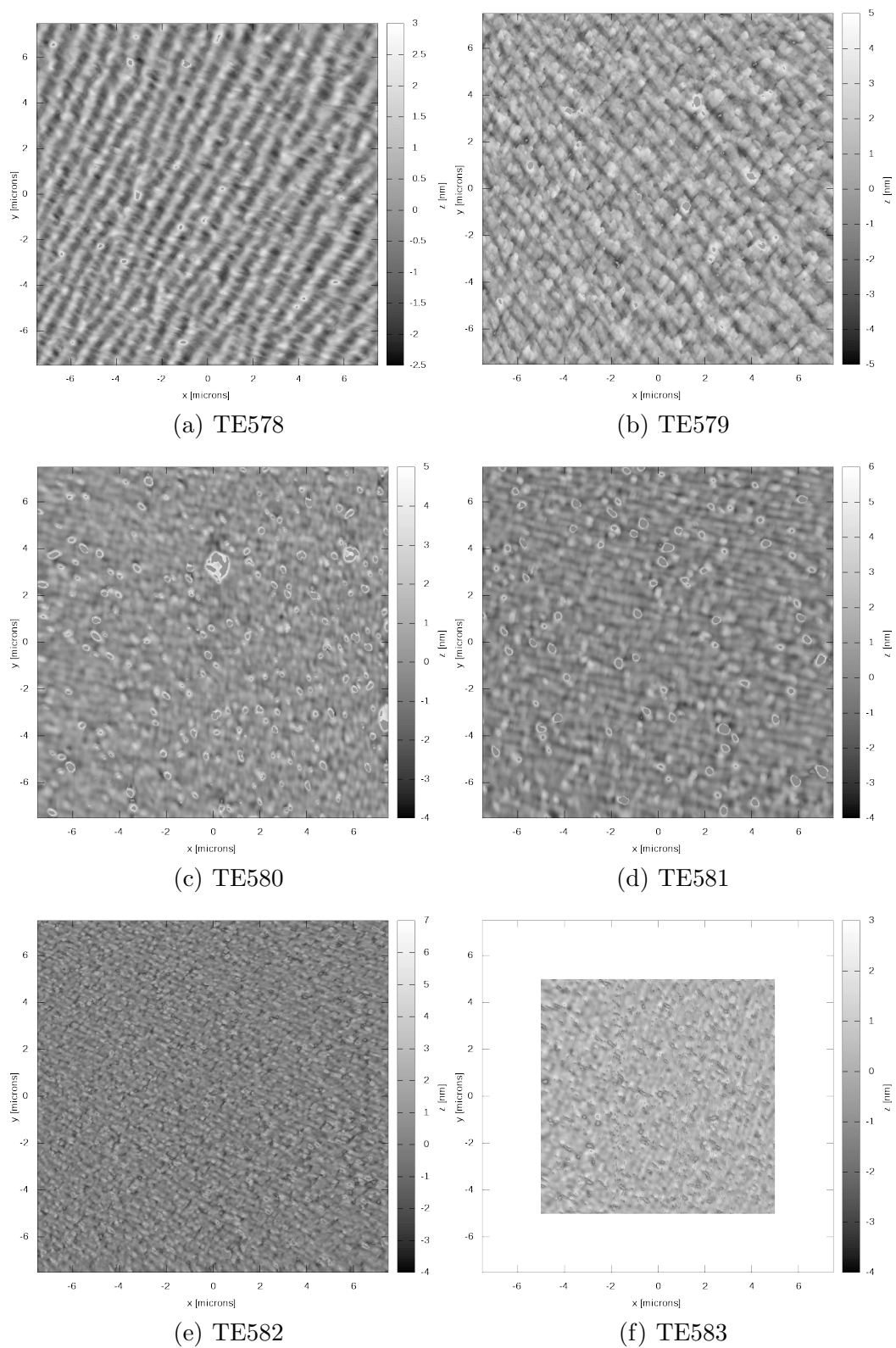
(e) TE582

(f) TE583

Figure A.2: AFM scans of samples TE578 through TE583.
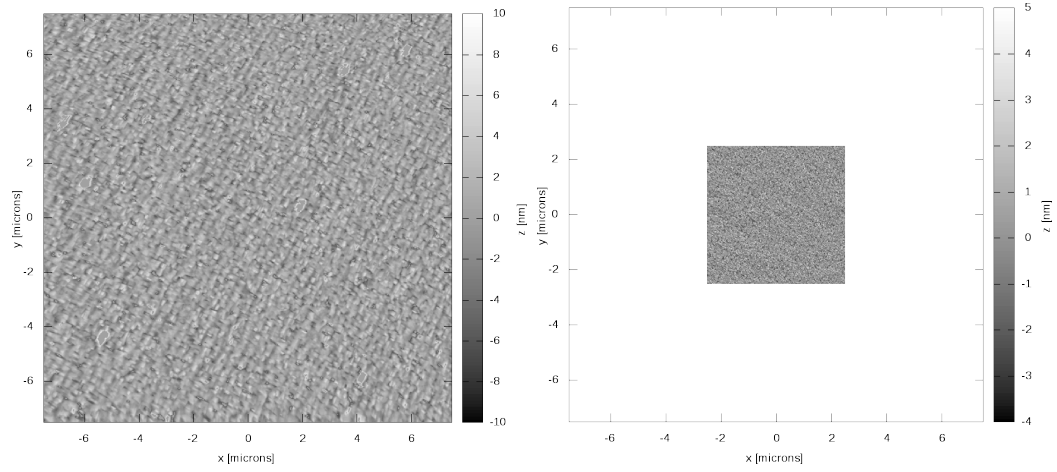
(a) TE594

(b) TE596
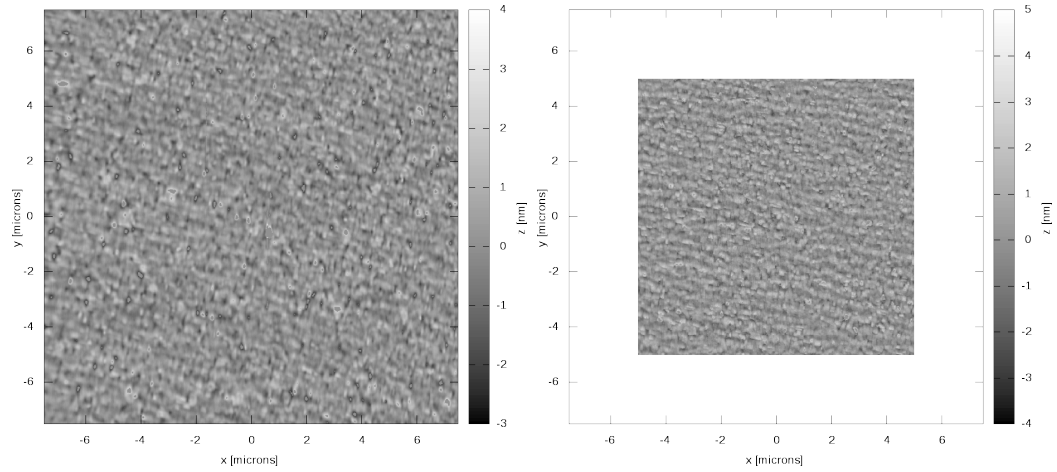
(c) TE597

(d) TE598
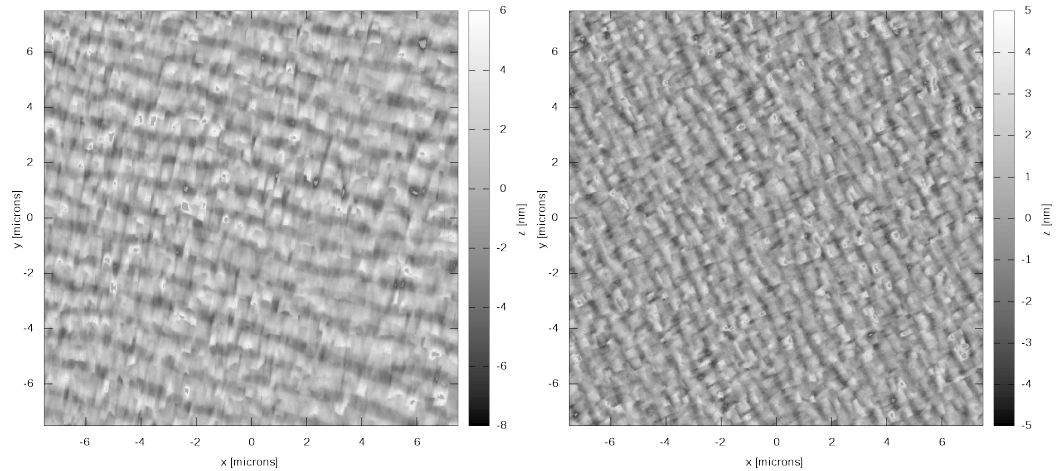
(e) TE599

(f) TE600

Figure A.3: AFM scans of samples TE594 through TE600.

Appendix B

Phase fraction

Figure B.1 shows the comparison of X-ray and resistivity phase fraction for samples TE578, TE579, TE580 and TE600.
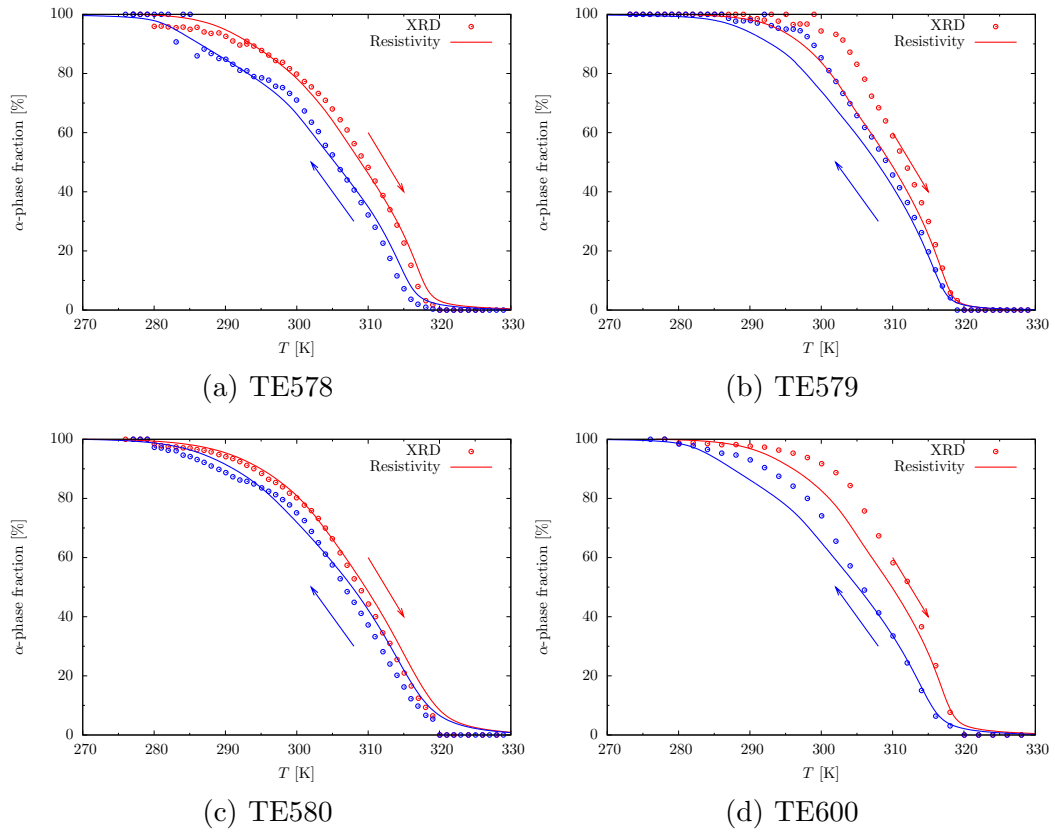
Figure B.1: Phase fraction versus temperature from X-ray (circles) and resistivity measurements (solid lines) for other samples.

References

[1] G. Schmidt, D. Ferrand, L. W. Molenkamp, A. T. Filip, and B. J. van Wees, "Fundamental obstacle for electrical spin injection from a ferromagnetic metal into a diffusive semiconductor," *Physical Review B*, vol. 62, pp. R4790–R4793, Aug 2000. 5

[2] E. I. Rashba, "Theory of electrical spin injection: Tunnel contacts as a solution of the conductivity mismatch problem," *Physical Review B*, vol. 62, pp. R16267–R16270, Dec 2000. 5

[3] H. Ohno, A. Shen, F. Matsukura, A. Oiwa, A. Endo, S. Katsumoto, and Y. Iye, "(Ga,Mn)As: A new diluted magnetic semiconductor based on GaAs," *Applied Physics Letters*, vol. 69, no. 3, pp. 363–365, 1996. 5

[4] K. Y. Wang, R. P. Campion, K. W. Edmonds, M. Sawicki, T. Dietl, C. T. Foxon, and B. L. Gallagher, "Magnetism in (Ga,Mn)As thin films with T_C up to 173 K," *AIP Conference Proceedings*, vol. 772, no. 1, pp. 333–334, 2005. 5, 6

[5] H.-P. Schönherr, R. Nötzel, W. Ma, and K. H. Ploog, "Evolution of the surface morphology of Fe grown on GaAs (100), (311)A, and (331)A substrates by molecular beam epitaxy," *Journal of Applied Physics*, vol. 89, no. 1, pp. 169–173, 2001. 5

REFERENCES

[6] K. H. Ploog, "Spin injection in ferromagnet-semiconductor heterostructures at room temperature (invited)," *Journal of Applied Physics*, vol. 91, no. 10, pp. 7256–7260, 2002. 5

[7] C. H. Li, G. Kioseoglou, O. M. J. van 't Erve, A. T. Hanbicki, B. T. Jonker, R. Mallory, M. Yasar, and A. Petrou, "Spin injection across (110) interfaces: Fe/GaAs(110) spin-light-emitting diodes," *Applied Physics Letters*, vol. 85, no. 9, pp. 1544–1546, 2004. 5

[8] M. Ramsteiner, H. Y. Hao, A. Kawaharazuka, H. J. Zhu, M. Kästner, R. Hey, L. Däweritz, H. T. Grahn, and K. H. Ploog, "Electrical spin injection from ferromagnetic MnAs metal layers into GaAs," *Physical Review B*, vol. 66, p. 081304, Aug 2002. 5

[9] Y.-J. Zhao, W. T. Geng, A. J. Freeman, and B. Delley, "Structural, electronic, and magnetic properties of α- and β-MnAs: LDA and GGA investigations," *Physical Review B*, vol. 65, p. 113202, Feb 2002. 5

[10] R. de Paiva, J. L. A. Alves, R. A. Nogueira, J. R. Leite, and L. M. R. Scolfaro, "First-principles materials study for spintronics: MnAs and MnN," *Brazilian Journal of Physics*, vol. 34, no. 2, pp. 568–570, 2004. 5

[11] H. Shimizu and M. Tanaka, "Magneto-optical properties of semiconductor-based superlattices having GaAs with MnAs nanoclusters," *Journal of Applied Physics*, vol. 89, no. 11, pp. 7281–7283, 2001. 6

[12] M. Tanaka, H. Shimizu, and M. Miyamura, "Enhancement of magneto-optical effect in a GaAs:MnAs hybrid nanostructure sandwiched by gaas/alas distributed Bragg reflectors: epitaxial semiconductor-based magneto-photonic crystal," *Journal of Crystal Growth*, vol. 227-228, pp. 839 – 846, 2001. 6

REFERENCES

[13] M. Yokoyama, T. Ogawa, A. M. Nazmul, and M. Tanaka, "Large magnetoresistance (> 600 %) of a GaAs:MnAs granular thin film at room temperature," *Journal of Applied Physics*, vol. 99, no. 8, p. 08D502, 2006. 6

[14] E. Brück, "Developments in magnetocaloric refrigeration," *Journal of Physics D: Applied Physics*, vol. 38, no. 23, pp. R381–R391, 2005. 6

[15] H. Wada and Y. Tanabe, "Giant magnetocaloric effect of $MnAs_{1-x}Sb_x$," *Applied Physics Letters*, vol. 79, no. 20, pp. 3302–3304, 2001. 6

[16] S. Gama, A. A. Coelho, A. de Campos, A. M. G. Carvalho, F. C. G. Gandra, P. J. von Ranke, and N. A. de Oliveira, "Pressure-induced colossal magnetocaloric effect in MnAs," *Physical Review Letters*, vol. 93, p. 237202, Nov 2004. 6

[17] A. de Campos, D. L. Rocco, A. M. G. Carvalho, L. Caron, A. A. Coelho, S. Gama, L. M. da Silva, F. C. G. Gandra, A. O. dos Santos, L. P. Cardoso, P. J. von Ranke, and N. A. de Oliveira, "Ambient pressure colossal magnetocaloric effect tuned by composition in $Mn_{1-x}Fe_xAs$," *Nature Materials*, vol. 5, no. 10, p. 802, 2006. 6

[18] M. Balli, D. Fruchart, D. Gignoux, and R. Zach, "The "colossal" magnetocaloric effect in $Mn_{1-x}Fe_xAs$: What are we really measuring?," *Applied Physics Letters*, vol. 95, no. 7, p. 072509, 2009. 6

[19] N. K. Sun, W. B. Cui, D. Li, D. Y. Geng, F. Yang, and Z. D. Zhang, "Giant room-temperature magnetocaloric effect in $Mn_{1-x}Cr_xAs$," *Applied Physics Letters*, vol. 92, no. 7, p. 072504, 2008. 6

[20] P. F. Xu, S. H. Nie, K. K. Meng, S. L. Wang, L. Chen, and J. H. Zhao, "Co doping enhanced giant magnetocaloric effect in $Mn_{1-x}Co_xAs$ films epitaxied on GaAs (001)," *Applied Physics Letters*, vol. 97, no. 4, p. 042502, 2010. 6

REFERENCES

[21] H. Wada, S. Matsuo, and A. Mitsuda, "Pressure dependence of magnetic entropy change and magnetic transition in MnAs$_{1-x}$Sb$_x$," *Physical Review B*, vol. 79, no. 9, p. 092407, 2009. 6

[22] A. Serres, "Paramagnétisme de quelques composés du manganèse," *Journal de Physique et Le Radium*, vol. 8, no. 5, pp. 146–151, 1947. 8, 13

[23] C. Guillaud, "Les points de transformation des composés définis MnAs, MnBi en relation avec un mécanisme probable d'antiferromagnétisme," *Journal de Physique et Le Radium*, vol. 12, no. 3, pp. 223–227, 1951. 8, 13, 14

[24] C. Kittel, "Model of exchange-inversion magnetization," *Physical Review*, vol. 120, pp. 335–342, Oct 1960. 8

[25] C. P. Bean and D. S. Rodbell, "Magnetic disorder as a first-order phase transformation," *Physical Review*, vol. 126, pp. 104–115, Apr 1962. 8, 10, 14

[26] M. Yuzuri and M. Yamada, "On the magnetic properties of the compound Mn$_2$As," *Journal of the Physical Society of Japan*, vol. 15, no. 10, pp. 1845–1850, 1960. 9, 108

[27] A. E. Austin, E. Adelson, and W. H. Cloud, "Magnetic structures of Mn$_2$As and Mn$_2$Sb$_{0.7}$As$_{0.3}$," *Journal of Applied Physics*, vol. 33, no. 3, pp. 1356–1357, 1962. 9, 108

[28] K. Cenzual, L. M. Gelato, M. Penzo, and E. Parthé, "Inorganic structure types with revised space groups. I," *Acta Crystallographica Section B*, vol. 47, pp. 433–439, Aug 1991. 9

[29] M. Yuzuri, "Electron spin resonance studies of the compounds Mn$_3$As$_2$, MnAs and Mn$_2$Sb," *Science reports of the Yokohama National University*, vol. 18, pp. 13–18, 1971. 9

REFERENCES

[30] B. Predel, *As-Mn (Arsenic - Manganese)*. Landolt-Börnstein, Springer Berlin Heidelberg, new series ed., 2006. xvi, 9, 16

[31] T. Suzuki and H. Ido, "Relation between structural and magnetic properties of compound $MnAs_{1-x}P_x$ ($0 \leq x \leq 0.275$)," *Journal of the Physical Society of Japan*, vol. 51, no. 10, pp. 3149–3156, 1982. xvi, xvii, xx, 10, 11, 12, 20, 65

[32] N. P. Grazhdankina and A. M. Burkhanov, "Elastic Properties of Manganese Arsenide in the Magnetic Transformation Region," *Soviet Journal of Experimental and Theoretical Physics*, vol. 23, pp. 1013–1016, Dec. 1966. 10

[33] R. H. Wilson and J. S. Kasper, "The crystal structure of MnAs above 40°C," *Acta Crystallographica*, vol. 17, pp. 95–101, Feb 1964. 10, 14, 146

[34] B. T. M. Willis and H. P. Rooksby, "Magnetic transitions and structural changes in hexagonal Manganese compounds," *Proceedings of the Physical Society, Section B*, vol. 67, no. 4, pp. 290–296, 1954. xvi, 11, 12

[35] L. Däweritz, "Interplay of stress and magnetic properties in epitaxial MnAs films," *Reports on Progress in Physics*, vol. 69, no. 9, pp. 2581–2629, 2006. 11, 17, 21

[36] I. Rungger and S. Sanvito, "Ab initio study of the magnetostructural properties of MnAs," *Physical Review B*, vol. 74, no. 2, p. 024429, 2006. 11, 14

[37] A. J. Meyer and P. Taglang, "Influence du champ magnétique sur une transformation polymorphique d'un ferromagnétique," *Journal de Physique et Le Radium*, vol. 14, pp. 82–84, Feb. 1953. 13

[38] R. W. De Blois and D. S. Rodbell, "Magnetic first-order phase transition in single-crystal MnAs," *Physical Review*, vol. 130, pp. 1347–1360, May 1963. 13, 14, 27

REFERENCES

[39] J. B. Goodenough and J. A. Kafalas, "High-pressure study of the first-order phase transition in MnAs," *Physical Review*, vol. 157, pp. 389–395, May 1967. 13, 14

[40] H. Ido, "Magnetic properties of mixed crystals with NiAs-type structure," *Journal of Applied Physics*, vol. 57, no. 8, pp. 3247–3249, 1985. xvi, 13

[41] G. E. Bacon and R. Street, "Magnetic structure of manganese arsenide," *Nature*, vol. 175, no. 4455, p. 518, 1955. 14

[42] R. W. De Blois and D. S. Rodbell, "Magnetic first-order phase transition and anisotropy in single-crystal MnAs," *Journal of Applied Physics*, vol. 34, no. 4, pp. 1101–1103, 1963. 14, 27

[43] T. Kato, K. Nagai, and T. Aisaka, "A model of magneto-structural phase transition in MnAs," *Journal of Physics C: Solid State Physics*, vol. 16, no. 16, pp. 3183–3196, 1983. 14

[44] N. Menyuk, J. A. Kafalas, K. Dwight, and J. B. Goodenough, "Effects of pressure on the magnetic properties of MnAs," *Physical Review*, vol. 177, pp. 942–951, Jan 1969. xxvii, 14, 147, 148

[45] M. K. Niranjan, B. R. Sahu, and L. Kleinman, "Density functional determination of the magnetic state of β-MnAs," *Physical Review B*, vol. 70, no. 18, p. 180406, 2004. 14

[46] L. M. Sandratskii and E. Şaşioğlu, "Unusual sequence of phase transitions in MnAs: First-principles study," *Physical Review B*, vol. 74, no. 21, p. 214422, 2006. 14

[47] J. E. Ayers, *Heteroepitaxy of Semiconductors: theory, growth, and characterization.* CRC Press Taylor & Francis Group, 2007. xvii, 14, 20

REFERENCES

[48] M. Dörfler and K. Bärner, "The elastic constants of MnAs," *physica status solidi (a) - applications and materials science*, vol. 17, no. 1, pp. 141–148, 1973. xxviii, 15

[49] B. W. Roberts, "Neutron diffraction study of the structures and magnetic properties of manganese bismuthide," *Physical Review*, vol. 104, pp. 607–616, Nov 1956. 16

[50] E. E. Huber and D. H. Ridgley, "Magnetic properties of a single crystal of manganese phosphide," *Physical Review*, vol. 135, pp. A1033–A1040, Aug 1964. 16

[51] A. Kjekshus and W. Pearson, "Phases with the nickel arsenide and closely-related structures," *Progress in Solid State Chemistry*, vol. 1, pp. 83 – 174, 1964. 16

[52] R. R. Heikes, "Magnetic transformation in MnBi," *Physical Review*, vol. 99, pp. 446–447, Jul 1955. 16

[53] A. Zieba, Y. Shapira, and S. Foner, "Magnetic phase diagram of MnAs: Effect of magnetic field on structural and magnetic transitions," *Physics Letters A*, vol. 91, no. 5, pp. 243 – 245, 1982. 16

[54] W. Reimers, E. Hellner, W. Treutmann, and G. Heger, "Magnetic phase diagram of the system $Mn_{1-x}Cr_xSb$ ($0 \leq x \leq 1$)," *Journal of Physics C: Solid State Physics*, vol. 15, no. 16, p. 3597, 1982. 16

[55] S. J. Pearton, C. R. Abernathy, D. P. Norton, A. F. Hebard, Y. D. Park, L. A. Boatner, and J. D. Budai, "Advances in wide bandgap materials for semiconductor spintronics," *Materials Science and Engineering: R: Reports*, vol. 40, no. 4, pp. 137 – 168, 2003. 16

REFERENCES

[56] S.-H. Kim, M. Boström, and D.-K. Seo, "Two-dimensional superdegeneracy and structure–magnetism correlations in strong ferromagnet, Mn_2Ga_5," *Journal of the American Chemical Society*, vol. 130, no. 4, pp. 1384–1391, 2008. 16

[57] T. A. Bither and W. H. Cloud, "Magnetic tetragonal delta phase in the Mn-Ga binary," *Journal of Applied Physics*, vol. 36, no. 4, pp. 1501–1502, 1965. 16

[58] K. M. Krishnan, "Ferromagnetic δ-$Mn_{1-x}Ga_x$ thin films with perpendicular anisotropy," *Applied Physics Letters*, vol. 61, no. 19, pp. 2365–2367, 1992. 16

[59] M. Tanaka, J. P. Harbison, J. DeBoeck, T. Sands, B. Philips, T. L. Cheeks, and V. G. Keramidas, "Epitaxial growth of ferromagnetic ultrathin MnGa films with perpendicular magnetization on GaAs," *Applied Physics Letters*, vol. 62, no. 13, pp. 1565–1567, 1993. 16

[60] M. Tanaka, J. P. Harbison, M. C. Park, Y. S. Park, T. Shin, and G. M. Rothberg, "Epitaxial ferromagnetic MnAs thin films grown by molecular-beam epitaxy on GaAs: Structure and magnetic properties," *Journal of Applied Physics*, vol. 76, no. 10, pp. 6278–6280, 1994. 17, 34

[61] M. Tanaka, J. P. Harbison, M. C. Park, Y. S. Park, T. Shin, and G. M. Rothberg, "Epitaxial orientation and magnetic properties of MnAs thin films grown on (001) GaAs: Template effects," *Applied Physics Letters*, vol. 65, no. 15, pp. 1964–1966, 1994. 17

[62] K. Akeura, M. Tanaka, M. Ueki, and T. Nishinaga, "Epitaxial ferromagnetic MnAs thin films grown by molecular beam epitaxy on Si(001) substrates," *Applied Physics Letters*, vol. 67, no. 22, pp. 3349–3351, 1995. 17, 34

[63] M. Yokoyama, S. Ohya, and M. Tanaka, "Growth and magnetic properties of

168

REFERENCES

epitaxial MnAs thin films grown on InP(001)," *Applied Physics Letters*, vol. 88, no. 1, p. 012504, 2006. 17, 34

[64] M. Yokoyama, S. Ohya, and M. Tanaka, "Molecular beam epitaxy growth, magnetic and structural properties of MnAs thin films grown on InP(001) and InGaAsP," *Journal of Crystal Growth*, vol. 301-302, p. 615, 2007. 17

[65] S. Hegde, E. Fraser, J. Kwon, H. Zeng, and H. Luo, "Growth and characterization of MnAs on HOPG," *APS Meeting Abstracts*, pp. 32012–+, Mar. 2009. 17

[66] F. Iikawa, M. J. S. P. Brasil, O. D. D. Couto, C. Adriano, C. Giles, and L. Däweritz, "Effect of MnAs/GaAs(001) film accommodations on the phase-transition temperature," *Applied Physics Letters*, vol. 85, no. 12, pp. 2250–2252, 2004. xvi, 18

[67] D. K. Satapathy, V. M. Kaganer, B. Jenichen, W. Braun, L. Däweritz, and K. H. Ploog, "Periodic array of misfit dislocations at the MnAs/GaAs interface studied by synchrotron x-ray diffraction," *Physical Review B*, vol. 72, no. 15, p. 155303, 2005. 19

[68] C. Adriano, C. Giles, O. Couto, M. Brasil, F. Iikawa, and L. Däweritz, "Strain redistribution at the phase transition of MnAs/GaAs(001) films," *Applied Physics Letters*, vol. 88, APR 2006. 19, 64, 146

[69] V. M. Kaganer, B. Jenichen, F. Schippan, W. Braun, L. Däweritz, and K. H. Ploog, "Strain-mediated phase coexistence in heteroepitaxial films," *Physical Review Letters*, vol. 85, pp. 341–344, Jul 2000. 21, 52, 91

[70] V. M. Kaganer, B. Jenichen, F. Schippan, W. Braun, L. Däweritz, and K. H. Ploog, "Strain-mediated phase coexistence in MnAs heteroepitaxial films on

GaAs: An X-ray diffraction study," *Physical Review B*, vol. 66, p. 045305, Jul 2002. 21, 22, 52, 59

[71] N. Sridhar, J. M. Rickman, and D. J. Srolovitz, "Twinning in thin films–I. Elastic analysis," *Acta Materialia*, vol. 44, no. 10, pp. 4085 – 4096, 1996. 21

[72] N. Sridhar, J. M. Rickman, and D. J. Srolovitz, "Twinning in thin films–II. Equilibrium microstructures," *Acta Materialia*, vol. 44, no. 10, pp. 4097 – 4113, 1996. 21

[73] B. Jenichen, V. M. Kaganer, M. Kästner, C. Herrmann, L. Däweritz, K. H. Ploog, N. Darowski, and I. Zizak, "Structural and magnetic phase transition in MnAs(0001)/GaAs(111) epitaxial films," *Physical Review B*, vol. 68, p. 132301, Oct 2003. 22, 34

[74] A. Aharoni, *Introduction to the Theory of Ferromagnetism.* Oxford University Press, 2 ed., 2000. 23, 27

[75] J. Crangle, *The Magnetic Properties of Solids.* Edward Arnold, Jan. 1977. 23

[76] G. Bertotti, *Hysteresis in Magnetism.* Academic Press, 1998. 23

[77] J. Stöhr and H. C. Siegmann, *Magnetism - From Fundamentals to Nanoscale Dynamics.* Solid-State Sciences, Springer Berlin / Heidelberg, 2006. 23, 110

[78] J. D. Zou, H. Wada, B. G. Shen, J. R. Sun, and W. Li, "Giant magnetocaloric effect and soft-mode magneto-structural phase transition in MnAs," *Europhysics Letters*, vol. 81, no. 4, p. 47002 (4pp), 2008. 25

[79] A. Aharoni, "Demagnetizing factors for rectangular ferromagnetic prisms," *Journal of Applied Physics*, vol. 83, no. 6, pp. 3432–3434, 1998. 26

[80] C. M. Hurd, *The Hall Effect in Metals and Alloys.* The International Cryogenic Monograph Series, Plenum Press, 1972. 29

REFERENCES

[81] R. Karplus and J. M. Luttinger, "Hall effect in ferromagnetics," *Physical Review*, vol. 95, pp. 1154–1160, Sep 1954. 31

[82] J. Smit, "The spontaneous Hall effect in ferromagnetics I," *Physica*, vol. 21, pp. 877 – 887, 1955. 32

[83] J. Smit, "The spontaneous Hall effect in ferromagnetics II," *Physica*, vol. 24, pp. 39 – 51, 1958. 32

[84] L. Berger, "Side-jump mechanism for the Hall effect of ferromagnets," *Physical Review B*, vol. 2, pp. 4559–4566, Dec 1970. 32

[85] M. V. Berry, "Quantal phase factors accompanying adiabatic changes," *Proceedings of the Royal Society A: Mathematical, Physical and Engineering Sciences*, vol. 392, no. 1802, p. 45, 1984. 32

[86] M.-C. Chang and Q. Niu, "Berry phase, hyperorbits, and the Hofstadter spectrum: Semiclassical dynamics in magnetic Bloch bands," *Physical Review B*, vol. 53, pp. 7010–7023, Mar 1996. 32

[87] G. Sundaram and Q. Niu, "Wave-packet dynamics in slowly perturbed crystals: Gradient corrections and Berry-phase effects," *Physical Review B*, vol. 59, pp. 14915–14925, Jun 1999. 32

[88] J. Ye, Y. B. Kim, A. J. Millis, B. I. Shraiman, P. Majumdar, and Z. Tešanović, "Berry phase theory of the anomalous Hall effect: Application to colossal magnetoresistance manganites," *Physical Review Letters*, vol. 83, pp. 3737–3740, Nov 1999. 32

[89] T. Jungwirth, Q. Niu, and A. H. MacDonald, "Anomalous Hall effect in ferromagnetic semiconductors," *Physical Review Letters*, vol. 88, p. 207208, May 2002. 32

REFERENCES

[90] F. D. M. Haldane, "Berry curvature on the Fermi surface: Anomalous Hall effect as a topological Fermi-liquid property," *Physical Review Letters*, vol. 93, p. 206602, Nov 2004. 32

[91] N. Nagaosa, J. Sinova, S. Onoda, A. H. MacDonald, and N. P. Ong, "Anomalous Hall effect," *Reviews of Modern Physics*, vol. 82, pp. 1539–1592, May 2010. 32

[92] E. A. Mityushov, N. I. Kourov, and Y. P. Irkhin, "Hall effect in microscopically inhomogeneous magnetic alloys," *Physics of the Solid State*, vol. 41, pp. 87–90, January 1999. 32

[93] S. Zhang, "Extraordinary Hall effect in magnetic multilayers," *Physical Review B*, vol. 51, pp. 3632–3636, Feb 1995. 33

[94] K.-J. Friedland, M. Kästner, and L. Däweritz, "Ordinary Hall effect in MBE-grown MnAs films grown on GaAs(001) and GaAs(111)B," *Physical Review B*, vol. 67, p. 113301, Mar 2003. 33, 66

[95] L. Däweritz, L. Wan, B. Jenichen, C. Herrmann, J. Mohanty, A. Trampert, and K. H. Ploog, "Thickness dependence of the magnetic properties of MnAs films on GaAs(001) and GaAs(113)A: Role of a natural array of ferromagnetic stripes," *Journal of Applied Physics*, vol. 96, no. 9, pp. 5056–5062, 2004. 34, 52

[96] Y. Morishita, K. Iida, J. Abe, and K. Sato, "Substrate-orientation dependence on structure and magnetic properties of MnAs epitaxial layers," *Japanese Journal of Applied Physics*, vol. 36, pp. L1100–L1103, 1997. 34

[97] Y. Takagaki, C. Herrmann, B. Jenichen, J. Herfort, and O. Brandt, "Growth of m-plane MnAs on GaAs(111)B by molecular beam epitaxy," *Applied Physics Letters*, vol. 92, no. 10, p. 101918, 2008. 34

REFERENCES

[98] R. N. Sacks, D. Barlett, C. A. Taylor II, and J. Williams, "Growth related interference effects in band edge thermometry of semiconductors," *Journal of Vacuum Science & Technology B*, vol. 23, no. 3, pp. 1247–1251, 2005. 35

[99] R. Nakane, S. Sugahara, and M. Tanaka, "Effect of postgrowth annealing on the morphology and magnetic properties of MnAs thin films grown on GaAs(001) substrates," *Journal of Applied Physics*, vol. 95, no. 11, pp. 6558–6561, 2004. 37

[100] M. Sing, B. Schmid, W. Drube, P. Klar, W. Heimbrodt, W. Stolz, J. Wenisch, K. Brunner, and R. .Claessen, "Hard X-ray photoemission on MnAs films and MnAs clusters in a GaAs matrix." HASYLAB Annual Report, 2005. 37

[101] F. Schippan, M. Kästner, L. Däweritz, and K. H. Ploog, "Growth control of MnAs on GaAs(001) by reflection high-energy electron diffraction," *Applied Physics Letters*, vol. 76, no. 7, pp. 834–836, 2000. 38

[102] J. Sadowski and J. Z. Domagala, "Influence of defects on the lattice constant of GaMnAs," *Physical Review B*, vol. 69, p. 075206, Feb 2004. 44

[103] L. X. Zhao, C. R. Staddon, K. Y. Wang, K. W. Edmonds, R. P. Campion, B. L. Gallagher, and C. T. Foxon, "Intrinsic and extrinsic contributions to the lattice parameter of GaMnAs," *Applied Physics Letters*, vol. 86, no. 7, p. 071902, 2005. 44

[104] I. Kuryliszyn-Kudelska, J. Z. D. a, T. Wojtowicz, X. Liu, E. Łusakowska, W. Dobrowolski, and J. K. Furdyna, "Effect of Mn interstitials on the lattice parameter of $Ga_{1-x}Mn_xAs$," *Journal of Applied Physics*, vol. 95, no. 2, pp. 603–608, 2004. 44

[105] A. Wolos, M. Kaminska, M. Palczewska, A. Twardowski, X. Liu, T. Wojtowicz,

and J. K. Furdyna, "Properties of arsenic antisite defects in $Ga_{1-x}Mn_xAs$," *Journal of Applied Physics*, vol. 96, no. 1, pp. 530–533, 2004. 45

[106] Philips Analytical X-Ray B.V., "Wingixa," Nov. 1998. Version V1.102. 46

[107] F. Iikawa, M. Knobel, P. V. Santos, C. Adriano, O. D. D. Couto, M. J. S. P. Brasil, C. Giles, R. Magalhães-Paniago, and L. Däweritz, "Effect of a magnetic field on the magnetostructural phase transition of MnAs films on GaAs," *Physical Review B*, vol. 71, no. 4, p. 045319, 2005. 52

[108] F. Iikawa, M. J. S. P. Brasil, C. Adriano, O. D. D. Couto, C. Giles, P. V. Santos, L. Däweritz, I. Rungger, and S. Sanvito, "Lattice distortion effects on the magnetostructural phase transition of MnAs," *Physical Review Letters*, vol. 95, no. 7, p. 077203, 2005. 52

[109] H. Yamaguchi, A. K. Das, A. Ney, T. Hesjedal, C. Pampuch, D. M. Schaadt, and R. Koch, "From ferro- to antiferromagnetism via exchange-striction of MnAs/GaAs(001)," *Europhysics Letters*, vol. 72, no. 3, pp. 479–485, 2005. 52

[110] V. Garcia, Y. Sidis, M. Marangolo, F. Vidal, M. Eddrief, P. Bourges, F. Maccherozzi, F. Ott, G. Panaccione, and V. Etgens, "Biaxial strain in the hexagonal plane of MnAs thin films: The key to stabilize ferromagnetism to higher temperature," *Physical Review Letters*, vol. 99, p. 117205, Sep. 2007. 52

[111] T. Plake, T. Hesjedal, J. Mohanty, M. Kästner, L. Däweritz, and K. H. Ploog, "Temperature-dependent magnetic force microscopy investigation of epitaxial MnAs films on GaAs(001)," *Applied Physics Letters*, vol. 82, no. 14, pp. 2308–2310, 2003. 52, 53

[112] J. R. Mohanty, *Micromagnetic investigation of MnAs thin films on GaAs surfaces.* PhD thesis, Humboldt-Universität zu Berlin, 2005. 52, 53

REFERENCES

[113] L. N. Coelho, B. R. A. Neves, R. MagalhÃ£es-Paniago, F. C. Vicentin, J. H. Westfahl, R. M. Fernandes, F. Iikawa, L. Däweritz, C. Spezzani, and M. Sacchi, "Magnetic reconfiguration of MnAs/GaAs(001) observed by magnetic force microscopy and resonant soft x-ray scattering," *Journal of Applied Physics*, vol. 100, no. 8, p. 083906, 2006. 52

[114] K.-S. Ryu, J. Kim, Y. Lee, H. Akinaga, T. Manago, R. Viswan, and S.-C. Shin, "Origin of uniaxial magnetic anisotropy in epitaxial MnAs film on GaAs(001) substrate," *Applied Physics Letters*, vol. 92, no. 8, p. 082503, 2008. 52

[115] R. Engel-Herbert, T. Hesjedal, J. Mohanty, D. M. Schaadt, and K. H. Ploog, "Magnetization reversal in MnAs films: Magnetic force microscopy, SQUID magnetometry, and micromagnetic simulations," *Physical Review B*, vol. 73, no. 10, p. 104441, 2006. 52

[116] R. Engel-Herbert, T. Hesjedal, and D. M. Schaadt, "Three-dimensional micromagnetic domain structure of MnAs films on GaAs(001): Experimental imaging and simulations," *Physical Review B*, vol. 75, p. 094430, Mar 2007. 52, 90

[117] T. Manago, A. Sinsarp, and H. Akinaga, "Magnetoresistance in epitaxially grown MnAs films on GaAs substrates," *Journal of Applied Physics*, vol. 102, no. 3, p. 033920, 2007. 52, 66

[118] R. Engel-Herbert and T. Hesjedal, "Magnetic coupling of ferromagnetic stripe arrays: Analytical model for the alpha-beta-phase coexistence regime of MnAs/GaAs(001)," *Physical Review B*, vol. 78, no. 23, p. 235309, 2008. 52, 90

[119] J. Mohanty, T. Hesjedal, A. Ney, Y. Takagaki, R. Koch, L. Däweritz, and K. H. Ploog, "Effect of strain on the local phase transition temperature of MnAs/GaAs(001)," *Applied Physics Letters*, vol. 83, no. 14, pp. 2829–2831, 2003. 53

REFERENCES

[120] R. W. Cheary and A. Coelho, "A fundamental parameters approach to X-ray line-profile fitting," *Journal of Applied Crystallography*, vol. 25, pp. 109–121, Apr 1992. xix, 62

[121] C. Dong, H. Chen, and F. Wua, "A new Cu $K_{\alpha 2}$-elimination algorithm," *Journal of Applied Crystallography*, vol. 32, pp. 68–173, Apr. 1999. 61

[122] M. Birkholz, *Thin Film Analysis by X-ray Scattering*. Wiley-VCH, Weinheim, 2006. 63, 118, 119

[123] A. B. McLean, C. E. J. Mitchell, and D. M. Swanston, "Implementation of an efficient analytical approximation to the Voigt function for photoemission lineshape analysis," *Journal of Electron Spectroscopy and Related Phenomena*, vol. 69, no. 2, pp. 125 – 132, 1994. 63

[124] M. Galassi, J. Davies, J. Theiler, B. Gough, G. Jungman, P. Alken, M. Booth, and F. Rossi, *GNU Scientific Library Reference Manual*. Network Theory Limited, 3rd ed., 2009. 63

[125] J. J. Berry, S. J. Potashnik, S. H. Chun, K. C. Ku, P. Schiffer, and N. Samarth, "Two-carrier transport in epitaxially grown MnAs," *Physical Review B*, vol. 64, p. 052408, Jul 2001. xxii, 66, 91, 92, 101

[126] Y. Takagaki, E. Wiebicke, L. Däweritz, and K. Ploog, "Fabrication of MnAs microstructures on substrates and their electrical properties," *Journal of Solid State Chemistry*, vol. 179, pp. 2271–2280, Aug. 2006. xxi, 66, 69, 70, 73, 76, 77, 79, 81, 101

[127] A. M. Grishin, S. I. Khartsev, and K. V. Rao, "Giant fluctuation magnetoresistance in MnAs thin films," *Applied Physics Letters*, vol. 68, no. 14, pp. 2008–2010, 1996. 66

REFERENCES

[128] Y. Takagaki, L. Däweritz, and K. H. Ploog, "Abrupt changes in the temperature coefficient of resistivity induced by the phase transitions in MnAs films on GaAs," *Physical Review B*, vol. 75, no. 3, p. 035213, 2007. 66, 101, 112, 114, 115

[129] Y. Takagaki and K.-J. Friedland, "Magnetotransport properties in ($1\bar{1}00$)- and (0001)-oriented MnAs films on GaAs substrates," *Journal of Applied Physics*, vol. 101, no. 11, p. 113916, 2007. 66

[130] Y. Takagaki, J. Herfort, and K.-J. Friedland, "Extremely strong domain-wall pinning and spontaneous demagnetization in MnAs(0001) films on GaAs(111)B," *Physical Review B*, vol. 76, no. 18, p. 184409, 2007. 66

[131] G. W. Milton, *The Theory of Composites*. Cambridge University Press, 2002. 67

[132] D. J. Bergman, X. Li, and Y. M. Strelniker, "Macroscopic conductivity tensor of a three-dimensional composite with a one- or two-dimensional microstructure," *Physical Review B*, vol. 71, p. 035120, Jan 2005. 67

[133] D. K. Schroder, *Semiconductor material and device characterization*. New York: John Wiley & Sons, Inc., 1990. 69

[134] Y. Takagaki, E. Wiebicke, M. Ramsteiner, L. Däweritz, and K. Ploog, "Spontaneous growth of arsenic oxide micro-crystals on chemically etched MnAs surfaces," *Applied Physics A: Materials Science & Processing*, vol. 76, pp. 837–840, March 2003. 69

[135] J. Mohanty, Y. Takagaki, T. Hesjedal, L. Däweritz, and K. H. Ploog, "Selective etching of epitaxial MnAs films on GaAs(001): Influence of structure and strain," *Journal of Applied Physics*, vol. 98, no. 1, p. 013907, 2005. 69, 70

REFERENCES

[136] W. Seidel, K. H. Ploog, R. Engel-Herbert, and T. Hesjedal, "High-aspect ratio patterning of MnAs films," *Semiconductor Science and Technology*, vol. 21, no. 10, pp. 1502–1506, 2006. 70

[137] "Clariant Corp.." 70, 71

[138] Y. Takagaki, M. Moreno, P. Schützendübe, M. Ramsteiner, and C. Herrmann, "Cracking of epitaxial MnAs films on GaAs(001)," *Journal of Applied Physics*, vol. 107, p. 023510, Jan. 2010. 71

[139] Y. Takagaki, E. Wiebicke, T. Hesjedal, H. Kostial, C. Herrmann, L. Däweritz, and K. H. Ploog, "Self-organized etching technique for fabricating a quasiregular array of MnAs nanoislands," *Applied Physics Letters*, vol. 83, no. 14, pp. 2895–2897, 2003. 72

[140] A. R. Albrecht, *InAs Quantum Dot Vertical-Cavity Lasers.* PhD thesis, The University of New Mexico, 2009. 72

[141] "Ernest F. Fullam, Inc. No. 14811: Silver Conducting Paint In Plastic Squeeze Bottle." 74

[142] S. Chaudhary, A. K. Sisodia, and D. C. Dube, "Thermal hysteresis across the first-order phase transition in the $(Na_{0.5}Bi_{0.5})_{1-x}Ba_xTiO_3$ dielectric system," *Phase Transitions: A Multinational Journal*, vol. 78, pp. 895–904, Dec. 2005. 87

[143] S. Majumdar, V. Sharma, M. Manekar, R. Kaul, K. Sokhey, S. Roy, and P. Chaddah, "Magnetic and martensitic transitions in Ni-Fe-Ga alloy," *Solid State Communications*, vol. 136, no. 2, pp. 85 – 88, 2005. 87

[144] R. Engel-Herbert, A. Locatelli, S. Cherifi, D. Schaadt, J. Mohanty, K. Ploog, E. Bauer, R. Belkhou, S. Heun, A. Pavlovska, T. Leo, and T. Hesjedal, "Investigation of magnetically coupled ferromagnetic stripe arrays," *Applied Physics*

REFERENCES

A: Materials Science & Processing, vol. 84, pp. 231–236, 2006. 10.1007/s00339-006-3619-8. 90

[145] K. H. Ploog, L. Däweritz, R. Engel-Herbert, and T. Hesjedal, "Micromagnetic properties of MnAs-on-GaAs(001) films," *physica status solidi (a) - applications and materials science*, vol. 203, no. 14, pp. 3574–3580, 2006. 90

[146] T. Manago and H. Akinaga, "Ladder-type magnetic structures in MnAs epitaxial films–measurements and micromagnetic simulations," *Journal of Applied Physics*, vol. 104, no. 9, p. 093901, 2008. 90

[147] R. Engel-Herbert and T. Hesjedal, "Investigation of slanted and V-shaped domain walls in MnAs films," *Journal of Applied Physics*, vol. 105, no. 7, p. 07D504, 2009. 90

[148] M. Mitchell, "Engauge digitizer." http://digitizer.sourceforge.net/. 91

[149] S. V. Barabash and D. Stroud, "Negative magnetoresistance produced by Hall fluctuations in a ferromagnetic domain structure," *Applied Physics Letters*, vol. 79, no. 7, pp. 979–981, 2001. 104

[150] A. Ney, T. Hesjedal, C. Pampuch, J. Mohanty, A. K. Das, L. Däweritz, R. Koch, and K. H. Ploog, "Magnetic out-of-plane component in MnAs/GaAs(001)," *Applied Physics Letters*, vol. 83, no. 14, pp. 2850–2852, 2003. xxiii, 106, 108

[151] L. Däweritz, M. Kastner, T. Hesjedal, T. Plake, B. Jenichen, and K. Ploog, "Structural and magnetic order in MnAs films grown by molecular beam epitaxy on GaAs for spin injection," in *International Conference on Molecular Beam Epitaxy*, p. 413, 2002. 108

[152] S. H. Chun, S. J. Potashnik, K. C. Ku, J. J. Berry, P. Schiffer, and N. Samarth, "Intrinsic exchange biasing in MnAs epilayers grown on (001) GaAs," *Applied Physics Letters*, vol. 78, no. 17, pp. 2530–2532, 2001. 109

[153] E. Bauer, R. Belkhou, S. Cherifi, A. Locatelli, A. Pavlovska, and N. Rouge-maille, "Magnetostructure of MnAs on GaAs revisited," *Journal of Vacuum Science & Technology B*, vol. 25, no. 4, pp. 1470–1475, 2007. 110

[154] Y. Takagaki, C. Herrmann, J. Herfort, C. Hucho, and K.-J. Friedland, "Stress-modified structural and electronic properties of epitaxial MnAs layers on GaAs," *Physical Review B*, vol. 78, no. 23, p. 235207, 2008. 112

[155] A. R. Mackintosh, "Magnetic ordering and the electronic structure of rare-earth metals," *Physical Review Letters*, vol. 9, pp. 90–93, Aug 1962. 113

[156] R. J. Elliott and F. A. Wedgwood, "Theory of the resistance of the rare earth metals," *Proceedings of the Physical Society*, vol. 81, no. 5, pp. 846–855, 1963. 113

[157] B. Jenichen, D. Satapathy, W. Braun, L. Däweritz, and K. H. Ploog, "Microstructure of epitaxial MnAs films on GaAs(001): An in situ x-ray study," *Journal of Applied Physics*, vol. 96, no. 11, pp. 6103–6108, 2004. 116

[158] R. Resel, E. Tamas, B. Sonderegger, P. Hofbauer, and J. Keckes, "A heating stage up to 1173 K for X-ray diffraction studies in the whole orientation space," *Journal of Applied Crystallography*, vol. 36, pp. 80–85, Feb 2003. 119

[159] C. Dong, F. Wu, and H. Chen, "Correction of zero shift in powder diffraction patterns using the reflection-pair method," *Journal of Applied Crystallography*, vol. 32, pp. 850–853, Oct 1999. 120

[160] P. Weightman, D. S. Martin, R. J. Cole, and T. Farrell, "Reflection anisotropy spectroscopy," *Reports on Progress in Physics*, vol. 68, no. 6, pp. 1251–1341, 2005. 125

[161] C. Kaspari, *Fast optical in situ spectroscopy in III-V MOVPE*. PhD thesis, Technischen Universität Berlin, 2007. xxv, 126, 128

REFERENCES

[162] I. Kamiya, D. E. Aspnes, L. T. Florez, and J. P. Harbison, "Reflectance-difference spectroscopy of (001) GaAs surfaces in ultrahigh vacuum," *Physical Review B*, vol. 46, pp. 15894–15904, Dec 1992. xxv, 127

[163] D. E. Aspnes, J. P. Harbison, A. A. Studna, and L. T. Florez, "Reflectance-difference spectroscopy system for real-time measurements of crystal growth," *Applied Physics Letters*, vol. 52, no. 12, pp. 957–959, 1988. 126

[164] T. C. Oakberg, "Magneto-Optic Kerr Effect," application note, Hinds Instruments, 2007. 126

[165] S. D. Silaghi, *Optical Characterisation of DNA Bases on Silicon Surfaces*. PhD thesis, Technische Universität Chemnitz, 2005. 126

[166] F. Vidal, O. Pluchery, N. Witkowski, V. Garcia, M. Marangolo, V. H. Etgens, and Y. Borensztein, "α-β phase transition in MnAs/GaAs(001) thin films: An optical spectroscopic investigation," *Physical Review B*, vol. 74, no. 11, p. 115330, 2006. 134, 135, 138

[167] A. M. Fox, *Optical Properties of Solids*. Oxford Master Series in Condensed Matter Physics, Oxford University Press, 2001. 136

[168] K. Bärner, R. Braunstein, and E. Chock, "The optical properties of MnAs and $MnAs_{0.85}P_{0.15}$," *physica status solidi (b) - basic solid state physics*, vol. 80, no. 2, pp. 451–460, 1977. 136

[169] M.-F. Li, T. Ariizumi, K. Koyanagi, and S. Suzuki, "First-principles study of electronic structures of MnX (X=As, Sb, or Bi): Fully relativistic full-potential calculations," *Japanese Journal of Applied Physics*, vol. 46, pp. 3455–3462, 2007. xxvi, 140

[170] E. Munin, J. A. Roversi, and A. B. Villaverde, "Faraday effect and energy gap

in optical materials," *Journal of Physics D: Applied Physics*, vol. 25, no. 11, pp. 1635–1639, 1992. 142

[171] S. Streiffer and D. Fong, "Phase transitions in nanoscale ferroelectric structures," *MRS Bulletin*, vol. 34, pp. 832–837, Nov. 2009. 153